

COMPUTATIONAL FLUID DYNAMICS SIMULATION OF CHEMICALLY REACTING
GAS FLOWS THROUGH MICROFIBROUS MATERIALS

Except where reference is made to the work of others, the work described in this dissertation is my own or was done in collaboration with my advisory committee.
This dissertation does not include proprietary or classified information.

Ravi Kumar Duggirala

Certificate of Approval:

Bruce J. Tatarchuk
Professor
Chemical Engineering

Christopher J. Roy, Chair
Associate Professor
Aerospace Engineering

Anwar Ahmed
Associate Professor
Aerospace Engineering

Brian S. Thurow
Assistant Professor
Aerospace Engineering

Joe F. Pittman
Interim Dean
Graduate School

COMPUTATIONAL FLUID DYNAMICS SIMULATION OF CHEMICALLY REACTING
GAS FLOWS THROUGH MICROFIBROUS MATERIALS

Ravi Kumar Duggirala

A Dissertation

Submitted to

the Graduate Faculty of

Auburn University

in Partial Fulfillment of the

Requirements for the

Degree of

Doctor of Philosophy

Auburn, Alabama
May 10, 2008

COMPUTATIONAL FLUID DYNAMICS SIMULATION OF CHEMICALLY REACTING
GAS FLOWS THROUGH MICROFIBROUS MATERIALS

Ravi Kumar Duggirala

Permission is granted to Auburn University to make copies of this dissertation at its discretion, upon the request of individuals or institutions and at their expense. The author reserves all publication rights.

Signature of Author

Date of Graduation

VITA

Ravi K. Duggirala, son of Ratnaji Rao and Ratna Kumari, was born on December 21, 1980. He received his tenth grade degree in June 1996 and high school degree in June 1998. In August 1998, he entered GITAM, Andhra University, Visakhapatnam, Andhra Pradesh, India, and graduated with Bachelor in Mechanical Engineering in May 2002. He completed his graduate study and received a Master of Science degree in Mechanical Engineering from Florida International University (FIU), Miami in July 2004. During his stay at FIU, he worked as a research assistant at Applied Research Center.

In August 2004, he entered the Graduate School at Auburn University, Auburn, Alabama for a Doctoral of Philosophy in Aerospace Engineering. In March 2006, he was awarded as *Most Outstanding Graduate Student* by the departmental faculty.

DISSERTATION ABSTRACT

COMPUTATIONAL FLUID DYNAMICS SIMULATION OF CHEMICALLY REACTING
GAS FLOWS THROUGH MICROFIBROUS MATERIALS

Ravi Kumar Duggirala

Doctor of Philosophy, May 10, 2008
(M.S., Florida International University–Miami, 2004)
(B.E., Andhra University–India, 1998)

250 Typed Pages

Directed by Christopher J. Roy

This dissertation presents results of research efforts to propose a design space for new microfibrinous materials with enhanced chemical reactivity with optimum pressure gradient. These microfibrinous materials material are a new class of patented materials, consisting of catalytic particles (50-300 μm in size) entrapped in a matrix of microfibers (2-10 μm in size), which show enhanced chemical reactivity compared to packed beds. Computational Fluid Dynamics (CFD) was used as a design tool to analyze the flow through microfibrinous materials and to investigate the underlying mechanisms behind the enhancement in chemical reactivity. Numerical experiments were performed using different materials such as packed beds, frozen beds (particles frozen in space), and microfibrinous materials with different geometric properties for

two gas phase applications: (1) desulfurization, where a challenge gas of 2 vol.% H₂S in H₂ is used at a temperature of 400 °C and ZnO/SiO₂ is used for desulfurization, and (2) removal of trace amounts of hexane (100 ppmv of C₆H₁₄) from air.

Pressure drops were predicted using CFD and are in good agreement with experiments, even with significant geometric approximations. The effects of residence time, dilution with void, clustering, fiber diameter, and fibers loading on chemical conversion are studied. Dilution with void and clustering showed a negative effect on chemical conversion compared with packed bed. Adding fibers enhanced the chemical reactivity by providing more uniform, plug flow like conditions, even in the presence of dilution. Microfibrous materials with more numerous smaller diameter fibers are required to have enhanced chemical conversion when pressure drop is not important with a maximum factor of increase in chemical reactivity for these cases (60-80%). Another design criteria is investigated by comparing the ratio of log reduction to pressure drop (using the same amount of catalyst) for different materials. This work suggests that new microfibrous materials with enhanced chemical reactivity for a given pressure drop should be designed with fewer, larger diameter fibers. Maxima increases in chemical reactivity per pressure drop of 8 and 6 were found for H₂S and hexane, respectively, using 8 micron diameter fibers at 3% volume fraction with a total voidage of 80%.

ACKNOWLEDGMENTS

"SUCCESS DEPENDS ON OPPORTUNITY AND NOT ONLY ON TALENT"

I would like to express my sincere gratitude towards Dr. Christopher J. Roy for giving me an opportunity to work with him on this research. I also would like to sincerely thank him for his consistent support, warm encouragement, insightful suggestions and scientific guidance during this research. I would like to extend my thanks to Dr. Bruce J. Tatarchuk for his support, guidance, thoughtful ideas, and also for serving on my committee. I would like to acknowledge Dr. Anwar Ahmed and Dr. Brian S. Thurow for serving on my committee. I would also like to express my thanks and appreciation to Dr. W. Robert Ashurst, Department of Chemical Engineering, for serving as my external examiner.

I express my earnest appreciation toward the members of CM³ for their kind help, especially Drs. Don and Yang, and Mr. Ranjeeth Kalluri.

I also want to thank James Clark, Shannon Price, and Jeff Walker from network services for their prompt help.

Finally, I'd like to thank my family. My father extended his passion for education to me while my mother was a constant source of support. I am grateful to my brother and sister for their encouragement and enthusiasm. I am especially grateful to dearest

friends, Anup and Vamsi, for their patience and for helping me in keeping my life in proper perspective and balance.

Special thanks are due to my fellow Auburnites: Srinath, Mouli, Pavan, Harshal, Anil Raju, Samik, Uday, Sunil, Christoph Burger, and Ran Dai.

Though the following dissertation is an individual work, I could never have reached the heights or explored the depths without the help, support, guidance and efforts of a lot of people.

Style manual or journal used Journal of Approximation Theory (together with the style known as “aums”). Bibliography follows Journal of Fluids Engineering

Computer software used The document preparation package T_EX (specifically L^AT_EX) together with the departmental style-file aums.sty.

TABLE OF CONTENTS

NOMENCLATURE	xx
LIST OF FIGURES	xxi
LIST OF TABLES	xxvii
1 INTRODUCTION	1
1.1 Motivation	1
1.2 Microfibrous Materials	2
1.3 Microscale Gas Flows	6
1.4 Flow Through Porous Media	11
2 BASIC THEORY	15
2.1 Numerical Simulation Approach	15
2.1.1 Governing Equations	19
2.1.1.1 Continuity Equation	19
2.1.1.2 Momentum Equation	20
2.1.1.3 Energy Equation	22
2.1.1.4 Equation of State	23
2.1.1.5 Species Equation	24
2.1.2 Discretization	25
2.1.2.1 First-Order Upwind Scheme	26
2.1.2.2 Second-Order Upwind Scheme	27
2.1.3 Solvers	28
2.2 Chemical Reactions	32
2.2.1 Fundamentals of Chemical Reactions	32
2.2.1.1 Rate of Reaction	33
2.2.1.2 Reaction Rate Constant	34
2.2.1.3 Reaction Order	35
2.2.1.4 Weiz-Prater Criterion	36
2.2.1.5 Effectiveness Factor	37
2.2.2 Heterogeneous Reacting Systems	38
2.2.2.1 Rate Equation for Heterogeneous Reactions	39
2.2.2.2 Rate Controlling Step	40

2.2.3	Desulphurization	43
2.2.4	Hexane Removal	44
2.3	Dimensionless Numbers	45
2.3.1	Reynolds Number	45
2.3.2	Peclet Number	48
2.3.3	Damkohler Number	48
2.3.4	Knudsen Number	49
3	MICROFIBROUS MATERIALS	52
3.1	Description	52
3.2	Properties	54
3.3	Manufacturing	55
3.4	Applications	56
4	SUMMARY OF EXPERIMENTAL DATA	59
4.1	Pressure Drop	59
4.2	Chemical Conversion	61
5	EMPIRICAL CORRELATIONS FOR PRESSURE DROP	66
5.1	Ergun Equation	66
5.2	Porous Media Permeability Equation	69
6	NUMERICAL MODELING	75
6.1	Geometric Modeling	75
6.1.1	Geometric Approximations	75
6.1.2	Flow-field Mesh	77
6.1.3	Boundary Conditions	79
6.2	Modeling Species Transport/ Chemical Reactions	83
7	RESULTS AND DISCUSSION	85
7.1	Pressure Drop Predictions	85
7.1.1	Packed Beds	89
7.1.1.1	Numerical Accuracy	89
7.1.1.2	Results and Model Validation	93
7.1.2	Immobilized Beds	95
7.1.2.1	Numerical Accuracy	97
7.1.2.2	Results	100
7.1.3	Microfibrous Materials	104
7.1.3.1	Numerical Accuracy	105
7.1.3.2	Results and Model Validation	108

7.2	Dimensionless Analysis	117
7.3	Chemically Reacting Gas Flows	123
7.3.1	Desulfurization	124
7.3.1.1	Calibration of Reaction Rate for Simulations	125
7.3.1.2	Numerical Accuracy	126
7.3.1.3	Effect of Residence Time	128
7.3.1.4	Effect of Dilution with Void	132
7.3.1.5	Effect of Clustering	136
7.3.1.6	Effect of Fiber Diameter	140
7.3.1.7	Effect of Fiber Loading	144
7.3.2	Hexane Removal	149
7.3.2.1	Numerical Accuracy	150
7.3.2.2	Effect of Dilution with Void	152
7.3.2.3	Effect of Clustering	154
7.3.2.4	Effect of Fiber Diameter	159
7.3.2.5	Effect of Fiber Loading	162
7.3.2.6	Effect of Clustering in Microfibrous Materials	165
8	SIMULATION BASED DESIGN OF NEW MICROFIBROUS MATERIALS	171
8.1	Desulfurization	171
8.2	Hexane Removal	173
9	SUMMARY AND CONCLUSIONS	175
	BIBLIOGRAPHY	195
A	VERIFICATION OF VELOCITY SLIP BOUNDARY CONDITION	196
B	EFFECT OF INLET DIFFUSION	200
B.1	Rectangular Channel Reactor	200
B.2	Packed Bed Reactor	205
C	UNIFORM GRID REFINEMENT FOR GRID CONVERGENCE	208
D	FLUENT INPUT FILES AND USER-DEFINED FUNCTIONS	214
D.1	Input Files	214
D.1.1	Pressure Drop	214
D.1.2	Chemical Reactions	215
D.2	User Defined Functions	220
D.2.1	Slip Boundary Condition	220

D.2.2	Explicit Surface Reaction	221
-------	-------------------------------------	-----

NOMENCLATURE

Roman Letters

A	surface area	m^2
A_r	pre-exponential factor	depends on the order of reaction
a_v	surface area to volume ratio	$1/m$
C_A	concentration of species A	$kgmol/m^3$
C_i	inlet concentration of species	$kgmol/m^3$
C_o	outlet concentration of species	$kgmol/m^3$
d_p	diameter of the particle	m
\mathcal{D}_{AB}	mass diffusivity of A in B	m^2/s
d_{eq}	equivalent diameter	m
Da	Damkohler number	-
E_r	activation energy	$KJ/kgmol$
f	friction factor	-
h	specific enthalpy	J/kg
J	diffusive flux	$kgmol/m^2 \cdot s$
j_D	Chilton-Colburn factor	-
k_c	mass transfer coefficient	m^2/s

k_f	film mass transfer coefficient	$\text{m}^2/2$
k_{fr}	reaction rate constant	depends on order of reaction
Kn	Knudsen number	-
L	length of the domain	m
L_e	tortuous length	m
\mathcal{M}	total molecular weight of the mixture	kg/kgmol
\mathcal{M}_n	molecular weight of n^{th} species	kg/kgmol
N_i	No. of moles of i^{th} species	-
ΔP	pressure drop	Pa
p	pressure	Pa
P_c	clustering parameter	-
Pe	Peclet number	-
\mathcal{R}	specific gas constant	J/kgmol·K
r	reaction rate	depends on type of reaction
r_h	hydraulic radius	m
Re	Reynolds number	-
Re'	modified Reynolds number	-
Sh	Sherwood number	-
T	Temperature	K

t	time	s
t_c	chemical reactive time scale	s
t_d	diffusive time scale	s
t_f	convective time scale	s
U	uncertainty in numerical simulations	depends on parameter
U_n	species diffusion velocity	m/s
u, v, w	velocity in X,Y,Z direction, respectively	m/s
U_s	slip velocity	m/s
U_w	velocity of the wall	m/s
\vec{V}	velocity vector ($\vec{V} = u \vec{i} + v \vec{j} + w \vec{k}$)	m/s
V	fluid volume	m ³
V_f	face velocity	m/s
V_i	interstitial velocity	m/s
W	mass of the solid	kg
W_A	molar flux	moles/m ² ·s
x, y, z	cartesian coordinates	m
Y_n	mass fraction of n th species	-
NS	number of species	-

Greek Letters

α	thermal diffusivity	m^2/s
α'	relaxation factor	-
α_1, β_1	order of the reaction	-
χ	solid volume fraction	-
δ_{ij}	Kronecker delta	-
ϵ	void volume fraction	-
η	effectiveness factor	-
κ	thermal conductivity	$\text{W}/\text{m}\cdot\text{K}$
λ	mean free path	m
μ	absolute viscosity of the fluid	$\text{kg}/\text{m}\cdot\text{s}$
ν	kinematic viscosity	m^2/s
ω_n	rate of production of species i	kg/s
ϕ	shape factor	-
ϕ'	Thiele modulus	-
Π	stress tensor	Pa
ρ	density of the fluid	kg/m^3

σ_v	tangential momentum accommodation factor (TMAC)	-
τ_{ii}	normal stress	N/m ²
τ_{ij}	shear stress on j th plane in “i” direction	N/m ²
τ_t	tortuosity	-
θ	flow angle	rad
φ	arbitrary variable	-
f_v	viscous friction factor	-

Mathematical Expressions

Δ	increment	-
$\frac{\partial}{\partial x^2}$	second order partial derivative in x	1/m ²
$\frac{\partial}{\partial t}$	first order partial derivative in t	1/s
$\frac{D}{Dt}$	total derivative	1/m
∇	gradient ($=\frac{\partial}{\partial x} \vec{i} + \frac{\partial}{\partial y} \vec{j} + \frac{\partial}{\partial z} \vec{k}$)	1/m

Superscripts

n time level

Subscripts

AB species A in bulk

AS species A on surface

i, j, k values in X,Y,Z direction, respectively

m grid location

Acronyms

ACP Activated Carbon Particles

CFD Computational Fluid Dynamics

CLRC Central Laboratory of the Research Councils

CM ³	Center for Microfibrous Materials Manufacturing
GCI	Grid Convergence Index
GFE	Glass Fiber Entrapped
HEPA	High Efficiency Particulate Air
MFES	MicroFibrous Entrapped Sorbent
PB	Packed Beds
PC	Pyrolyzed Cellulose
PDE	Partial Differential Equation
PMP	Porous Media Permeability
RDE	Relative Discretization Error
SEM	Scanning Electron Microscope
SIMPLE	Semi Implicit Pressure Linked Equation
TSE	Taylor Series Expansion
VOC	Volatile Organic Compounds

LIST OF FIGURES

1.1	Comparison of velocity contours in a packed bed obtained from a) classical chemical engineering using one-dimensional analysis and b) CFD using two-dimensional continuum mechanics at the microscale	5
2.1	2D rectangular grid with finite volume discretization	27
2.2	Flow chart for segregated solver used in this study	30
2.3	Sequence of individual steps in a heterogeneous catalytic reaction (courtesy Fogler, 2001 [1])	40
2.4	Low Reynolds number flow regimes for a cylinder (courtesy: Panton [2])	47
3.1	Al_2O_3 particles entrapped in the matrix of 8 μm Ni fibers (SEM provided by CM ³)	53
4.1	SEM of sintered composite material of 55-58 μm ACP with 2, 4, and 8 μm Ni fibers [3]	60
4.2	Pressure drop through 8 μm Ni/ACP mesh (data from Cahela et al [3])	61
4.3	Breakthrough curve showing the effect of velocity on the reactivity of the packed bed (data from Yang [4])	62
4.4	Effect of velocity on the apparent rate constant (data from [4])	63
4.5	Morphologies of SiO_2 particles in glass fibers (courtesy Yang [4])	64
4.6	Comparison of breakthrough curves of GFE and PB (experimental data from Yang [4])	65
6.1	Geometric simplifications of the microfibrous materials used in the simulations: (a) isometric view and (b) front view	76
6.2	(a) SEM of a typical microfibrous material (from CM ³); (b) CFD model of the microfibrous material	77

6.3	Triangular mesh on the fiber and particle walls	78
6.4	Triangular mesh on the top symmetry face with a prismatic boundary layer mesh around the particles and the fibers	79
7.1	Convergence history and iterative convergence for a packed bed at $Re = 1.0$	90
7.2	Grid convergence for packed bed at $Re = 1.0$)	91
7.3	Discretization Error for a packed bed at $Re = 1.0$	92
7.4	Contours of velocity magnitude : $Re=1.0$	94
7.5	Contours of gauge pressure : $Re=1.0$	94
7.6	Pressure drop in packed beds obtained from simulations and empirical correlations compared with experimental data [4]; Numerical uncertainty = 0.5%	96
7.7	Convergence history and iterative convergence for immobilized bed ($\chi_p=30%$ at $Re = 1.0$)	97
7.8	Velocity contours in constant Y-Plane for Immobilized beds	101
7.9	Pressure contours in constant Y-Plane for Immobilized beds	102
7.10	Comparison of pressure drop from simulations to empirical correlations ($\chi_p=20%$ & $40%$; Numerical uncertainty = 1-2%)	103
7.11	Comparison of pressure drop from simulations to empirical correlations ($\chi_p=30%$ & $50%$); Numerical uncertainty = 0.1-0.5%	103
7.12	Iterative convergence for microfibrous materials ($\chi_p=53%$ at $V_f = 0.04$ m/s)	106
7.13	Discretization error in the pressure drop for microfibrous materials ($\chi_p=59%$)	107
7.14	Discretization error in the pressure drop for microfibrous materials ($\chi_p=53%$)	108

7.15	Velocity contours in constant Z-plane for microfibrrous materials: $V_f = 0.04$ m/s	109
7.16	Pressure contours in constant Z-plane for microfibrrous materials: $V_f = 0.04$ m/s	111
7.17	Comparison of pressure drop from simulations to empirical correlations and experimental data for microfibrrous materials [3]; Numerical uncertainty = 2-4%	113
7.18	Error in predicting pressure drop in microfibrrous materials with respect to experiments [3]: $X_p=53\%$	115
7.19	Error in predicting pressure drop in microfibrrous materials with respect to experiments [3]: $X_p=59\%$	116
7.20	Dimensionless analysis: log reduction	119
7.21	Dimensionless analysis: dimensionless pressure gradient	120
7.22	Flow properties for various gas and liquid phase applications	122
7.23	Discretization error for different microfibrrous materials: (a) log reduction; (b) pressure drop	127
7.24	Effect of residence time: (a) packed bed with 60 vol.% loading and microfibrrous material with 25 vol. % loading	130
7.25	Contours of velocity and concentration in packed beds at low velocity (1.3 cm/s)	131
7.26	3D Geometric Model: (a) packed bed with 60 vol.% loading and (b) diluted bed with 5 vol. % loading	132
7.27	Effect of dilution for desulfurization: (a) variation of log reduction with Reynolds number and (b) percentage difference in log reduction with respect to packed bed at 60 vol.% loading	134
7.28	Clustering parameter: (a) uniform bed and (b) clustered bed	136

7.29	Effect of clustering in the frozen bed (40 vol. % loading) for desulfurization: (a) variation of log reduction with Reynolds number and (b) percentage difference in log reduction with respect to the uniform frozen bed	138
7.30	Effect of clustering in the frozen bed (20 vol. % loading) for desulfurization: (a) variation of log reduction with Reynolds number and (b) percentage difference in log reduction with respect to the uniform frozen bed	139
7.31	Effect of fiber diameter in microfibrus bed (20 vol. % loading) for desulfurization: (a) variation of log reduction with Reynolds number and (b) percentage difference in log reduction with respect to packed bed at 60 vol.% loading	141
7.32	Effect of fibers on velocity profile: (a) packed bed (60 vol.% loading) (b) frozen bed (20 vol.% loading) (c) microfibrus bed bed (20 vol.% loading)	143
7.33	Effect of fiber loading in microfibrus bed (20 vol. % loading) for desulfurization: (a) variation of log reduction with Reynolds number and (b) percentage difference in log reduction with respect to packed bed at 60 vol.% loading	146
7.34	Effect of fibers on pressure drop for desulfurization: (a) variation of pressure drop with Reynolds number and (b) percentage difference in the pressure drop with respect to packed bed (60 vol.% loading) . . .	148
7.35	Discretization error for different microfibrus materials: (a) log reduction; (b) pressure drop	151
7.36	Effect of dilution for hexane removal: (a) variation of log reduction with Reynolds number and (b) percentage difference in log reduction with respect to packed bed at 60 vol.% loading	155
7.37	Effect of clustering in a frozen bed (40 vol. % loading) for hexane removal: (a) variation of log reduction with Reynolds number and (b) percentage difference in log reduction with respect to a uniform frozen bed	157

7.38	Effect of clustering in frozen bed (20 vol. % loading) for hexane removal: (a) variation of log reduction with Reynolds number and (b) percentage difference in log reduction with respect to uniform frozen bed	158
7.39	Effect of fiber diameter in microfibrus beds (20 vol. % loading) for hexane removal: (a) variation of log reduction with Reynolds number and (b) percentage difference in log reduction with respect to packed bed at 60 vol.% loading	161
7.40	Effect of fiber loading in Microfibrus bed (20 vol. % loading) for hexane removal: (a) variation of log reduction with Reynolds number and (b) percentage difference in log reduction with respect to packed bed at 60 vol.% loading	163
7.41	Effect of fibers on pressure gradient: (a) variation of pressure drop with Reynolds number and (b) percentage difference in the pressure drop with respect to the packed bed with 60 vol.% loading	164
7.42	Effect of clustering in microfibrus beds ($d_p = 150 \mu\text{m}$; $d_f = 4 \mu\text{m}$; $\chi_p = 20 \text{ vol.}\%$; $\chi_f = 1.5 \text{ vol.}\%$): (a) variation of log reduction with Reynolds number and (b) percentage difference in log reduction with respect to packed bed at 60 vol.% loading	166
7.43	Effect of clustering in microfibrus beds ($d_p = 150 \mu\text{m}$; $d_f = 8 \mu\text{m}$; $\chi_p = 20 \text{ vol.}\%$; $\chi_f = 3.0 \text{ vol.}\%$): (a) variation of log reduction with Reynolds number and (b) percentage difference in log reduction with respect to packed bed at 60 vol.% loading	169
7.44	Effect of clustering in microfibrus beds ($d_p = 150 \mu\text{m}$; $d_f = 4 \mu\text{m}$; $\chi_p = 20 \text{ vol.}\%$; $\chi_f = 3.0 \text{ vol.}\%$): (a) variation of log reduction with Reynolds number and (b) percentage difference in log reduction with respect to packed bed at 60 vol.% loading	170
8.1	Effect of fibers on ratio of log reduction to pressure gradient for desulfurization: (a) variation of the ratio with Reynolds number and (b) percentage difference in the ratio with respect to packed bed (60 vol.% loading)	172
8.2	Effect of fibers on ratio of log reduction to pressure gradient for hexane removal: (a) variation of the ratio with Reynolds number and (b) percentage difference in the ratio with respect to packed bed (60 vol.% loading)	174

A.1	Illustration of test case geometry for Poiseuille flow	196
A.2	Comparison of velocity profiles for Poiseuille flow at $Kn=0.01$	198
A.3	Comparison of velocity profiles for Poiseuille flow at $Kn=0.1$	198
A.4	Comparison of velocity profiles for Poiseuille flow at $Kn=1.0$	199
B.1	Schematic geometry of the rectangular channel reactor (red denotes reactive region)	200
B.2	Effect of inlet diffusion for different mass diffusivities at $V_f = 10$ cm/s	201
B.3	Effect of inlet diffusivity at different velocities: (a) entire domain (b) closeup of the reaction zone	202
B.4	Concentration contours in the rectangular reactor with buffer at different velocities	203
B.5	Effect of inlet buffer on the concentration profiles ; $V_f=10$ cm/s . . .	204
B.6	Schematic geometry of the packed bed reactor (red denotes reactive region)	205
B.7	Effect of type of inlet buffer on the concentration profiles	206
B.8	Effect of inlet buffer on the concentration profiles in packed bed reactors	207
C.1	Achieved grid refinement in all three directions (a) constant X, (b) constant Y, and (c) constant Z	213

LIST OF TABLES

2.1	Comparison between experimental, theoretical, and computation approach	16
2.2	Rate law and units of corresponding rate constant	36
2.3	Steps in a Catalytic Reaction (courtesy Fogler, 2001 [1])	41
2.4	Different flow regimes based on Knudsen number [5]	51
4.1	Comparison between glass fiber entrapped ZnO/SiO ₂ sorbent (GFES) and packed beds composed of ZnO/SiO ₂ particles (PB)	65
7.1	Discretization error in predicting pressure for packed bed	93
7.2	Discretization error in predicting pressure drop for immobilized beds .	99
7.3	Properties of modeled microfibrus materials used in the CFD simulations	104
7.4	Discretization error in predicting pressure drop for Microfibrus Materials	110
7.5	Operating conditions and fluid properties for desulfurization study . .	125
7.6	Calibration of Pre-Exponential Factor	126
7.7	Discretization error in log reduction and pressure gradient for different microfibrus materials for desulfurization	129
7.8	Geometric properties of the microfibrus materials modeled for CFD simulations to study the effect of fiber diameter	140
7.9	Geometric properties of the microfibrus materials modeled for CFD simulations to study the effect of fiber loading	145
7.10	Operating conditions and fluid properties for hexane study	150

7.11	Discretization error in log reduction and pressure gradient for different microfibrinous materials for hexane removal	153
7.12	Geometric properties of the microfibrinous materials modeled for CFD simulations to study the effect of clustering in microfibrinous materials	167
C.1	Parameters used in boundary layer grid refinement	209

CHAPTER 1

INTRODUCTION

1.1 Motivation

Reactor design uses information from a variety of areas - thermodynamics, chemical kinetics, fluid mechanics, heat and mass transfer, and economics. Chemical reaction engineering is the synthesis of all of these factors with the aim of properly designing a chemical reactor. Important applications of chemical reaction engineering of all kinds can be found both inside and outside the chemical process industries. Reactions are classified into homogeneous and heterogeneous reactions based on phase.

A catalyst is a foreign source that can greatly affect the course of a chemical reaction but emerges from the process unchanged. In most of the heterogeneous catalytic reactions the catalyst is solid and the reactants and products are in liquid or gaseous form. In all these processes the reaction takes place on an active site on the surface of the catalyst. Five steps occur at the catalyst surface. First reactants are adsorbed onto the catalyst surface where reactants diffuse into the pores within the catalyst pellet, then the surface reaction occurs, followed by diffusion of the products onto the surface, and finally desorption of the products from the surface. Among all these steps the slowest one is the rate limiting step. The Weisz-Prater Criterion uses

measured values of the rate of reaction to determine if internal diffusion (within the catalyst/particle) is limiting the reaction. If the Weisz-Prater parameter is less than one then there are no internal diffusion limitations.

The main object of catalytic process engineering is to obtain an efficient chemical conversion of a species with a given reactor size and catalyst [6]. Heterogeneous catalytic reactions are commonly used for many industrial applications such as petrochemical, air pollution, carbon catalytic cracking, ozone removal, CO oxidation, and fuel reforming. Every chemical processing industry aims for optimum reactor performance. Reactor performance can be improved in two ways: (1) design a better reactor or (2) design a better catalyst. This study focuses on the former by creating optimized materials that give efficient chemical conversion.

1.2 Microfibrous Materials

A new class of composite materials developed by Auburn University's Center for Microfibrous Materials Manufacturing (CM³) [7-9], microfibrous entrapped sorbents and catalysts (MFES/MFEC), have demonstrated beneficial chemical properties such as enhancing net reaction rates while reducing pressure drops. Below is a list of experimental studies that have shown the advantages of using MFES/MFEC over traditional packed beds:

1. A 2-3 fold improvement in chemical conversion over packed beds has been observed in gas phase H_2S removal using microfibrous entrapped ZnO/Silica adsorbent [10–12]
2. With similar catalyst loading, microfibrous catalyst composites using 16% Ni/Alumina catalyst have shown 2-6 times higher specific activities in a trickle bed for toluene hydrogenation [13].
3. Using MFEC/S, an improvement in conversion has been reported for preferential catalytic oxidation and low temperature oxidation of carbon monoxide in hydrogen reformat [10, 14].
4. MFEC/S have demonstrated significant benefits in personal and collective protection applications [15].

Although the experimental studies have shown advantages with the use of these materials, the underlying reasons for enhancement of chemical reaction rates have not been fully understood. Attempts were made by Kalluri et al. [16] to understand the significance of various factors influencing the overall reaction rates in packed beds and MFES using one-dimensional classical chemical engineering flow models.

Classical chemical engineering approaches using one-dimensional flow models cannot fully analyze the flow characteristics as they average the flow properties in

the domain and thus do not resolve property variations at the microscale level. Computational Fluid Dynamics (CFD), using multi-dimensional continuum mechanics at the microscale, can be used to analyze the flow characteristics. CFD solves the governing equation in a discretized domain and provides a detailed description of the local flow property variations.

As an example, classical chemical engineering approaches assume that the velocity is constant throughout the bed and is equal to the interstitial velocity (ratio of face velocity to voidage), whereas CFD using multi-dimensional continuum models at the microscale and appropriate boundary conditions, shows that the velocity varies in the bed and consists of peaking velocities when particles are close and that the velocity near the wall is reduced. Figure 1.1 illustrates the difference between classical chemical engineering approaches and CFD for the flow over 2D cylinders.

In order to know when these microfibrous materials are best suited to enhance the reaction rates, it is important to determine the pressure drop within the microfibrous material along with certain thermal properties [17]. The study of diffusion and surface reactions along with flow characteristics is also important to analyze the enhancement of chemical reactivity in microfibrous materials. This effort has been divided into several tasks which are summarized below.

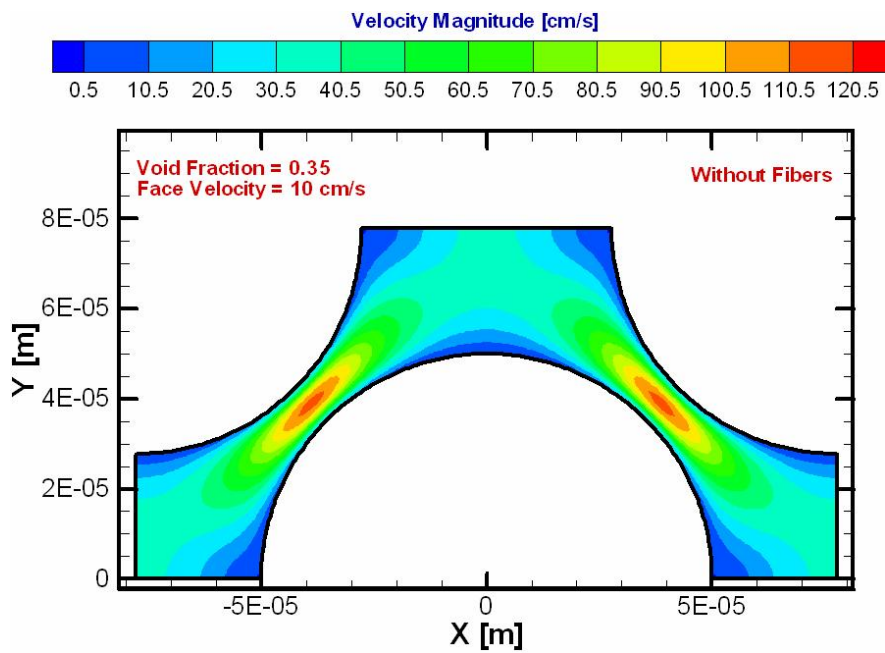
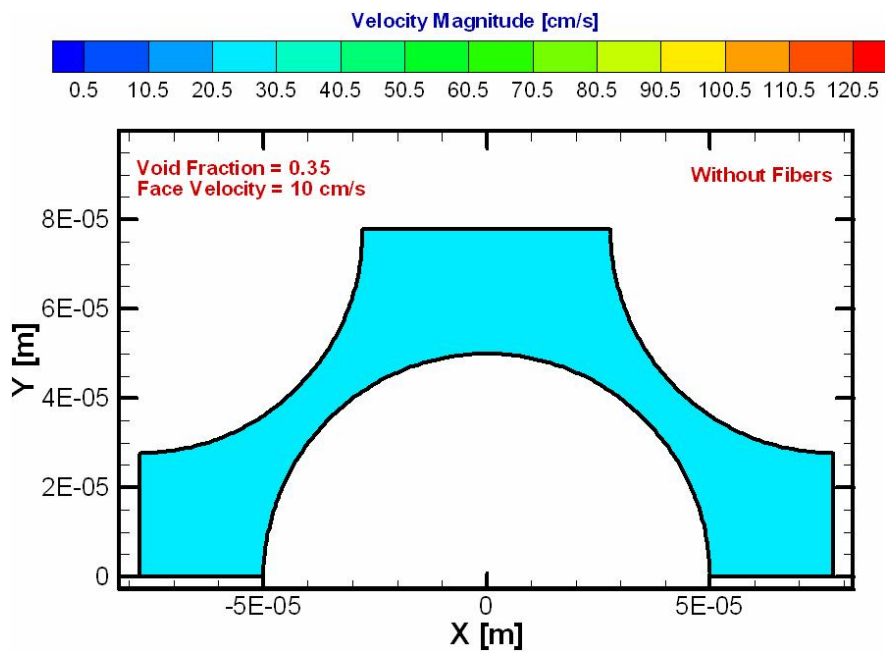


Figure 1.1: Comparison of velocity contours in a packed bed obtained from a) classical chemical engineering using one-dimensional analysis and b) CFD using two-dimensional continuum mechanics at the microscale

1. FLUID DYNAMICS: CFD is used to predict the pressure drop in packed bed and microfibrinous materials and then compared to empirical correlations (Ergun and PMP equations) as well as experimental results.
2. CHEMICAL REACTIONS: CFD is used to study the effect of residence time, channeling/flow maldistribution, particle size, and dilution on chemical reactivity in packed beds. The goal of this task is to provide a better understanding of surface reaction phenomena in packed beds.
3. VALIDATION: Experiments conducted by CM³ are used to validate the geometric CFD model of the microfibrinous material with mass diffusion and surface reactions.
4. DESIGN: Based on the understanding of the basic physical and chemical processes that occur in microfibrinous flows, CFD is used to design new microfibrinous materials with enhanced chemical reactivity.

1.3 Microscale Gas Flows

Microscale gas flow devices are becoming more prevalent due to recent advances in microsystems technology. Experimental study has shown that the underlying fluid mechanics is not the same for microscale gas flows and those at the macroscale. In order to understand microscale gas flows, several attempts were made to analyze

them using numerical methods. However, many of the earlier numerical studies either lacked the proper physics or were numerically expensive. In this section we briefly discuss applications of microscale gas flows, the importance of investigating microscale gas flows, the fluid dynamics of microscale gas flows, and previous attempts made to understand microscale gas.

Microscale gas flows are a rapidly growing research field driven by microsystem technology which has enabled advances in almost all engineering fields [18] including aerospace, chemical, biological, electrical, mechanical and materials engineering. Microsystems are devices that have a characteristic length of less than 1 millimeter but larger than 1 micron (1 micron = 10^{-6} meter) and often combine mechanical and electrical components. These systems have many advantages mainly due to their small size, thus miniaturizing the systems and improving their performance with low energy usage.

Microsystems are widely used in various industrial and medical fields [19, 20]. Applications of microsystems involving gas flows include: chemical sensors [21], hand held gas chromatography systems for the detection of trace concentrations of airborne pollutants [22], micro sensors and micro actuators to sense and control small-scale vortex structure for increasing the aerodynamic efficiency and maneuverability of aircraft [23–25], micro propulsion for spacecraft, and micro turbines [26, 27].

Our understanding of microscale gas flows is far behind the rapid development in fabrication and application of microsystems [28–31]. The examples given below show that the fluid mechanics of microscale gas flows differs from that experienced in the macroscopic world:

1. The pressure distribution in a long micro-channel was observed to be non-linear [32].
2. The measured flow rate in a micro channel was higher than that predicted from a conventional continuum flow model [33].
3. The friction force between the rotor and the substrate of a micro motor was found to be a function of the contact area instead of the normal force [28, 34]
4. The dynamic response of micro-machined accelerometers operating at atmospheric conditions was observed to be over-damped [29].

It is thus necessary to investigate the fluid mechanics of microscale gas flows in order to better understand microsystems and optimize their performance.

As mentioned above, the behavior of fluid mechanics at the microscale level differs from that found at macroscales. The characteristic length of a flow is an important parameter for many phenomena including flow regime and surface effects. Flows can be characterized by the Knudsen number (Kn), which is the ratio of the mean free

path between gas molecules to the characteristic length of the flow (see section 2.3.4 for details). For air at standard conditions, the equilibrium mean free path length is roughly 0.065 microns. If a macroscale gas flow has a characteristic length of 1 m, then the Knudsen number of the flow is significantly less than 0.01 and is considered to be in the continuum regime. If the flow instead has a characteristic length of 1 micron, then the Knudsen number is on the order of 0.1 and rarefied gas effects are important and should be included.

Surface force are prominent at small scales. The surface to volume ratio ($= 1/L$) changes from 1 m^{-1} to 10^6 m^{-1} as the characteristic length scale of a system is varied from 1 meter to 1 micron; thus, the surface forces that act on a flow dominate at the microscale level. Surface roughness and inhomogeneities are also involved for microscale gas flows.

Various numerical approaches have been developed in order to simulate and understand micro-scale gas flows. These flows can be modeled by solving continuum equations with slip boundary conditions (i.e., the continuum approach). Many conventional computational techniques can be used to solve the continuum equations including the finite volume method [35] and the finite element method [36]. To extend the application of the continuum approach to model flows in the slip regime, wall boundary condition having a discontinuous jump in velocity, temperature jump, and concentration jump are required due to rarefied gas phenomena.

Using the spectral element method, Karniadakis' group developed a Navier-Stokes solver [37] which uses a slip boundary condition that is designed to be valid over the entire range of Knudsen number [38, 39]. They studied the rarefied gas effects for flows in channels, pipes and ducts and showed that the continuum-based approach can be employed to simulate micro flows in the continuum and slip regimes [31].

Using upwind differences and a finite volume approach, a numerical method was developed by Hennighausen [40] which integrates the compressible Navier-Stokes equations on a deforming grid. The Maxwell slip boundary condition was used and a preconditioning technique was also implemented in order to expedite the iterative convergence at low Mach numbers.

Gas flow past a confined microsphere has been investigated over a range of Knudsen numbers covering continuum and slip regimes to estimate hydrodynamic drag forces on a stationary sphere by Barber et al. [41]. A two-dimensional finite-volume Navier-Stokes solver developed by CLRC (Central Laboratory of the Research Councils) has been used to solve the governing equations assuming an incompressible flow. A fully-developed slip-velocity profile in a pipe is used at the inflow boundary and at the outlet the axial gradient of the velocity components was assumed to be zero. It was observed that in continuum flow, the product of the Reynolds number and the drag coefficient collapse to a single value that depends upon the blockage ratio

and the blockage effects are important for continuum flows with very large increase in drag for height to diameter ratio less than five. Whereas in the slip regime, the total drag on a sphere decreases with the increase in Knudsen number. Thus, the drag amplification effect caused by the blockage ratio becomes less significant as the rarefaction effects starts to influence the flow.

1.4 Flow Through Porous Media

Transport phenomena in disordered systems have seen a great deal of study [42]. Particularly, fluid flow through porous media has been widely investigated due to its importance in several technological processes such as filtration, catalysis, chromatography, spread of hazardous wastes, and petroleum exploration and recovery [43]. Flow in porous media can be studied at either the microscopic or the macroscopic scale. At microscopic scales, the flow within individual pores is simulated using standard fluid dynamics equations, while at the macroscopic scale a continuum description based on volume averaging is used to derive the macroscopic governing equation from the equations pertaining to the microscopic scales [44].

It has been shown experimentally that the passage from linear to nonlinear behavior following Darcy's law is more likely to be gradual in flow through porous materials, whereas in pipes and channels there will be a critical Reynolds number that separates laminar and turbulent flow [45]. It has been proved numerically that

the contribution of inertia to the flow in the pores should also be examined in the laminar flow regime before making an assumption that it is fully turbulent [46, 47].

Information on the flow through packed beds was thoroughly examined by Ergun in 1952 [48]. He found that the pressure losses are due to simultaneous kinetic and viscous energy losses which follow a comprehensive equation that is applicable to flow through packed beds. Pressure losses depend upon flow rate, properties of the fluids, fractional void volume, as well as the orientation, size, shape, and surface of the particles in the packed bed (in section 5.1 we will discuss this equation in detail).

Papathanasiou et al. [49] evaluated the Ergun and Forchheimer equations for the permeability of fibrous porous media using square and hexagonal arrays of fibers. Arrays with uniform fibers as well as arrays in which the fiber size was allowed to change were used in their study with the porosity ranging from 0.30 to 0.60 (these lower porosities represent actual materials used in biotechnology applications) and the Reynolds number ranged between 0 and 160. No-slip boundary conditions were used on the fiber surfaces and symmetry boundary conditions were used in the fluid. The inlet and outlet were linked as periodic boundary condition and the pressure was obtained from the applied force in the direction of fluid flow. The authors compared the numerical results obtained from FIDAP to the predictions of KOKOPELLI, a research CFD code developed at Los Alamos National Laboratory. The authors reported that the numerical results coincided with the Ergun equation at high porosity

and low Reynolds number ($Re < 1$), whereas for low porosity and high Reynolds number, Ergun equation over-predicted the friction factor in square arrays. For the hexagonal geometry, numerical predictions were in good agreement for $Re < 1$, but disagreed for larger Reynolds number. The authors also observed that the Forchheimer equation slightly over-predicted the friction factor for the square geometry while it under-predicted it for the hexagonal array. At very low Reynolds number (creeping flow), the Forchheimer equation was in good agreement with the numerical simulations, while the Ergun equation did not capture the behavior of the fiber arrays in the flow with strong contracting/expanding elements.

Andrade et al. [50] investigated the origin of the deviation from the classical Darcy law numerically by simulating the Navier-Stokes equations in two-dimensional disordered porous media. They used the Forchheimer equation to correlate the variations of friction factor with porosity and the flow conditions. They observed the transition from linear to non-linear behavior of Darcy's law at high Reynolds number where inertia become important. They found that the transition can be understood and characterized in terms of spatial distribution of kinetic energy in the system.

Hicks [51] briefly discussed the validity of the Ergun equation in predicting the pressure drop in a packed bed of spheres. He showed that the coefficients (a, b) in the Ergun equation vary with Reynolds number and are not true constants. He also showed that the Ergun equation is not a good fit of pressure drop for smooth

spheres with the value $Re/(1-\epsilon)$ greater than 500 and that in the range $300 < Re/(1-\epsilon) < 60,000$, the viscous friction factor is represented by the non-linear relationship

$$f_v = 6.8 \left(\frac{Re}{1-\epsilon} \right)^{0.8} .$$

CHAPTER 2

BASIC THEORY

2.1 Numerical Simulation Approach

Over the past half century, a new methodology for solving complex problems in fluid mechanics and heat transfer has emerged. This new methodology is known as Computational Fluid Dynamics (CFD). In this numerical approach, the equations that govern the physical (and chemical) processes are solved numerically. Significant advances were made in the beginning of the twentieth century in numerical methods, especially finite difference for solving ordinary and partial differential equations.

There are basically three approaches that can be used to solve a problem in fluid mechanics and heat transfer:

1. Experimental
2. Theoretical
3. Computational (CFD)

The advantages and disadvantages in these three methods are described in Table 2.1.

Table 2.1: Comparison between experimental, theoretical, and computation approach

Method	Advantages	Disadvantage
Experimental	Capable of being most realistic	Equipment required Scaling problems Tunnel corrections Measurement difficulties Operating costs
Theoretical	Clean general information which is usually in formula form	Restricted to simple geometry Usually restricted to linear problems
Computational	Problems with highly non-linear flows can be solved Complicated physics can be treated Time evolution of flow can be obtained Obtains the flow details	Truncation error Boundary condition problems Computer costs Model errors

Several considerations determine whether the solution obtained from computational approach will be a good approximation to the exact solution to original PDE. These considerations include truncation error, round off errors, discretization errors, iterative errors, stability, and consistency.

TRUNCATION ERROR: Truncation error is defined as the difference between the partial differential equation (PDE) and the discrete approximation to it [52]. Consider the heat equation:

$$\frac{\partial \phi}{\partial t} = \alpha \frac{\partial^2 \phi}{\partial x^2} \tag{2.1}$$

Using a forward first difference in time and a central second difference in space, we can approximate Equation 2.1 by,

$$\frac{\phi_m^{n+1} - \phi_m^n}{\Delta t} = \frac{\alpha}{\Delta x^2} (\phi_{m-1}^n - 2\phi_m^n + \phi_{m+1}^n) \quad (2.2)$$

If we include the truncation error associated with the finite difference representation of derivatives, then we can write

$$\underbrace{\frac{\partial \phi}{\partial t} - \alpha \frac{\partial^2 \phi}{\partial x^2}}_{\text{PDE}} = \underbrace{\left[\frac{\phi_m^{n+1} - \phi_m^n}{\Delta t} - \frac{\alpha}{\Delta x^2} (\phi_{m-1}^n - 2\phi_m^n + \phi_{m+1}^n) \right]}_{\text{Finite Difference Equation}} + \underbrace{\left[-\frac{\partial^2 \phi}{\partial t^2} \Big|_m^n \frac{\Delta t}{2} + \frac{\partial^4 \phi}{\partial x^4} \Big|_m^n \frac{\Delta x^2}{12} + \dots \right]}_{\text{Truncation Error}} \quad (2.3)$$

In this case, truncation error is calculated using $TE = PDE - FDE$.

ROUND-OFF ERROR: Due to the finite bit size available on computers, results are rounded off at one or more intermediate steps [52]. The error produced due to this rounding is called round-off error. The most common problems resulting from roundoff error occur either when many steps are involved with rounding occurring at each step, when two quantities very close to each other are subtracted, or when a number is divided by a number which is close to zero. Round-off errors will always

exist and are usually negligible or controllable. In certain problems, the magnitude of the round-off error is proportional to the number of grid points in the computational domain. In these cases, refining the grid may decrease the truncation error but increase the round-off error [52].

DISCRETIZATION ERROR: In numerical simulations, continuous PDEs are converted into discrete algebraic equations. The difference between the exact solution to PDE and the round-off free, exact solution of the discrete algebraic equations is called discretization error [52]. These errors are grid dependent but *a priori* knowledge of the proper grid for a desired level of accuracy is generally lacking.

CONSISTENCY: Consistency addresses how well the FDE approximate the PDE. A consistent numerical scheme is one in which the TE goes to zero in the limit $\Delta t, \Delta x \rightarrow \text{zero}$. The above FDE for the heat equation is consistent since the TE goes to zero as $\Delta x, \Delta t \rightarrow 0$.

STABILITY: Numerical stability applies only to marching problems (parabolic or hyperbolic equations), although steady state elliptic problems are often solved by marching in time to a steady state solution. A stable numerical scheme is one in which errors do not grow as we proceed in the marching direction [52]. The stability limit for the above FDE for the heat equation is $\alpha \frac{\Delta t}{\Delta x^2} \leq \frac{1}{2}$.

2.1.1 Governing Equations

Modeling chemically reacting gas flows depends strongly on the application and the model of chemical reactions. It is based on a set of partial differential equations maintaining conservation of mass, momentum, energy, and species. These equations describe the convective motion of the fluid, the chemical reactions among the constituent species, and the diffusive transport processes such as thermal conduction and species diffusion.

2.1.1.1 Continuity Equation

The law of conservation of mass applied to an infinitesimal fixed control volume gives the continuity equation in differential conservation form:

$$\frac{\partial \rho}{\partial t} + \nabla \cdot \rho \vec{V} = 0 \quad (2.4)$$

The first term in the Equation 2.4 represents the rate of increase in the density and the second term represents the rate of mass flux passing out of the control volume. For a steady incompressible flow, $\rho = \text{constant}$ and $\frac{\partial \rho}{\partial t} = 0$ which reduces Equation 2.4 to

$$\nabla \cdot \vec{V} = 0 \quad \text{or} \quad \frac{\partial u}{\partial x} + \frac{\partial v}{\partial y} + \frac{\partial w}{\partial z} = 0 \quad (2.5)$$

2.1.1.2 Momentum Equation

Newton's second law applied to a fluid passing through an infinitesimal control volume yields the momentum equation:

$$\frac{\partial}{\partial t} (\rho \vec{V}) + \nabla \cdot (\rho \vec{V} \vec{V}) = \nabla \cdot \Pi_{ij} \quad (2.6)$$

The first term in the Equation 2.6 represents the rate of increase of momentum per unit volume in the control volume. The second term represents the rate of momentum lost by convection through control surface. The forces applied by external stresses such as normal and shearing stresses which can be represented by the stress tensor Π_{ij} . The stress tensor can be written as

$$\Pi_{ij} = -p\delta_{ij} + \mu \left[\left(\frac{\partial u_i}{\partial x_j} + \frac{\partial u_j}{\partial x_i} \right) - \frac{2}{3}\delta_{ij} \frac{\partial u_k}{\partial x_k} \right] \quad (2.7)$$

Upon substituting Equation 2.7 in Equation 2.6 and simplifying, we get the Navier-Stokes equations:

$$\rho \frac{D\vec{V}}{Dt} = -\delta_{ij} \nabla p + \frac{\partial}{\partial x_j} \left[\mu \left(\frac{\partial u_i}{\partial x_j} + \frac{\partial u_j}{\partial x_i} \right) - \frac{2}{3} \delta_{ij} \frac{\partial u_k}{\partial x_k} \right] \quad (2.8)$$

For a Cartesian coordinate system, Equation 2.8 can be separated into three scalar equations. The conservation of momentum the in x-direction is given by

$$\rho \frac{Du}{Dt} = -\frac{\partial p}{\partial x} + \frac{\partial \tau_{xx}}{\partial x} + \frac{\partial \tau_{yx}}{\partial y} + \frac{\partial \tau_{zx}}{\partial z}. \quad (2.9)$$

The conservation of momentum in the y-direction is given by

$$\rho \frac{Dv}{Dt} = -\frac{\partial p}{\partial y} + \frac{\partial \tau_{xy}}{\partial x} + \frac{\partial \tau_{yy}}{\partial y} + \frac{\partial \tau_{zy}}{\partial z}. \quad (2.10)$$

The conservation of momentum in the z-direction is given by

$$\rho \frac{Dw}{Dt} = -\frac{\partial p}{\partial z} + \frac{\partial \tau_{xz}}{\partial x} + \frac{\partial \tau_{yz}}{\partial y} + \frac{\partial \tau_{zz}}{\partial z}. \quad (2.11)$$

The viscous normal stresses are given by

$$\begin{aligned}\tau_{xx} &= \frac{2}{3}\mu \left(2\frac{\partial u}{\partial x} - \frac{\partial v}{\partial y} - \frac{\partial w}{\partial z} \right) \\ \tau_{yy} &= \frac{2}{3}\mu \left(2\frac{\partial v}{\partial y} - \frac{\partial u}{\partial x} - \frac{\partial w}{\partial z} \right) \\ \tau_{zz} &= \frac{2}{3}\mu \left(2\frac{\partial w}{\partial z} - \frac{\partial v}{\partial y} - \frac{\partial u}{\partial x} \right)\end{aligned}\tag{2.12}$$

and the viscous shear stresses are given by

$$\begin{aligned}\tau_{xy} = \tau_{yx} &= \mu \left(\frac{\partial v}{\partial x} + \frac{\partial u}{\partial y} \right) \\ \tau_{xz} = \tau_{zx} &= \mu \left(\frac{\partial w}{\partial x} + \frac{\partial u}{\partial z} \right) \\ \tau_{yz} = \tau_{zy} &= \mu \left(\frac{\partial w}{\partial y} + \frac{\partial v}{\partial z} \right)\end{aligned}\tag{2.13}$$

2.1.1.3 Energy Equation

The first law of thermodynamics applied to a fluid passing through an infinitesimal, fixed control volume yields the following energy equation:

$$\begin{aligned}
\frac{\partial}{\partial t}(\rho h) + \vec{\nabla} \cdot (\rho \vec{V} h) &= \vec{\nabla} \cdot (\kappa \vec{V} T) - \frac{\partial}{\partial x}(up) - \frac{\partial}{\partial y}(vp) - \frac{\partial}{\partial z}(wp) \\
&+ \frac{\partial}{\partial x}(u\tau_{xx}) + \frac{\partial}{\partial y}(u\tau_{yx}) + \frac{\partial}{\partial z}(u\tau_{zx}) \\
&+ \frac{\partial}{\partial x}(v\tau_{xy}) + \frac{\partial}{\partial y}(v\tau_{yy}) + \frac{\partial}{\partial z}(v\tau_{zy}) \\
&+ \frac{\partial}{\partial x}(w\tau_{xz}) + \frac{\partial}{\partial y}(w\tau_{yz}) + \frac{\partial}{\partial z}(w\tau_{zz})
\end{aligned} \tag{2.14}$$

2.1.1.4 Equation of State

For most problems in gas dynamics, it is possible to assume a perfect gas. A perfect gas is defined as a gas whose intermolecular forces are negligible. A perfect gas obeys the perfect gas equation of state:

$$p = \rho \mathcal{R} T \tag{2.15}$$

In this study, the perfect gas equation of state (Eq. 2.15) is used to calculate the density for the compressible gas flow with change in pressure.

2.1.1.5 Species Equation

For most chemically reacting gases, it is possible to assume that the intermolecular forces are negligible, and hence each individual species obeys the perfect gas equation of state. In addition, each species can be assumed as thermally perfect. The equation of state for a mixture of perfect gases can be written as:

$$p = \rho \frac{\mathcal{R}}{\mathcal{M}} T, \quad \mathcal{M} = \left(\sum_{n=1}^{NS} \frac{Y_n}{\mathcal{M}_n} \right)^{-1} \quad (2.16)$$

The species mass fractions in a reacting mixture of gases are determined by the species equation:

$$\frac{\partial \rho_n}{\partial t} + \nabla \cdot \left[\rho_n \left(\vec{V} + \vec{U}_n \right) \right] = r_n \quad (2.17)$$

Using the relation between mass fraction and species density, $Y_n = \frac{\rho_n}{\rho}$, and Fick's law, $\rho_n \vec{U}_n = -\rho \mathcal{D}_{AB} \nabla Y_n$, Equation 2.17 can be written as:

$$\frac{\partial Y_n}{\partial t} + \vec{V} \cdot \nabla Y_n - \mathcal{D}_{AB} \nabla^2 Y_n = \frac{r}{\rho} \quad (2.18)$$

Continuity (Eq. 2.5), x-momentum (Eq. 2.9), y-momentum (Eq. 2.10), z-momentum (Eq. 2.11), energy (Eq. 2.14), and species equations (Eq. 2.18) are solved using the

commercial CFD code FLUENT [53] to simulate incompressible, laminar, steady-state reacting flow.

2.1.2 Discretization

The process of converting partial differential equations into a set of algebraic relations which can be solved on a computer is called discretization [54]. It involves two main steps: (1) converting the continuum partial differential equations into algebraic relations and (2) converting the continuous physical domain into nodes, volumes, or elements where the algebraic equations will be solved. Discretization of partial differential equations can be done in many different ways. Among those, the two types of discretization used to solve problems in fluid mechanics and heat transfer are finite differences (discretization of partial differential form of equations) and finite volumes (discretization of equations in the integral form) [54].

In the finite difference approach, the continuous problem or domain is discretized so that the dependent variables are considered to exist only at discrete points. In the finite volume method, the conservation principles are applied to a fixed region or space known as the control volume. Using the finite volume approach, either control volumes are established first and grid points are placed at the center of the volumes (cell-centered method) or grid points are established first and then fix the boundaries of the control volume (vertex-centered method) [52]. The finite volume method using

the cell-centered approach is used in this study to convert the governing equations into an algebraic form which is then solved numerically.

There are various methods for discretizing the governing equations using the finite volume method. In this study, first-order and second-order accurate upwind methods are used. The cell-centered method is used which solves the flow properties at the cell centers; the values at the interfaces (used to obtain cell fluxes) are obtained by interpolating the cell-centered values with an upstream direction bias. This method is called an upwinding scheme.

2.1.2.1 First-Order Upwind Scheme

The solution obtained by using the first-order upwind scheme is first order accurate. In this method, the values at the interface are approximated with the cell-centered values in the upstream direction. This can be explained clearly using Taylor series expansions (TSE). Consider a variable φ which is stored at the cell-center and $\varphi_{i+\frac{1}{2}}$ be the value at the interface. Using the TSE, we can write $\varphi_{i+\frac{1}{2}}$ as

$$\varphi_{i+\frac{1}{2}} = \varphi_i + \frac{\partial\varphi}{\partial x}\bigg|_i \frac{\Delta x}{2} + \frac{\partial^2\varphi}{\partial x^2}\bigg|_i \left(\frac{\Delta x}{2}\right)^2 \frac{1}{2!} + \frac{\partial^3\varphi}{\partial x^3}\bigg|_i \left(\frac{\Delta x}{2}\right)^3 \frac{1}{3!} + \frac{\partial^4\varphi}{\partial x^4}\bigg|_i \left(\frac{\Delta x}{2}\right)^4 \frac{1}{4!} + \dots \quad (2.19)$$

In the Equation 2.19, if $\Delta x \rightarrow 0$ then Equation 2.19 becomes

$$\varphi_{i+\frac{1}{2}} = \varphi_i + TE$$

$$TE = \left. \frac{\partial \varphi}{\partial x} \right|_i \frac{\Delta x}{2} + \left. \frac{\partial^2 \varphi}{\partial x^2} \right|_i \left(\frac{\Delta x}{2} \right)^2 \frac{1}{2!} + \left. \frac{\partial^3 \varphi}{\partial x^3} \right|_i \left(\frac{\Delta x}{2} \right)^3 \frac{1}{3!} + \left. \frac{\partial^4 \varphi}{\partial x^4} \right|_i \left(\frac{\Delta x}{2} \right)^4 \frac{1}{4!} + \dots$$

where TE is truncation error. The order of the leading term of the truncation error gives the order of accuracy of the discretization. In this case, the approximation that $\varphi_{i+\frac{1}{2}} \sim \varphi_i$ is first-order accurate.

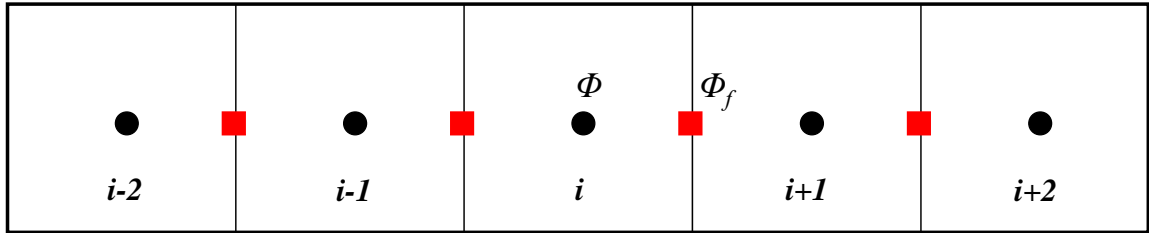


Figure 2.1: 2D rectangular grid with finite volume discretization

2.1.2.2 Second-Order Upwind Scheme

Using the second-order upwind scheme, quantities at the cell interface are computed using a multidimensional linear reconstruction approach [53]. In this approach, second-order accuracy is achieved using TSEs of cell-centered values. In Equation 2.19, as $\Delta x \rightarrow 0$, we can neglect higher order Δx terms and we get

$$\begin{aligned}\varphi_{i+\frac{1}{2}} &= \varphi_i + \left. \frac{\partial \varphi}{\partial x} \right|_i \frac{\Delta x}{2} + TE \\ TE &= \left. \frac{\partial^2 \varphi}{\partial x^2} \right|_i \left(\frac{\Delta x}{2} \right)^2 \frac{1}{2!} + \left. \frac{\partial^3 \varphi}{\partial x^3} \right|_i \left(\frac{\Delta x}{2} \right)^3 \frac{1}{3!} + \left. \frac{\partial^4 \varphi}{\partial x^4} \right|_i \left(\frac{\Delta x}{2} \right)^4 \frac{1}{4!} + \dots\end{aligned}$$

The order of Δx in the leading term of the truncation error is two, thus this scheme is second-order accurate.

2.1.3 Solvers

FLUENT [53], a commercial CFD code, has been used in this study to simulate reactive flow through microfibrinous materials. This section discusses the Fluent solver options that are used in this study. Governing equations for conservation of mass, momentum, energy, and chemical species are solved using cell-centered control volume based segregated solver.

SEGREGATED SOLVER: In this approach, the governing equations are solved sequentially (i.e., segregated from one another). Several iterations of the solution loop are performed before obtaining a converged solution. The basic steps involved in a segregated solver are:

1. Initial guess of pressure, velocity and species transport quantities such as mass flux is made.

2. The discretized Navier-Stokes equations (i.e., momentum equations) are solved using the guessed values of P^* , u^* , v^* etc. In this step coefficients to determine the fluxes through the cell/boundary faces by conduction/convection etc. The flow variables (p , u , v , w etc) for the entire domain (for each grid node) are obtained at the end of this step.
3. Once the flow properties are calculated, the continuity equation will be verified. If the continuity equation is not satisfied, pressure and velocity values (u , v , w) are corrected using pressure correction equation. SIMPLE algorithm is used for pressure-velocity coupling.
4. Once the flow properties are obtained, other discretized transport equations are solved. The initial guess for the transport quantities are depicted in step-1. After solving the transport equation, we get the transport properties at each node
5. In this step the flow and transport variables, obtained in step 3 and 4, at each node are compared with values of previous iteration and residuals are calculated using L_2 Norm. If the residuals are less than prescribed tolerance limit, the solution is final. If the residual is higher than tolerance limit, all steps 1-5 are repeated till it satisfies the convergence criteria. The initial guess values

are replaced with values of flow and transport variables obtained from current iteration.

Steps involved in each iteration are shown in Figure 2.2[53].

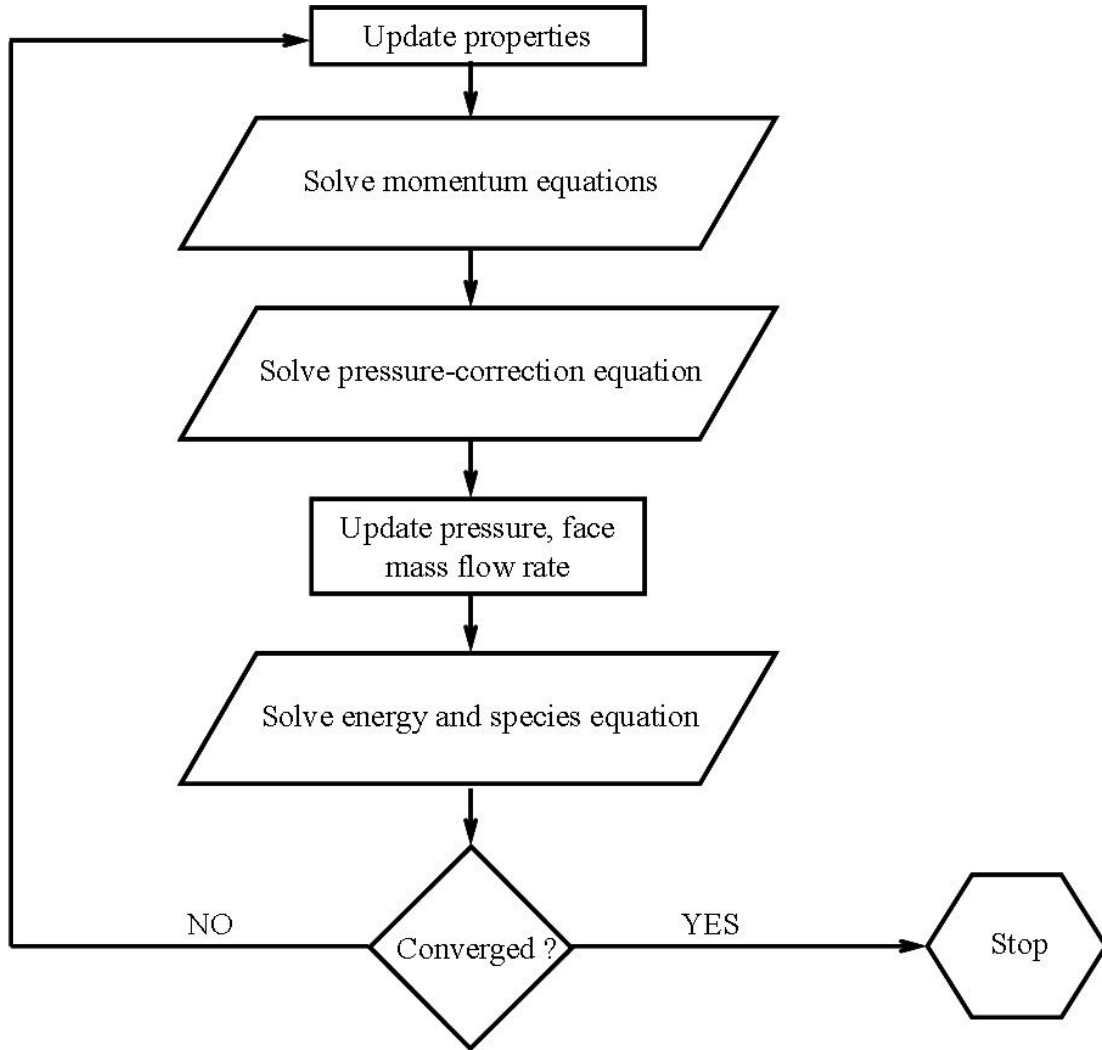


Figure 2.2: Flow chart for segregated solver used in this study

PRESSURE-VELOCITY COUPLING METHOD: A pressure-velocity coupling is used to derive an equation for pressure from the discrete continuity equation. The SIMPLE algorithm [53] is used to obtain a relationship between velocity and pressure corrections to enforce mass conservation and thus obtain the pressure field.

UNDER-RELAXATION FACTORS: Because the governing equations that we solve are a non-linear set of equations, it is necessary to control the change of variable (φ) for every iteration. This can be achieved by using under-relaxation factors, which reduces the change produced during each iteration. Let φ^n be the value at time step n , the computed change in φ from n to $n + 1$ be $\Delta\varphi$ and the relaxation factor be α' then

$$\varphi^{n+1} = \varphi^n + \alpha' \Delta\varphi \tag{2.20}$$

under-relaxation factors (α') are typically ranges between 0.5 and 1 (no under-relaxation).

2.2 Chemical Reactions

2.2.1 Fundamentals of Chemical Reactions

Chemical reactions are classified based on number and types of phases involved. The two main divisions of chemical reactions are homogeneous and heterogeneous reactions.

HOMOGENEOUS REACTIONS: A reaction is homogeneous if it takes place in one phase alone. The variables affecting the rate of reaction in these reactions are temperature, pressure, and composition. These chemical reactions are simple because the chemical changes that takes place are solely dependent on the nature of the interactions of the reacting substances.

HETEROGENEOUS REACTIONS: A reaction is heterogeneous if it requires the presence of at least two phases. The reactions that take places on the surface of a catalyst of a different phase are also heterogeneous . Practical applications of heterogeneous reactions are in catalytic convertors, fuel cells, and chemical vapor deposition among others. The variables affecting the rate of reaction in these reactions are heat and mass transfer. Heterogeneous reactions among solid-gas or gas-liquid interface are complex and are made up of several elementary physio-chemical process [55].

2.2.1.1 Rate of Reaction

The rate of reaction is defined as the number of moles of fluid reacting per unit time per unit volume. For a gas-solid catalytic system (heterogeneous reactions), the rate of reaction is defined as the number of moles reacted per unit time per unit mass of catalyst. The rate of reaction can be expressed in a number of ways based on volume, weight, surface area, etc. The reaction rate expressed based on unit volume of the reacting fluid:

$$r_v = \frac{1}{V} \frac{dN_i}{dt} = \frac{\text{moles } i \text{ formed}}{(\text{volume of fluid})(\text{time})}$$

unit mass of solid in the fluid-solid system:

$$r_w = \frac{1}{W} \frac{dN_i}{dt} = \frac{\text{moles } i \text{ formed}}{(\text{mass of solid})(\text{time})}$$

unit interfacial surface in the two-fluid system:

$$r_s = \frac{1}{A} \frac{dN_i}{dt} = \frac{\text{moles } i \text{ formed}}{(\text{surface})(\text{time})}$$

unit volume of the solid in the gas-solid system:

$$r_{v_s} = \frac{1}{V_s} \frac{dN_i}{dt} = \frac{\text{moles } i \text{ formed}}{(\text{volume of solid})(\text{time})}$$

Let r_A be the rate of formation of species A per unit volume. The rate of reaction can be expressed as:

$$\begin{aligned} r_A &= \frac{\text{moles } i \text{ formed}}{(\text{volume of fluid})(\text{time})} \\ \Rightarrow \frac{1}{V} \frac{dN_A}{dt} &= \frac{d(N_A/V)}{dt} = \frac{dC_A}{dt} \end{aligned} \tag{2.21}$$

The rate at which a species disappears/reacts can be written as the product of a reaction rate constant k and a function of concentration of various species involved in the reaction,

$$-r_A = [k_{fr}(T)] [fn(C_A, C_B, \dots)] \tag{2.22}$$

Equation 2.22 relates the species source term ($-r_A$) to the species concentration and is called kinetic expression or rate law.

2.2.1.2 Reaction Rate Constant

The reaction rate constant k is a proportionality constant in the relation between the rate of reaction and the concentration of species. The reaction rate constant is not

actually a constant but it is independent of the concentration of the species involved in the reaction and strongly dependent on temperature. The dependence of k on temperature can often be expressed using the Arrhenius equation (Eq. 2.23).

$$k(T) = A_r e^{-E_r/\mathcal{R}T} \quad (2.23)$$

where the activation energy E_r is the minimum energy required for a reaction to take place the reaction. The pre-exponential factor (or steric factor) A_r accounts for quantities such as the frequency of molecular collisions and their orientation. It varies slightly with temperature and is often taken as constant across small temperature ranges. The units of A_r are same as the units of the reaction rate constant and depend on the order of the reaction.

2.2.1.3 Reaction Order

The reaction rate can be expressed as a product of the rate constant and a function of the species concentrations in the reaction as:

$$-r_A = k C_A^{\alpha_1} C_B^{\beta_1} \quad (2.24)$$

The order of a reaction refers to the powers to which the concentrations are raised in the kinetic rate law. In Equation 2.24, the reaction is α_1 order with respect to species A and β_1 order with respect to species B. The overall order of the reactions is $\alpha_1 + \beta_1$. Consider a reaction involving only one reactant,



the rate laws corresponding to a zero, first, second, and third order reaction along with the units for corresponding rate constants are shown in Table 2.2

Table 2.2: Rate law and units of corresponding rate constant

Order of the Reaction	Rate Law	Units of Rate Constant
Zero-Order	$-r_A = k$	$\text{mol}/(\text{m}^3 \cdot \text{s})$
First-Order	$-r_A = kC_A$	s^{-1}
Second-Order	$-r_A = kC_A^2$	$\text{m}^3/(\text{mol} \cdot \text{s})$
Third-Order	$-r_A = kC_A^3$	$\text{m}^3/(\text{mol}^2 \cdot \text{s})$

2.2.1.4 Weiz-Prater Criterion

The Weiz-Prater criterion is an important method to determine the importance of diffusion limitations [1]. It uses measured values of rate of reaction to determine

whether internal diffusion is the rate limiting step and can be found using

$$\text{Weisz-Prater parameter, } \eta\phi'^2 = 3(\phi' \coth \phi' - 1) \quad (2.26)$$

If the Weisz-Prater parameter is small ($\ll 1$), then there are no diffusion limitations and no concentration gradient exists within the particle as intra-particle diffusion can be neglected. If the Weisz-Prater parameter is large ($\gg 1$), then internal diffusion limits the reaction and intra-particle diffusion cannot be neglected.

2.2.1.5 Effectiveness Factor

The Effectiveness factor η is a measure of how much the reaction rate is lowered because of the diffusional resistance in the pores. It is defined as the ratio of the actual reaction rate within pore to the rate if not slowed by pore diffusion [56].

$$\text{Effectiveness factor, } \eta = \frac{\text{actual reaction rate within pore}}{\text{rate if not slowed by pore diffusion}} \quad (2.27)$$

If all of the catalyst is present on the surface of the particle at a concentration of C_{AS} , the reaction rate would be

$$\text{rate of reaction} = (\text{rate per unit area})(\text{surface area})$$

The expression for the effectiveness factor given by Thiele and Zeldowich which found from concentration profiles using a diffusion equation is given by Equation 2.28 [57]

$$\eta = \frac{\tanh \phi'}{\phi'} \quad (2.28)$$

where the Thiele modulus $\phi' = L\sqrt{\frac{k\rho_s}{D_{AB}}}$. If $\phi' \rightarrow 0$, then the effectiveness factor is one which implies no appreciable resistance and one can assume that all sorbent is present on the surface of the particle.

2.2.2 Heterogeneous Reacting Systems

Heterogeneous reaction systems consist of more than one phase. The complicating factors for heterogeneous reactions are:

1. The complications of rate equation: Since it consists of more than one phase, movement of a substance from one phase to another should be included in the rate expression; thus, the rate expression should include mass transfer terms. These mass transfer terms are different for different types of heterogeneous systems, so, no general rate expression can be used.
2. The contacting patterns for the two-phase systems: In homogeneous system, the flow patterns are either plug or mixed flow. In heterogeneous systems, each phase may be in plug or mixed flow, so several combinations are possible. In

addition, if one of the phases is discontinuous (eg., droplets or solid particles), its macro-characteristics should also be involved.

2.2.2.1 Rate Equation for Heterogeneous Reactions

The rate equation for heterogeneous reactions involve more than one process. The rates of different processes can be combined (like heat conduction through layers of different materials) using convective mass transfer from one fluid to another through stagnant boundary films [56].

Let $r_1, r_2, r_3, \dots, r_n$ be the rates of individual processes. If the processes occur in parallel then the overall rate will be the sum of all individual processes [56]:

$$r_{overall} \text{ for parallel} = \sum_{i=1}^n r_i. \quad (2.29)$$

If these processes take place in series then the rate of all individual process is same [56]:

$$r_{overall} \text{ for series} = r_1 = r_2 = r_3 = \dots = r_n. \quad (2.30)$$

When the rates of reaction are compared or added, they should be defined in the same manner. The rate of reaction is defined based on the unit area for heterogeneous reactions, whereas it is defined based on the unit volume for homogeneous reactions.

2.2.2.2 Rate Controlling Step

In a heterogeneous catalytic reaction, the reaction/adsorption process occurs at the fluid-solid interface. There are some additional steps involved in the process that can affect the reaction rates. The process of catalytic reaction can occur in a sequence of individual steps which are shown in Figure 2.3 and explained in detail in Table 2.3. Hence, the rate of each individual step contributes to the overall reaction rate (i.e., it is a series reaction).

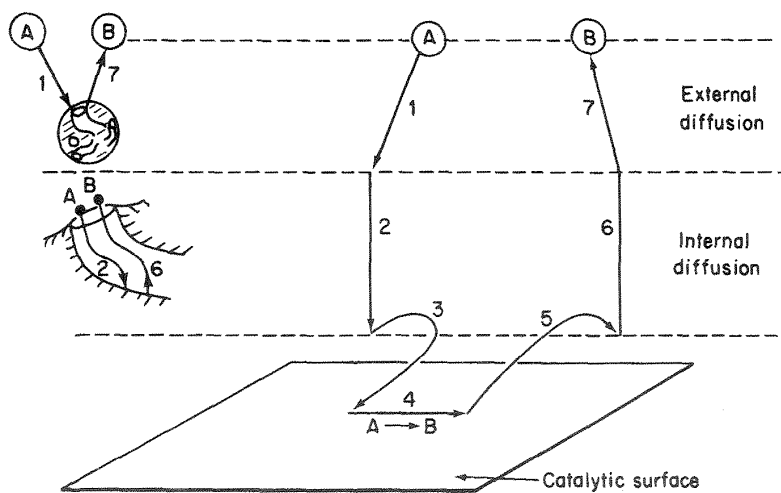


Figure 2.3: Sequence of individual steps in a heterogeneous catalytic reaction (courtesy Fogler, 2001 [1])

The various factors affecting the reaction rate are external diffusion, internal diffusion, and surface reaction. Surface reaction can be further divided into adsorption, reaction, and desorption. A brief discussion of each of these effects is presented next.

Table 2.3: Steps in a Catalytic Reaction (courtesy Fogler, 2001 [1])

1. Mass transfer of reactant from the bulk fluid to the external surface of the catalyst pellet (external diffusion)
 2. Diffusion of the reactant from the pore mouth through the catalyst pores to the immediate vicinity of the internal catalytic surface (internal diffusion)
 3. Adsorption of reactant on to the catalyst surface
 4. Reaction on the surface of the catalyst
 5. Desorption of the products from the surface
 6. Diffusion of the products from the interior of the pellet to the pore mouth at the external surface (internal diffusion)
 7. Mass transfer of the products from the external pellet surface to the bulk fluid
-

EXTERNAL DIFFUSION (steps 1 & 7): In any fluid-solid catalytic reaction, the fluid phase diffusion of chemical species to the solid surface and back to the bulk fluid phase is called external diffusion and is the key step which is often rate limiting. Molar flux from a bulk fluid at concentration C_{AB} to the surface of a spherical particle of diameter d_p at concentration C_{AS} is

$$W_A = k_c (C_{AB} - C_{AS}) \quad (2.31)$$

where k_c is the mass transfer coefficient which can be calculated using the Sherwood number $Sh = \frac{k_c d_p}{\mathcal{D}_{AB}} = 2.0 + 0.6 \cdot Re^{1/2} Sc^{1/3}$. Re and Sc are the Reynolds and Schmidt numbers (see section 2.3 for details). There are various correlations available in the literature to estimate the external mass transfer coefficient for various geometries (packed beds [58] and monoliths), Reynolds number ranges, and Schmidt number ranges.

Several approaches exist to estimate the Sherwood number in packed beds. At high Reynolds numbers (>10) the empirical correlations are reasonably accurate whereas at low Reynolds numbers the empirical correlations are off by up to four orders of magnitude. Various reasons have been cited for the observed mass transfer rates being far below the theoretically expected values. Due to small particles in the packed beds, the effects of channeling, and axial diffusion on the fluid-solid mass transfer and heat transfer rates are more prominent. The effects of channeling and clustering will be studied in detail during the course of this research.

INTERNAL DIFFUSION (steps 2 & 6): Once the reactants diffuse from the bulk fluid to external surface, they then diffuse from the external surface into and through the pores within the pellet. After the surface reaction occurs, the products need to diffuse out of the the particles. This process of diffusing reactants into the particles and products out of the particles is called internal diffusion. This additional step can become rate limiting and needs to be accounted for in reaction rate calculations. The

internal transport resistances are incorporated in the form of effectiveness factors, and estimation of these factors for various types of geometries is explained in the literature [59].

SURFACE REACTION (steps 3, 4 & 6): The surface reaction in a catalytic reaction consists of:

1. Adsorption (step 3): The reactant species that reach the pores within the pellet will be adsorbed on the catalytic sites.
2. Reaction (step 4): Once a reactant has been adsorbed onto the surface, reaction take place to form products.
3. Desorption (step 5): The products of the surface reaction are then desorbed into the fluid phase.

2.2.3 Desulphurization

Removal of sulfur from fuel typically using metal oxides, is called desulphurization. The concentration of sulfur in the fuel is an important controlling factor because the emission of sulfur leads to SO_x air pollution. The sulfur content in liquid fuels (such as diesel, JP8 et.,) is typically around 300-500 parts per million by weight (ppmw) [60, 61]. Desulfurization is also used for modern power technologies such as integrated gasification combined cycle and coal-to-electricity in the power generation

process which requires low concentrations of sulfur to operate. With efficient desulfurization, the power generation process can be improved significantly [62–64]. Fuel systems that use hydrocarbon fuels also require desulfurization to protect precious metal catalysts in fuel processors and the anode material in fuel cells from sulfur poisoning [12, 65, 66].

2.2.4 Hexane Removal

Volatile organic compounds (VOCs) are organic compounds which under normal conditions significantly vaporize and mix with atmosphere as they have high enough vapor pressures. A wide range of carbon-based molecules such as aldehydes, ketones, and hydrocarbons are considered as VOCs. These are the major atmospheric pollutants responsible for smog formation and other harmful health effects such as cancer [67]. Even at low concentrations, VOCs are harmful air pollutants and dangerous to the environment and human health [68]. Emission of VOCs may contribute to the acidification of rain, the generation of precursors of photochemical oxidants and the depletion of the stratospheric ozone layer [69]. VOCs can be removed either by catalytic oxidation or by adsorption.

One scenario for a potential terrorist attack is the release of chemical or biological agents in a city or building. Hexane often used as a laboratory surrogate for the

nerve gas Sarin. In this study, low concentration hexane removal using microfibrinous entrapped catalysts/sorbents by adsorption (physisorption) is explored.

2.3 Dimensionless Numbers

In this section, we discuss all the important dimensionless numbers used in this study. The various dimensionless number numbers used are:

1. Reynolds number
2. Peclet number
3. Damkohler number
4. Knudsen number

2.3.1 Reynolds Number

For microscale flows, the Reynolds number (ratio between inertial and viscous forces) is an important dimensionless parameter and is given by:

$$Re = \frac{\rho V d_p}{\mu} \quad (2.32)$$

Laminar flow occurs at low Reynolds numbers, where viscous forces are dominant, and is characterized by smooth, constant fluid motion. Turbulent flow, on the other

hand, occurs at high Reynolds numbers where the flow is dominated by inertial forces, thus producing chaotic turbulent eddies, vortices, and other flow fluctuations. The transition between laminar and turbulent flow is often indicated by a critical Reynolds number which depends on the exact flow configuration.

Microscale flows by definition have length scales in the order of microns ($1 \mu\text{m} = 10^{-6} \text{ m}$), thus the Reynolds numbers for microscale flows are generally very small. In order to examine the different flow regimes, it is helpful to examine the canonical flow over a cylinder shown in Figure 2.4 [2].

In the limit as the Reynolds number approaches zero, the flow remains attached and the streamlines are symmetric before and after the cylinder. For Reynolds numbers between zero and four, the flow is still attached, but the streamlines are no longer symmetric. For Reynolds numbers between four and forty, the flow separates behind the cylinder and a steady recirculation zone is formed. Finally, for Reynolds numbers between forty and approximately 100 (a typical upper limit for microscale flows), an oscillatory wake known as a Von-Karman vortex street is formed. Transition from a laminar to turbulent wake flow does not occur until Reynolds numbers greater than 200, thus turbulence is extremely unlikely in most microscale flows.

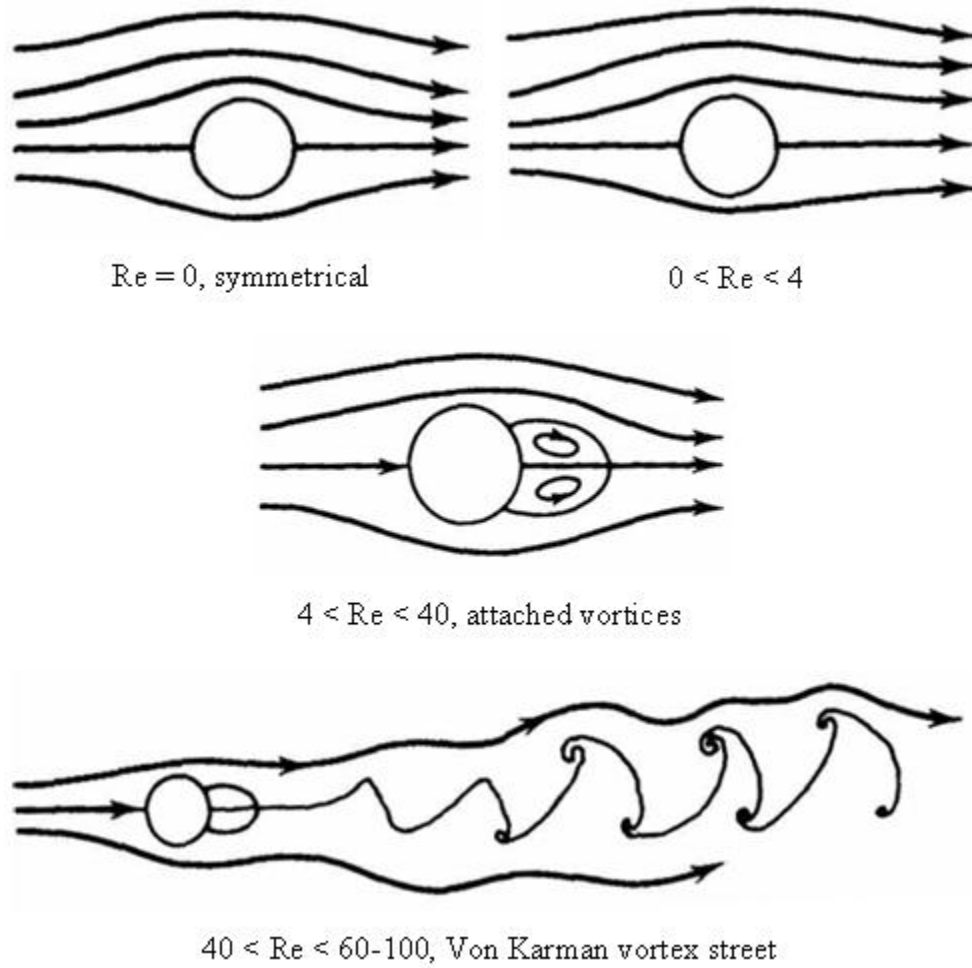


Figure 2.4: Low Reynolds number flow regimes for a cylinder (courtesy: Panton [2])

2.3.2 Peclet Number

Peclet number is a measure of the relative importance of species advection to species diffusion and can be written as

$$Pe_L = \frac{t_f}{t_d} = \frac{V_f L}{\mathcal{D}_{AB}}. \quad (2.33)$$

It is important to choose the proper length scale L because the Peclet number is proportional to length and diffusion dominates at small length scales. The Peclet number can also be calculated using the Reynolds and Schmidt numbers:

$$Pe = Re \cdot Sc; \quad Sc = \frac{\nu}{\mathcal{D}_{AB}} \quad (2.34)$$

2.3.3 Damkohler Number

The Damkohler number is a dimensionless number which provides an estimate of the degree of conversion that can be achieved in continuous flow reactions. There are many ways to define the Damkohler number, but in this study we defined it as the ratio of the convective time scale to the chemical reaction time scale ($\frac{t_f}{t_c}$):

$$\begin{aligned}
Da \text{ for surface reaction} &= \frac{d_p k_r}{V_f} a_v \\
Da \text{ for volumetric reaction} &= \frac{d_p k_r}{V_f}
\end{aligned}
\tag{2.35}$$

Larger Damkohler numbers correspond to very rapid chemical reactions in comparison to convection, thus the reaction is considered diffusion controlled. Small Damkohler numbers correspond to very slow chemical reactions in comparison to convection and are considered reaction controlled.

2.3.4 Knudsen Number

As the length scale of a physical system decreases, the validity of the standard continuum approach with no-slip wall velocity boundary conditions diminishes. The most commonly used dimensionless number that determines the degree of rarefaction of a gas and validity of the continuum flow assumption is the Knudsen number. It is defined as the ratio of the fluid mean free path between molecular collisions and the macroscopic length scale of the physical system

$$Kn = \frac{\lambda}{L} \tag{2.36}$$

where the fluid mean free path, λ , is defined as the average distance traveled by a molecule before it collides with another molecule. It can be expressed in terms of fluid properties like viscosity (μ), density (ρ), and temperature (T) as

$$\lambda = \frac{16\mu}{15\rho\sqrt{2\pi RT}} \quad (2.37)$$

Fluid flow can be divided into different regimes based on the Knudsen number which is shown in Table 2.4. When $\text{Kn} < 0.01$, it is called the continuum regime where the Navier-Stokes equations with no-slip boundary conditions govern the flow. When the Knudsen number ranges between 0.01 and 0.1, it is called the slip flow regime. In this regime, no-slip boundary conditions fail and the Knudsen layer starts to dominate. The Knudsen layer is less than 10% of the channel height or boundary layer thickness for external flows. This Knudsen layer can be neglected by extrapolating the bulk gas flow towards wall which results in a finite velocity value (i.e., velocity slip) at the wall. In the slip flow regime, the flow is governed by the Navier-Stokes equations and rarefaction effects can be modeled through the partial slip at the wall using Maxwell's velocity slip and Von-Smoluchowski's temperature jump boundary conditions. When the Knudsen number is greater than 0.1, the flow is said to be in the transition flow range. The flow in this regime requires higher-order corrections

to the constitutive laws that result in the Burnett or Woods equations which can be derived directly from the Boltzmann equation.

Table 2.4: Different flow regimes based on Knudsen number [5]

Knudsen Number (Kn)	Flow Type	Equations	Application
< 0.01	Continuum flow	Navier-Stokes equations with no-slip boundary condition	Micro-Channels, pumps etc.
$0.1 > \text{Kn} > 0.01$	Slip flow	Navier-Stokes equation with slip boundary condition	Micro-accelerometer, flow sensors, nozzle
$10 > \text{Kn} > 0.1$	Transitional flow	Burnett or Woods equation	Micro-channels, valves, nozzles
> 10	Free molecular flow	Boltzmann equations, DSMC, molecular dynamics	Micro-channels, valves, nozzles

CHAPTER 3
MICROFIBROUS MATERIALS

3.1 Description

Microfibrous materials developed at the Center of Microfibrous Materials Manufacturing (CM³) at Auburn University provide a novel method for versatile design of small, efficient, and lightweight fuel processors [3, 7–9, 12, 13, 70–77]. Microfibrous media carriers can be used with large surface to volume ratios to entrap micro-sized sorbent/catalyst particulates while withstanding considerable vibration and avoiding bypassing or channeling. This generic approach can also enhance heat/mass transfer, improve contacting efficiency, and promote regenerability [3, 13]. The fabrication of the microfibrous media is based on high-speed, roll-to-roll, paper-making and sintering processes, which substantially reduces production cost and improves product quality. Microfibrous entrapped 16% Ni/Al₂O₃ catalysts for toluene hydrogenation in a trickle bed reactor have demonstrated 2-6 times higher specific activities than the conventional packed bed catalysts on a gravimetric basis, while volumetric activities of 40 vol% composite catalysts were 80% higher than conventional extrudates [13]. Microfibrous entrapped 1% Pt-m/Al₂O₃ for PrOX CO provided 3-fold higher or more

bed utilization than the packed beds of 2-3 mm diameter pellets [72] at the same CO conversion.

Microfibrous materials are manufactured by a wet-lay paper-making/sintering process. The void volume in these media can be varied from 35% (typical packed beds) to 98% [3]. The diameter of the fibers used in these material generally varies from 2 to 20 μm , and the diameter of particles that are entrapped in the sintered bond of fibers varies from 10 to 300 μm . A Scanning Electron Microscope (SEM) image of a typical microfibrous material is shown in Figure 3.1.



Figure 3.1: Al_2O_3 particles entrapped in the matrix of 8 μm Ni fibers (SEM provided by CM³)

3.2 Properties

Microfibrous entrapped catalysts and sorbents (MFEC/S) possess many inherent beneficial properties. Large particles (> 1 mm) are typically used in conventional packed beds. In microfibrous systems, smaller particles are used which significantly reduce the intraparticle and the interphase heat and mass transport resistances. During the process of preparing MFEC/S using the wet-lay process. [7, 8, 11, 77] the microfibers and catalyst/adsorbent particles settle in a highly viscous medium. This assemblage of fibers and particles is self-correcting and hence leads to formation of uniform structures. This uniform structure of MFEC/S is a direct result of their preparation procedure and it helps in minimizing the intrabed channeling which can lead to flow maldistributions. As catalyst/sorbent particles in MFEC/S are held in space by high aspect ratio fibers of different materials, the voidage of these materials can be theoretically varied from 40% (typical packed bed) to as high as 99%. In practice, the typical volume loading of adsorbent/catalyst and fibers in MFEC/S is about 10-20% and 1-3%, respectively, with the remainder being void. The high voidage in MFEC/S promotes radial dispersion and hence suppresses undesirable axial dispersion of reactants/adsorbants in the direction of the flow.

The pressure drop across MFEC/S decreases with an increase in voidage. The flexibility of MFEC/S is another significant attribute which helps in achieving higher

conversion at lower pressure drops; this characteristic will be demonstrated clearly in this study. This design has shown significant benefits in the form of combining the high capacity of packed beds with the high efficiency of MFEC/S. Also, this design has resulted in significant decrease in the pressure drop.

3.3 Manufacturing

This new class of microfibrous materials are fabricated using a low cost, high speed wet-lay paper making process. Details of the fabrication process [17] and its advantages are discussed in this section.

The detailed procedure for the preparation of MFEC/S is discussed in the literature [3, 13, 17]. The raw materials used in the preparation of these materials are microfibers (metal, ceramic or polymer), catalyst support/adsorbent particles, cellulose, and viscosity modifiers. The generic procedure for the preparation of these materials involves four main steps:

1. Pre-form preparation
2. Pre-oxidation
3. Sintering
4. Catalyst impregnation

Micron diameter metal fibers (or combinations of metal fibers and catalyst/support powders) are processed into pre-form sheets and rolls along with cellulose fibers using traditional high speed wet-lay paper making techniques (*step 1: pre-form preparation*). This paper product obtained from the wet-lay process is then heated in a continuous hydrogen sintering furnace at 1000 °C. This heating process removes cellulose and causes the metal fibers to sinter-bond at their junctures so that it entraps the particulates present in the paper pre-form (*step 2/3: pre-oxidation and sintering*). After sintering, the fibrous void fraction of sintered fiber structures generally exceeds 98%. The advantages of using high-speed wet-layup paper making process are:

1. This process is low cost, high speed, and provides a self-correcting filtration process.
2. It achieves the desired physical structures.
3. It provides a unique combination of surface area, pore size/ particle size, and void volume.
4. The cellulose scraps can be recycled prior to sintering.

3.4 Applications

These microfibrinous materials can be employed as carriers for catalysts or sorbents [12, 72, 78], applied in electrochemical cells [70], or used as HEPA filters [17, 79].

CM³ has also developed MFEC/S for desulfurization applications which have shown 2-3 fold improvement over packed bed breakthrough times in gas phase H₂S removal [10, 11, 74] using Ni fibers to entrap ZnO/SiO₂ and ZnO/ACP sorbents. The MFEC/S using ZnO/SiO₂ was designed and employed for regenerable use to scavenge bulk H₂S from reformat streams in a continuous batch mode at 400⁰C or use in the primary desulfurization unit. ZnO/ACP was designed to remove trace amounts of H₂S to below the ppb poisoning threshold of Proton Exchange Membrane fuel cells. This MFEC/S also protects fuel cells during unsteady operations for fuel cleanup processes. Composite beds consisting of packed beds of 1-2 mm diameter extrudates followed by high contacting efficiency microfibrus entrapped polishing sorbents were also demonstrated, and details of the performance of these sorbents were described by Lu et al. [12].

Significant improvements have been reported with the use of MFEC/S for preferential catalytic oxidation and low temperature oxidation of carbon monoxide in hydrogen-reformat streams [11, 74]. MFEC/S composites using a 16% Ni/Al₂O₃ catalyst have demonstrated 2-6 fold higher specific activities than conventional packed beds with similar catalyst loading for toluene hydrogenation in a trickle bed reactor [13]. Carbon-based MFEC/S have shown significant benefits in terms of pressure drop

and gas life for various personal and collective protection applications [15]. Other applications where MFEC/S have been used include ozone/VOC abatement for aircraft cabin air purification and liquid phase sulfur removal from jet fuels, etc.

CHAPTER 4

SUMMARY OF EXPERIMENTAL DATA

Experiments conducted at CM³ are used to validate the models used in the current CFD simulations. Cahela et al. [3] and Yang [4] conducted experiments to measure pressure drop and chemical conversion in the microfibrous materials and packed beds, respectively. The experimental data reported in these two studies were used to validate the CFD simulations used in this study.

4.1 Pressure Drop

Experiments were conducted by Cahela et al. [3] to measure the pressure drop in microfibrous materials consisting of nickel (Ni) and pyrolyzed cellulose (PC) fibers of diameters 8 μm and 10 μm , respectively, and 100-120 mesh activated carbon powder (ACP). The solid volume percentages of Ni, ACP, and PC were 7.1%, 91.4%, and 1.5%, respectively. Pressure drops were measured in these materials with 40-50% void face velocities between 0.04 m/s and 1.29 m/s. (The face velocity is defined as the velocity that would occur if the flow were uniform without microfibrous material.) An SEM image of 55-58 μm ACP entrapped in a micro-metal fiber matrix of 2, 4, and 8 μm Ni fibers is shown in Figure 4.1 where the fibers and ACP are clearly identifiable.

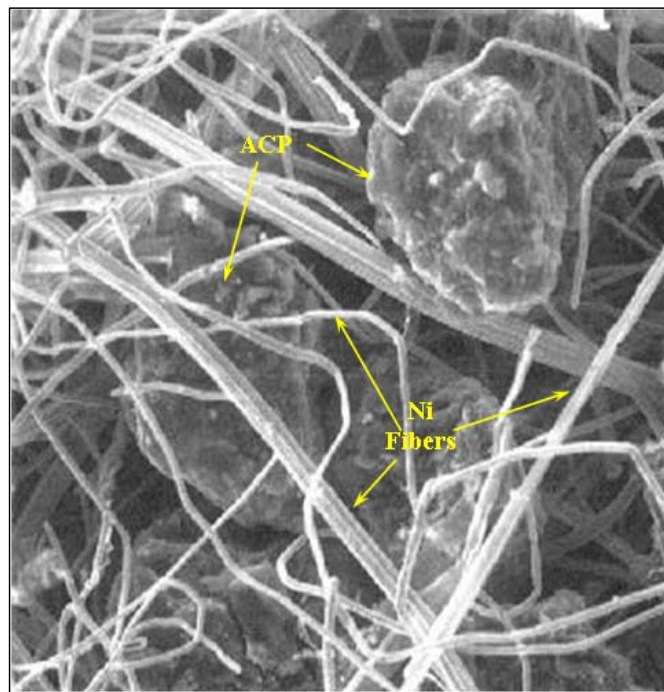


Figure 4.1: SEM of sintered composite material of 55-58 μm ACP with 2, 4, and 8 μm Ni fibers [3]

The measured pressure drops across the unit length of the bed are plotted against the face velocity for void fractions of 0.41 and 0.47 are shown in Figure 4.2. The pressure drop varies linearly with the face velocity for both void fractions. It should be noted that the experimental data set also includes pressure drop measurements at a voidage of 0.67; however, problems securing the microfibrinous media in the test apparatus (related to the deformation of the edges of the high voidage, sponge-like material) are believed to have created significant bias errors. Therefore, these high voidage data are omitted from the present study.

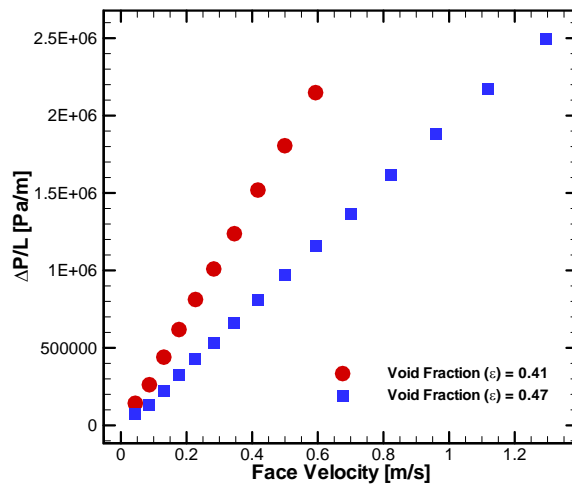


Figure 4.2: Pressure drop through 8 μm Ni/ACP mesh (data from Cahela et al [3])

4.2 Chemical Conversion

Experiments were conducted by Yang [4] to study the effect of face velocity (residence time) on the breakthrough capacities and apparent rate constants in packed

beds. The particles in the packed beds were SiO_2 coated with ZnO on the pore surface. All the ZnO/SiO_2 sorbents were tested at 400°C with a challenge gas of 2 vol.% H_2S in H_2 . During the experiment, 0.1 g of prepared ZnO/SiO_2 sorbent was loaded in the reactor with a bed thickness of 2.0 mm at a gas face velocity of 1.3 cm/s. In the experiments, the amount of sorbent and the face velocity were doubled at simultaneously until the sorbent loading reached 0.8 g and the face velocity reached 10.4 cm/s.

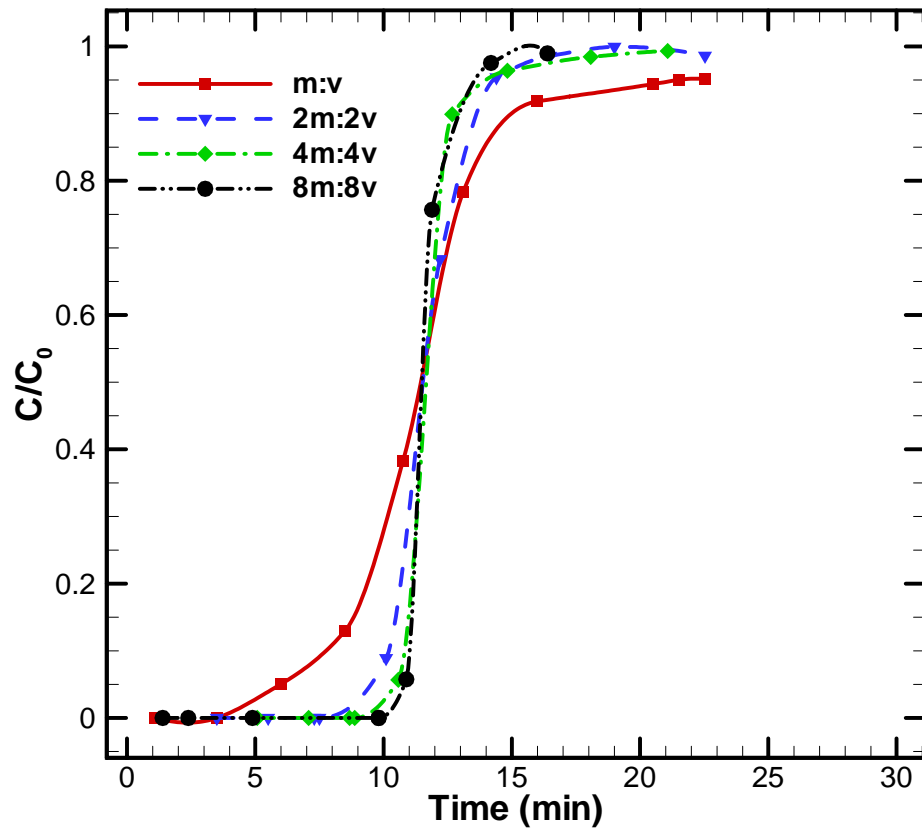


Figure 4.3: Breakthrough curve showing the effect of velocity on the reactivity of the packed bed (data from Yang [4])

The breakthrough curves and effect of the face velocity on the apparent rate constant are shown in Figures 4.3 and 4.4.

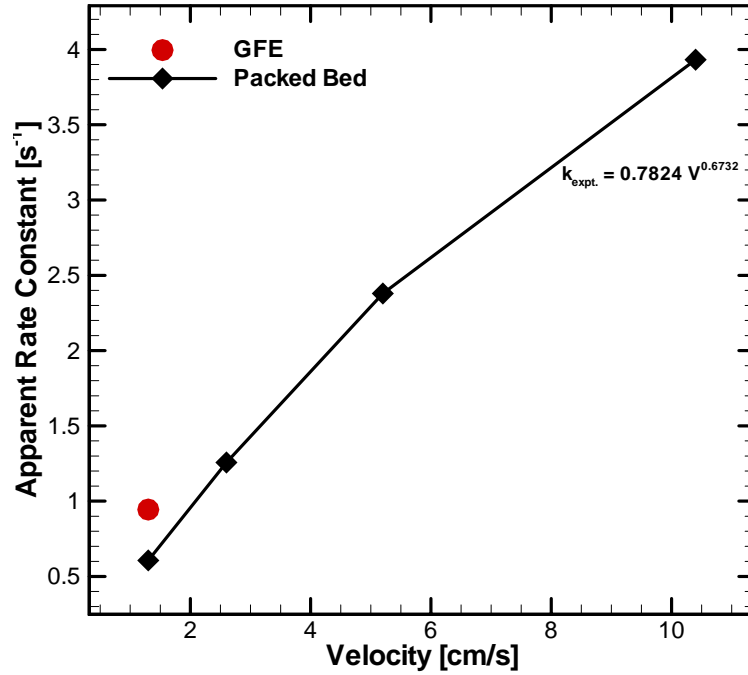


Figure 4.4: Effect of velocity on the apparent rate constant (data from [4])

Figure 4.3 shows that all of the packed beds in this set of tests had the same theoretical saturation time t (or $t_{\frac{1}{2}}$) of 12 minutes and the same residence time of 0.075 s. The breakthrough curves become sharper as the face velocity of challenge gas is increased.

Glass fiber entrapped sorbent containing 0.1 g of ZnO/SiO₂ sorbent, shown in Figure 4.5, were also tested at the velocity of 1.2 cm/s.

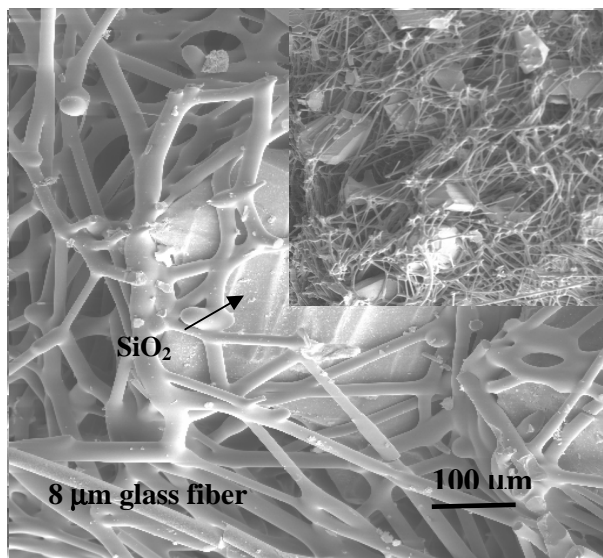


Figure 4.5: Morphologies of SiO₂ particles in glass fibers (courtesy Yang [4])

Figure 4.6 shows the comparison of breakthrough curves with packed bed (m:v experiment) and glass fiber entrapped sorbents at same loading. The breakthrough curve of glass fiber entrapped sorbents shows the capacity at breakthrough increases about 50% compared with the packed bed experiment, while in both cases, the same type of sorbent (ZnO/SiO₂) with the same amount of ZnO catalyst was used. Therefore, the resulting improvement is related to the geometry of the glass fiber media.

Table 4.1 shows the percent loading by weight and volume of each component in the packed beds and microfibrinous materials used by Yang [4] during his experiments.

Table 4.1: Comparison between glass fiber entrapped ZnO/SiO₂ sorbent (GFES) and packed beds composed of ZnO/SiO₂ particles (PB)

Components	Wt.%		Vol.%	
	GFES	PB	GFES	PB
ZnO	13	17	NA	NA
SiO ₂	65	83	22	60
μ Fibers	22	NA	3	NA
Void	NA	NA	75	40

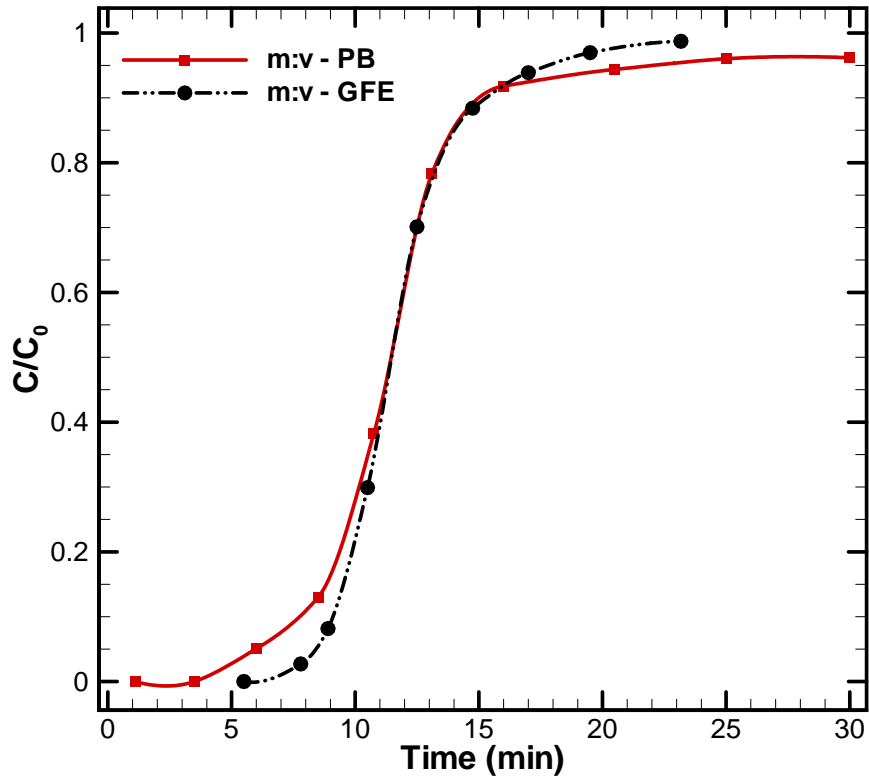


Figure 4.6: Comparison of breakthrough curves of GFE and PB (experimental data from Yang [4])

CHAPTER 5

EMPIRICAL CORRELATIONS FOR PRESSURE DROP

5.1 Ergun Equation

The linear Ergun equation is used to predict the pressure drop through packed beds. In this section, The Ergun equation is derived for laminar and turbulent flows from the Hagen-Poiseuille law.

Assuming the hydraulic radius r_h (the ratio of cross-sectional area to wetted perimeter) as the length scale, the friction factor can be defined as

$$f = \frac{2(\Delta P/L) r_h}{\rho V_i^2} \quad (5.1)$$

where the interstitial velocity V_i is defined as the face velocity divided by the voidage ($V_i = V_f/\epsilon$).

The hydraulic radius can be written as

$$r_h = \frac{\epsilon}{a_v(1 - \epsilon)}$$

where

$$a_v = \frac{\text{Surface Area}}{\text{Volume}} = \frac{6}{d_p} \text{ (for a sphere)}$$

Thus we can write

$$r_h = \frac{\epsilon d_p}{6(1 - \epsilon)} \quad (5.2)$$

Substituting face velocity and hydraulic radius (into Equation 5.1) we get

$$f = \frac{\left(\frac{\Delta P}{L}\right) \epsilon^2 d_p}{3\rho V_f^2 (1 - \epsilon)}. \quad (5.3)$$

For laminar flows, Hagen-Poiseuille law can be written as

$$f = \frac{16}{Re'}. \quad (5.4)$$

For packed beds, the modified Reynolds number can be written as:

$$Re' = \frac{V_f (4r_h) \rho}{\mu} = \frac{2}{3} \frac{V_f d_p \rho}{\mu (1 - \epsilon)} \quad (5.5)$$

Substituting Re' into Equation 5.4 we get

$$f = \frac{24\mu(1-\epsilon)}{V_f d_p \rho}. \quad (5.6)$$

Equating Equations 5.3 and 5.6 results in

$$\frac{\frac{\Delta P}{L} \epsilon^2 d_p}{3\rho V_f^2 (1-\epsilon)} = \frac{24\mu(1-\epsilon)}{V_f d_p \epsilon} \quad \text{or} \quad (5.7)$$

$$f' = \frac{\Delta P d_p \epsilon^3}{L \rho V_f^2 (1-\epsilon)} = 72 \frac{(1-\epsilon)}{\frac{\rho V_f d_p}{\mu}}.$$

By applying the least square method to existing experimental data, Ergun increased the numerical coefficient of 72 to 150 [80]. This modification is a simple empirical correction to the numerical coefficient only. Equation 5.8 is called the Blake-Kozeny equation:

$$f' = \frac{\Delta P d_p \epsilon^3}{L \rho V_f^2 (1-\epsilon)} = 150 \frac{(1-\epsilon)}{\rho V_f d_p / \mu} \quad (5.8)$$

For turbulent flows, the friction factor for flow through packed beds can be expected to follow Prandtl's resistance law. However, the Prandtl's resistance law is valid (and agrees well) for smooth tubes and pipes only. Roughness on the surface

increases the friction factor at high Reynolds numbers where one can assume the friction factor is independent of Reynolds number. Thus, for turbulent flows we have:

$$f = \frac{\Delta P d_p \epsilon^3}{L \rho V_f^2 (1 - \epsilon)} = \text{constant} \quad (5.9)$$

A constant of 1.75 fits the data from experiments. With this constant, Equation 5.9 is called the Burke-Plummer equation [80]. The friction factor for flows with Reynolds numbers ranging from 10 to 1000 can be obtained by combining Blake-Kozeny equation (Equation 5.8) and Burke-Plummer equation (Equation 5.9):

$$f = \frac{\Delta P d_p \epsilon^3}{L \rho V_f^2 (1 - \epsilon)} = 150 \frac{(1 - \epsilon)}{V_f d_p \rho / \mu} + 1.75 \quad (5.10)$$

From the Burke-Plummer equation (Equation 5.10), the pressure gradient can be written as

$$\frac{\Delta P}{L} = \frac{\rho V_f^2 (1 - \epsilon)}{d_p \epsilon^3} \left[150 \frac{(1 - \epsilon) \mu}{V_f d_p \rho} + 1.75 \right] \quad (5.11)$$

5.2 Porous Media Permeability Equation

The Ergun equation is designed for packed beds and does not apply for porosities greater than 50% as it does not consider form drag losses which are small at low porosities. Most of the filter materials composed of microfibrinous materials have high

porosity greater than 80% [17]. The viscous form drag losses are calculated using Stokes' law and are added to the viscous friction losses which improve the agreement of the Ergun equation for high voidage materials. This modified Ergun equation is called Porous Media Permeability (PMP) equation and was derived by Cahela et al. [3].

The porous media can be modeled as a collection of capillaries of length L_e . The interstitial velocity (V_i) can be written as

$$V_i = \frac{\Delta P r_h^2}{2\mu L_e} . \quad (5.12)$$

Since the particles in the porous media are not smooth spheres, an equivalent diameter is defined base on the shape factor (ϕ) as $d_{eq} = \phi d_p$ where $\phi = \frac{6}{d_p a_v}$.

Incorporating the shape factor in to the hydraulic radius (Equation 5.2) results in

$$r_h = \frac{\epsilon d_{eq}}{6(1-\epsilon)} = \frac{\epsilon(\phi d_p)}{6(1-\epsilon)} . \quad (5.13)$$

It is observed that the interstitial velocity for a porous bed is greater than the face velocity divided by void fraction [81]. Fluid flowing through a tortuous path travels more distance than just the length of the porous bed. For a tortuous path in

a porous media one finds that

$$\left\{ \begin{array}{l} \text{Time to travel distance } L \\ \text{at a velocity } V_f/\epsilon \end{array} \right\} = \left\{ \begin{array}{l} \text{Time to travel a tortuous path of} \\ \text{length } L_e \text{ at a velocity } V_i \end{array} \right\}$$

Thus,

$$\frac{L\epsilon}{V_f} = \frac{L_e}{V_i} \Rightarrow V_i = \frac{V_f\tau_t}{\epsilon} \text{ or } V_i = \frac{V_f}{\epsilon} \left(\frac{L_e}{L} \right). \quad (5.14)$$

Tortuosity (τ_t) of the porous media is estimated using a cubic cell with one sphere in the center and is defined as

$$\tau_t = 1 + (1 - \epsilon)/2. \quad (5.15)$$

The orientation of fibers in a fixed bed also affects the interstitial velocity [82]. Let θ be the angle between the flow direction (r) and perpendicular direction through the bed (x), then

$$\begin{aligned} dx &= dr \cos \theta \Rightarrow V_x = V_r \cos \theta \\ V_i &= \frac{V_f\tau_t}{\epsilon \cos \theta} \end{aligned} \quad (5.16)$$

By substituting V_i and r_h into Equation 5.12 we get

$$\frac{V_f \tau_t}{\epsilon \cos \theta} = \frac{\Delta P}{L} \left(\frac{L}{L_e} \right) \left[\frac{\epsilon (\phi d_p)}{6(1-\epsilon)} \right]^2 \frac{1}{2\mu} \quad (5.17)$$

$$\frac{\Delta P}{L} \Big|_{Friction Losses} = 72 \frac{\tau_t^2}{\cos^2 \theta} \frac{\mu V_f (1-\epsilon)^2}{\epsilon^3 (\phi d_p)^2} \text{ since, } \frac{L}{L_e} = \frac{\cos \theta}{\tau_t} \quad (5.18)$$

The above equation accounts only for friction losses. From Stokes law, the force on the sphere in a laminar flow is given by,

$$F = 6\pi\mu R V_\infty = \pi\mu d_p V_i \quad (5.19)$$

The pressure loss due to form drag per tortuous bed length is the product of form drag force per particle and the number of particles per volume of bed. The number of particles per volume of bed is the ratio of volume fraction occupied by particles to the volume of one particle [17]:

$$\frac{\Delta P}{L} \Big|_{Form Drag Losses} = 6 \frac{\tau_t^2}{\cos^2 \theta} \frac{\mu V_f (1-\epsilon)^3}{\epsilon (\phi d_p)^2} \quad (5.20)$$

Total pressure drop due to viscous losses is the sum of the friction losses (Equation 5.17) and form drag losses (Equation 5.20)

$$\begin{aligned} \frac{\Delta P}{L} \Big|_{Viscous Losses} &= \frac{\Delta P}{L} \Big|_{Friction Losses} + \frac{\Delta P}{L} \Big|_{Form Drag Losses} \\ &= 72 \frac{\mu V_f}{\epsilon^3} \frac{\tau^2}{\cos^2 \theta} \frac{(1-\epsilon)^2}{(\phi d_p)^2} \left[1 + \frac{1}{12} \frac{\epsilon^2}{(1-\epsilon)} \right]; \quad \frac{\epsilon^2}{12(1-\epsilon)} = x_{FD} \end{aligned} \quad (5.21)$$

Microfibrous materials generally consist of a matrix of fibers containing particles. Cahela et al. [17] derived an equation to predict the pressure drop through a mixture of fibers and particulates by defining an equivalent diameter based on total surface area and total volume of the particles as

$$\frac{1}{d_{eq}} = \frac{SA_p}{6 Vol_p} = \sum \frac{x_i}{\phi_i d_i}. \quad (5.22)$$

An equivalent hydraulic radius can be defined as:

$$r_h = \frac{\epsilon}{6(1-\epsilon) \sum \frac{x_i}{(\phi d_i)}} \quad (5.23)$$

Finally, the total pressure drop for laminar flows through a mixture of solid particles and fibers of any shape and size is given by:

$$\frac{\Delta P}{L} = 72 \mu V_f \frac{\tau_t^2}{\cos^2 \theta} \frac{(1-\epsilon)^2}{\epsilon^3} \left[\left(\sum \frac{x_i}{\phi_i d_i} \right)^2 + x_{FD} \sum \frac{x_i}{(\phi_i d_i)^2} \right] \quad (5.24)$$

Equation 5.24 is called the porous media permeability (PMP) equation.

CHAPTER 6

NUMERICAL MODELING

6.1 Geometric Modeling

GAMBIT, a commercial pre-processor is used to generate geometric models used in this study. FLUENT, a commercial CFD code, is used to solve the discretized governing equations. For post-processing the results obtained from FLUENT, TEC-PLOT is used.

6.1.1 Geometric Approximations

A simplified 3D geometric approximation for the microfibrous material is used in the CFD simulations and is shown in Figure 6.1 .

The straight cylindrical fibers and spherical particles are evident in the isometric view, and the regular orientation of the fibers in the domain is shown in the front view. The geometric approximations made while modeling the microfibrous material are:

1. The sorbent/catalytic particles are assumed to be spherical in shape and are arranged in a regular matrix.
2. The fibers are assumed to be straight cylinders.

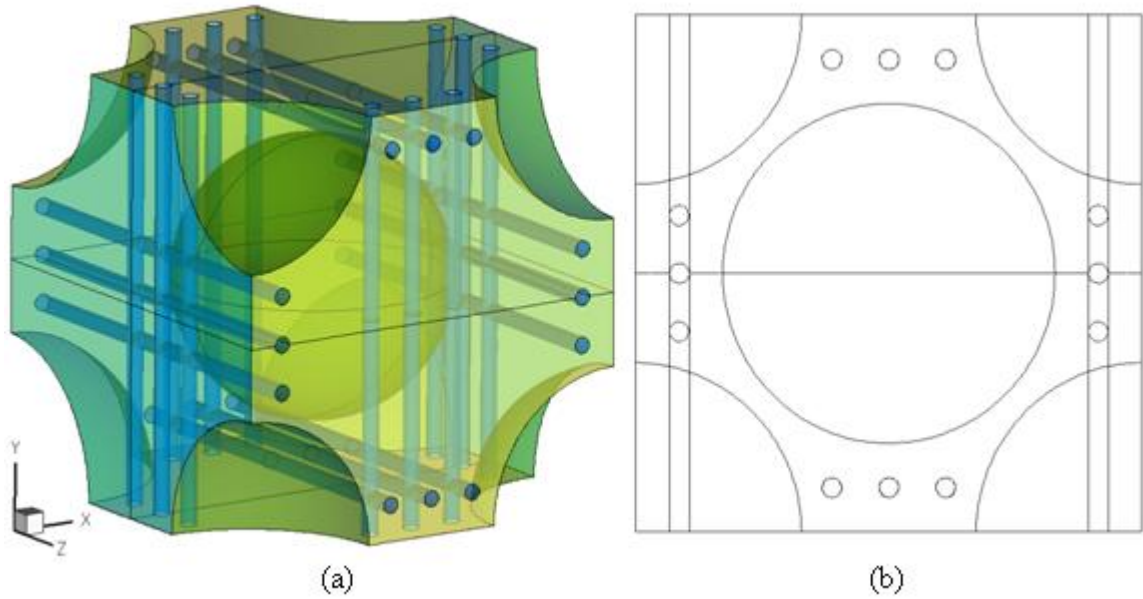


Figure 6.1: Geometric simplifications of the microfibrillar materials used in the simulations: (a) isometric view and (b) front view

3. Only one size of cylindrical fibers is considered instead of varying fiber diameters that found in the microfibrillar materials.
4. The fibers are oriented perpendicular to the flow direction, parallel to Y and Z axes (flow is in positive X direction).
5. The fibers oriented parallel to Y and Z axes intersect each other, whereas in reality the fibers may touch each other but they do not intersect.
6. The length to height ratio of each unit cell is assumed to be unity.

With all of these approximations, the 3D unit cell of simulation model (Figure 6.1) is assembled using the boundary conditions (to be discussed later) and is shown in Figure 6.2. In Figure 6.2(a), the dark irregular shapes labeled as ACP are the sorbent/catalytic particles and the light colored wires labeled as Ni Fibers are the microfibers. In Figure 6.2(b), the blue spheres represent sorbent/catalytic particles and the grey cylinders represent the microfibers.

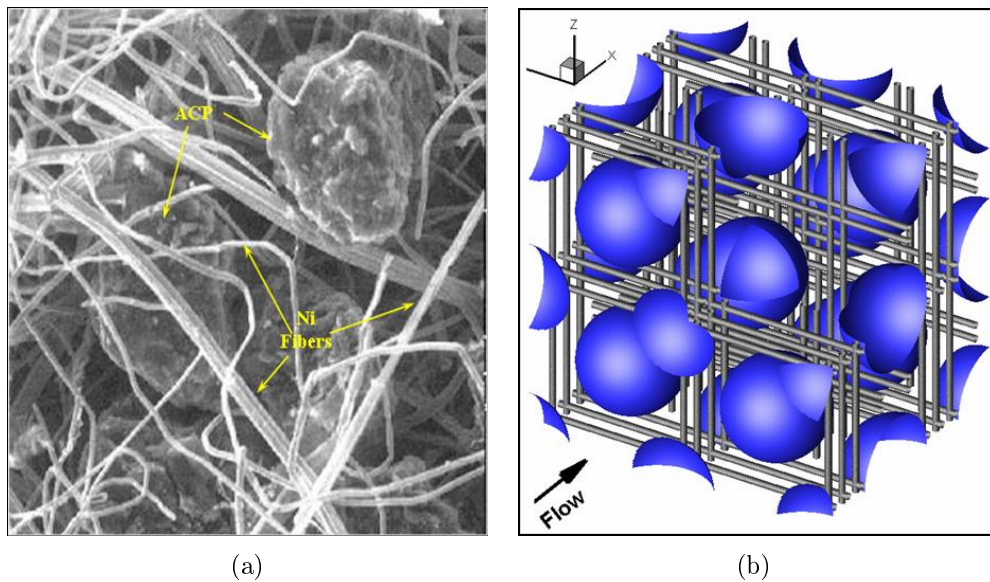


Figure 6.2: (a) SEM of a typical microfibrinous material (from CM^3); (b) CFD model of the microfibrinous material

6.1.2 Flow-field Mesh

The grid generator GAMBIT is used to create a volume mesh in the fluid domain. An unstructured mesh consisting of tetrahedral volumetric elements in 3D is used in

the entire domain except around the fibers and the particles, where a boundary layer mesh consisting of prismatic volumetric elements is used.

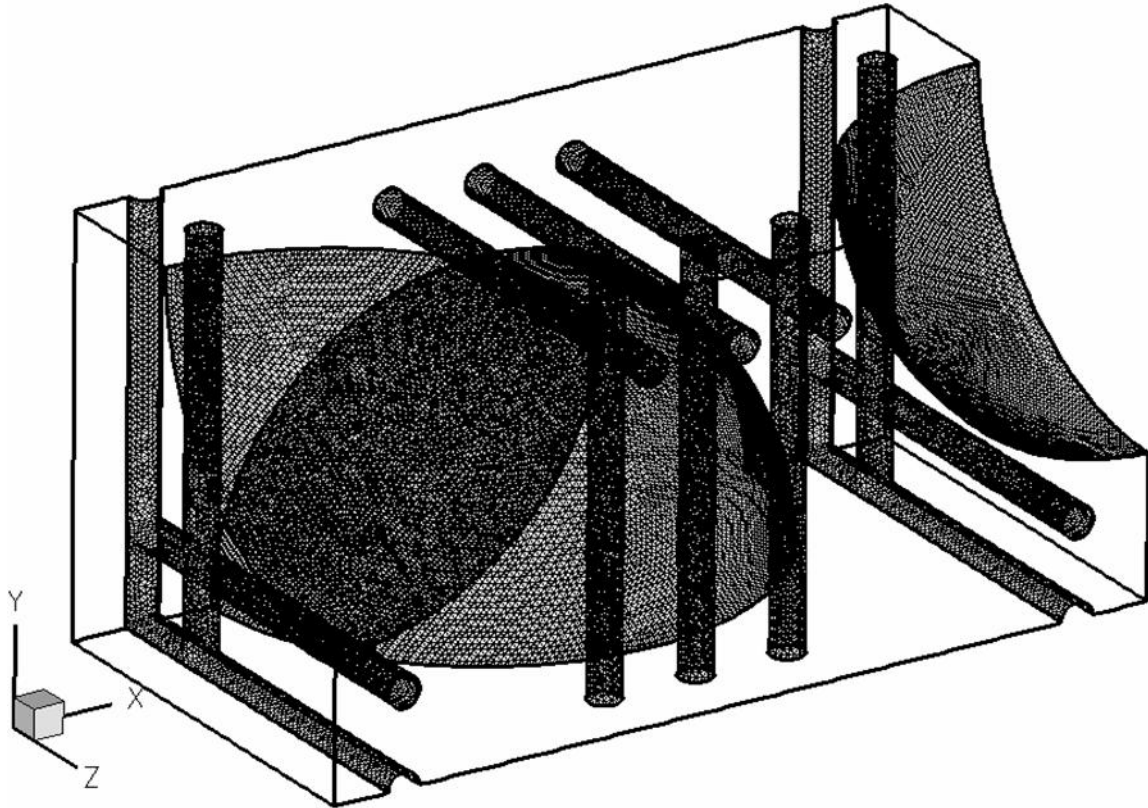


Figure 6.3: Triangular mesh on the fiber and particle walls

Figure 6.3 shows a sample mesh consisting of triangular elements on the particle and fiber walls of the modeled microfibrillar material. Figure 6.4 shows the unstructured mesh on the top symmetry face along with the prismatic boundary layer mesh around the fiber and the particle (in the enlarged region at the right).

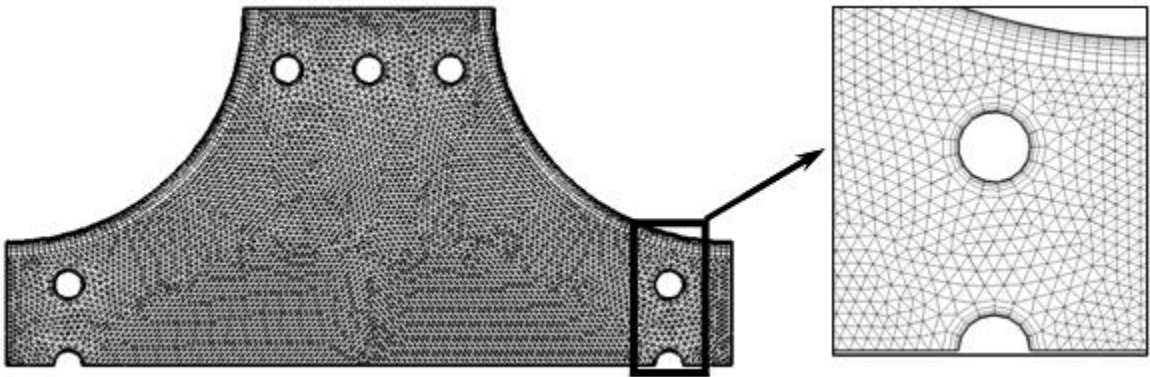


Figure 6.4: Triangular mesh on the top symmetry face with a prismatic boundary layer mesh around the particles and the fibers

The effect of using a boundary layer mesh around the fibers and particles is also examined by considering a case with an unstructured mesh in the entire domain. Pressure drops on the structured and unstructured mesh around the fibers and the particles varied by up to 2-8%; moreover, the unstructured mesh results had significantly larger numerical error as estimated by a grid refinement study. The accuracy of the fully tetrahedral mesh results could be increased by refining the mesh, but the additional refinement is expensive in both computation cost and solution time. As a result, a prismatic boundary layer mesh is used around the fibers and the particles to reduce the computation cost and to improve numerical accuracy.

6.1.3 Boundary Conditions

Different boundary conditions used in this study are:

1. Periodic

2. Symmetry
3. Velocity-slip
4. No-slip
5. Velocity inlet
6. Outflow
7. Inlet diffusion

A detailed description of each boundary condition is given in this section.

PERIODIC BOUNDARY CONDITION: Periodic boundary conditions are used when the physical geometry of interest and the expected pattern of the flow have a periodically repeating nature [53]. Since the velocities are periodic in the X direction, the inlet and outlet planes are linked as periodic boundary conditions, which enforces periodicity of the velocity but allows a pressure drop.

SYMMETRY BOUNDARY CONDITION: Symmetry boundary conditions are used when the physical geometry of interest, and the expected pattern of the flow have mirror symmetry [53]. By employing symmetry arguments, only one-quarter of the total domain shown in Figure 6.1 is modeled to reduce the computational effort and a symmetry boundary condition is used on all four sides (which are parallel to the flow).

VELOCITY-SLIP WALL BOUNDARY CONDITION: The Knudsen number based on the fiber diameter ranges between $0.001 < \text{Kn} < 0.1$. In this slip regime ($\text{Kn} > 0.01$), the gas-phase velocity at the solid surface is no longer zero. Surfaces of the fibers and particles are defined as high Knudsen number slip walls by enabling the low-pressure slip boundary formulation in Fluent, which uses the first-order Maxwell velocity-slip boundary condition [5]:

$$U_s - U_w = \frac{2 - \sigma_v}{\sigma_v} \lambda \frac{\partial U}{\partial n} \quad (6.1)$$

NO-SLIP WALL BOUNDARY CONDITION: For viscous flows with $\text{Kn} \leq 0.01$, the no-slip boundary condition is enforced at the walls.

VELOCITY INLET BOUNDARY CONDITION: Velocity inlet boundary conditions are used to define the flow velocity and concentration along with all flow properties at the inlet. Also inlet is defined as diffusion inlet. As we are using segregated solver in FLUENT, a commercial CFD code, the net transport species at inlet is due to convection and diffusion. The convection transport is fixed by the inlet species concentration (defined as inlet concentration) and diffusion is obtained from the gradient of computed species at the inlet [53].

OUTFLOW BOUNDARY CONDITION: Outflow boundary conditions are used to model flow exits where the details of the flow velocity and pressure are not known prior to solution of the flow problem. At outflow boundaries, all of the necessary boundary information is extrapolated from the interior.

INLET DIFFUSION: The fluid inlet has been defined as a velocity inlet where we define the velocity and concentration of the challenge gas. Also inlet is defined as diffusion inlet. The net species transport at an inlet boundary consists of two terms: convective flux and diffusive flux. The convective flux is determined by the inlet properties (i.e., velocity and concentration) of the challenge gas as the product of velocity and concentration. The diffusive flux is determined by the concentration gradient from the interior using the Equation 6.2.

$$J = D_{AB} \frac{\partial C}{\partial x} \quad (6.2)$$

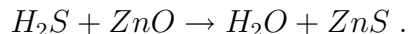
When inlet diffusion is turned off, i.e., if the concentration gradient is set to zero, then diffusive flux vanishes and net species transport is equal to convective flux. In this case, concentration at the inlet boundary will be constant (inlet concentration) and inlet is treated as a reservoir or infinite source. When the inlet is an infinite source, it can result in a very large species gradients near the inlet which results in large diffusive flux at the boundary and this is physically incorrect.

When inlet diffusion is turned on, i.e., if the concentration gradient is extrapolated from the interior, the net species flux is the sum of convective and diffusive fluxes. In this case, the concentration at the inlet boundary will be less than the specified concentration. Various numerical experiments were conducted to analyze the effects of inlet diffusion (see Appendix B). It was observed that inlet diffusion has no effect if the inlet is far way from the reactor. However, when the inlet is close to the reactor, enabling inlet diffusion effectively assumes a virtual inlet far away from the reactor and agrees well with the long entrance length case, while turning off inlet diffusion produced spurious results.

6.2 Modeling Species Transport/ Chemical Reactions

For gas-phase reactions, the reaction rate is defined based on volume and rate of reaction (creation or destruction of chemical species) and becomes a source term in the species conservation equations. This study is focused on both desulphurization of hydrogen using metal zinc oxide and removal of hexane from air. Species transport equations are solved to obtain steady-state solutions for both desulfurization and hexane removal.

DESULFURIZATION: The reaction used to model the desulphurization reaction



The spherical particles are assumed to be made of silica (SiO_2) with a zinc oxide (ZnO) coating on it. 2% H_2S mixed with H_2 at 400°C is used as challenge gas. According to Weiz-Pratar criteria (discussed in Appendix B.1), it is assumed that all the zinc oxide is on the surface of the particle and the reaction is modeled as catalytic surface reaction. The reaction rate constant is obtained by calibrating with experiments at high face velocity, and this process will be discussed in detail in 7.

HEXANE REMOVAL: In practice, the hexane reaction rate changes with time: as the catalyst gets polluted by hexane the reaction rate decreases. Before the surface is polluted, the reaction is assumed to be infinitely fast. For infinitely fast reactions, the concentration of species can be fixed to zero at the surface of the particle. 100 ppmv (parts per million by volume) of hexane in air at 40°C is used as the challenge gas and the concentration of hexane on the surface of the particles is set to zero.

CHAPTER 7

RESULTS AND DISCUSSION

7.1 Pressure Drop Predictions

Pressure drop is predicted in packed beds, immobilized beds, and microfibrinous materials. The predicted pressure drop is compared to empirical correlations (Ergun [Equation 5.11] and PMP [Equation 5.24]). For the case of microfibrinous materials, the pressure drop is also compared with experimentally measured values. In this section results are analyzed and the numerical accuracy will also be discussed.

PROCEDURE: The procedure followed for all the pressure drop simulations is the same and is discussed here. An iterative solution approach is employed where the solution is advanced in pseudo-time until the steady-state equations are satisfied to a specified tolerance. At each iteration the governing equations are solved using a segregated solver. A finite volume technique is used to solve the discrete form of the governing equation on the computational grid. The standard SIMPLE algorithm is used in which the momentum equations are first solved for the velocity components. A pressure correction is then determined which drives the velocity field towards satisfying the mass conservation equation.

Iterative convergence is assessed by monitoring the L_2 norms of the steady-state residuals. The convergence criterion is set to 10^{-7} for all conservation equations. The iterative error in the pressure drop is found by comparing the pressure drop at the current iteration to the converged pressure drop (residuals $\sim 10^{-7}$):

$$\% \text{ Error in } \frac{\Delta P}{L} \text{ } i^{\text{th}} \text{ iteration} = 100 \times \left| \frac{\left(\frac{\Delta P}{L} \right)_{\text{converged}} - \left(\frac{\Delta P}{L} \right)_{i^{\text{th}} \text{ iteration}}}{\left(\frac{\Delta P}{L} \right)_{\text{converged}}} \right| \quad (7.1)$$

Due to difficulties in converging the residuals to 10^{-7} using the second-order spatial discretization, the following procedure is used to converge the solution in all cases. Initially for these simulations, a first-order upwind scheme is used to discretize the conservation equations. The solution is then converged to a relative tolerance of 10^{-3} using the first-order upwind spatial discretization scheme. At this point, a second-order discretization scheme is used to discretize the conservation equations and the solution is then converged to a relative tolerance of 10^{-7} .

As the original conservation equations are discretized, the numerical solution will not match with the exact solution to the partial differential equations. The difference between the numerical solution and the exact solution is called discretization error. The discretization error is usually the primary source of numerical errors in CFD

simulations. The exact solution for the pressure drop per unit length can be estimated using generalized Richardson extrapolation [83] is given by Equation 7.2.

$$\frac{\Delta P}{L} \Big|_{exact} = \frac{\Delta P}{L} \Big|_1 + \frac{\frac{\Delta P}{L} \Big|_1 - \frac{\Delta P}{L} \Big|_2}{r^{p'} - 1} \quad (7.2)$$

Once the exact solution has been estimated, the relative discretization error (RDE) in the fine grid solution can be estimated using Equation 7.3

$$RDE = \frac{\frac{\Delta P}{L} \Big|_1 - \frac{\Delta P}{L} \Big|_{exact}}{\frac{\Delta P}{L} \Big|_{exact}} \times 100\% \quad (7.3)$$

The generated flow-field grids along with Equations 7.2 and 7.3 are used to estimate the discretization error for all pressure drop simulations. The quantity p' in Equation 7.2 is set to the formal order of accuracy of two.

The accuracy of the estimated exact solution for pressure drop per unit length can be determined by comparing the observed order of accuracy with the formal order. The formal order of accuracy is determined by a truncation error analysis, and is defined as the order of the leading term of the truncation error obtained in the process of discretizing the governing equations. The observed order of accuracy is the order of accuracy of the numerical solution which can be calculated using solutions on three grids as [84]:

$$\frac{\left. \frac{\Delta P}{L} \right|_3 - \left. \frac{\Delta P}{L} \right|_2}{r_{23}^{p''}} = r_{12}^{p''} \left(\frac{\left. \frac{\Delta P}{L} \right|_2 - \left. \frac{\Delta P}{L} \right|_1}{r_{12}^{p''} - 1} \right); r_{ij} = \sqrt[d]{\frac{NE_i}{NE_j}}; d = 3 \text{ for 3D} \quad (7.4)$$

All of the CFD simulation results discussed in this section are represented with error bands which are calculated using Roache's grid convergence index (GCI) [84]. Equation 7.5 is used to calculate the GCI to provide uniform reporting of the grid convergence study

$$GCI = \frac{F_s}{r^{p'} - 1} \left| \frac{\left. \frac{\Delta P}{L} \right|_2 - \left. \frac{\Delta P}{L} \right|_1}{\left. \frac{\Delta P}{L} \right|_1} \right| \quad (7.5)$$

where F_s is the factor of safety. The factor of safety is recommended to be $F_s = 3.0$ for comparisons of two grids and $F_s = 1.25$ for comparisons over three or more grids. The higher factor of safety is recommended for reporting purposes and is quite conservative of the actual errors. Subscripts 1, 2, and 3 represents fine, medium, coarse grids, respectively.

7.1.1 Packed Beds

The pressure drop is predicted numerically and compared with empirical correlations for typical packed beds with a solid fraction of 60% and 150 μm diameter spherical particles.

7.1.1.1 Numerical Accuracy

ITERATIVE ERROR: A sample residual history for the computation with a Reynolds number of 1.0 is shown in Figure 7.1. Residuals are plotted along the y-axis in log scale and the x-axis represents iterations.

We observe that the residuals decrease gradually with each iteration. There is a sudden rise when the residuals reach 10^{-4} as the discretization scheme is changed from first to second order (as mentioned above), then the residuals gradually decrease and approach 10^{-7} .

The iterative error in the pressure drop is found by comparing the pressure drop at the current iteration to the converged pressure drop (residuals $\sim 10^{-7}$) using Equation 7.1. The iterative error in the pressure drop is also shown in Figure 7.1.

We observe that the percentage error in the pressure drop (right axis) decreases gradually from each iteration and approaches 0.01% as the maximum residual (left axis) approaches 10^{-7} . The value of 10^{-7} is thus used as the residual convergence tolerance for all Reynolds numbers. For this residual convergence tolerance, the

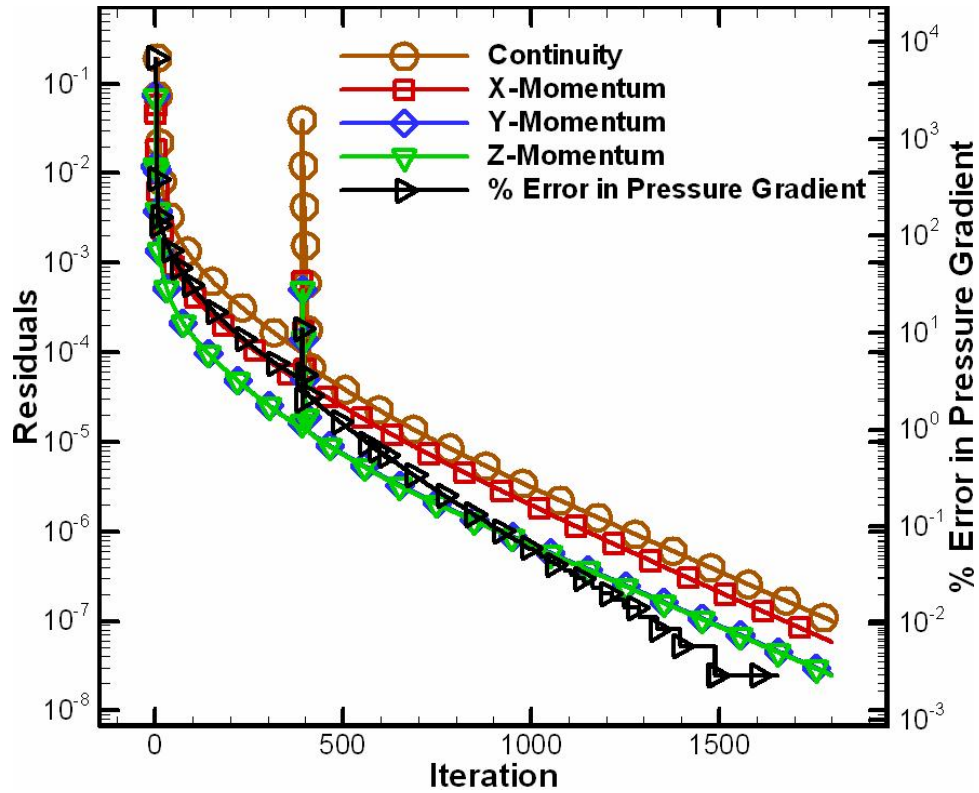


Figure 7.1: Convergence history and iterative convergence for a packed bed at $Re = 1.0$

iterative error in the pressure drop is estimated to be less than 0.01% and can thus be neglected.

DISCRETIZATION ERROR: A grid convergence study was conducted using three different grids. Starting from the coarse grid, medium and fine grids were obtained by refining with a factor of 1.5 in all three directions. The grid parameter h is defined as the cube root of the ratio of number of elements in fine grid to number of elements in i^{th} grid which gives $h=1$ for the fine grid.

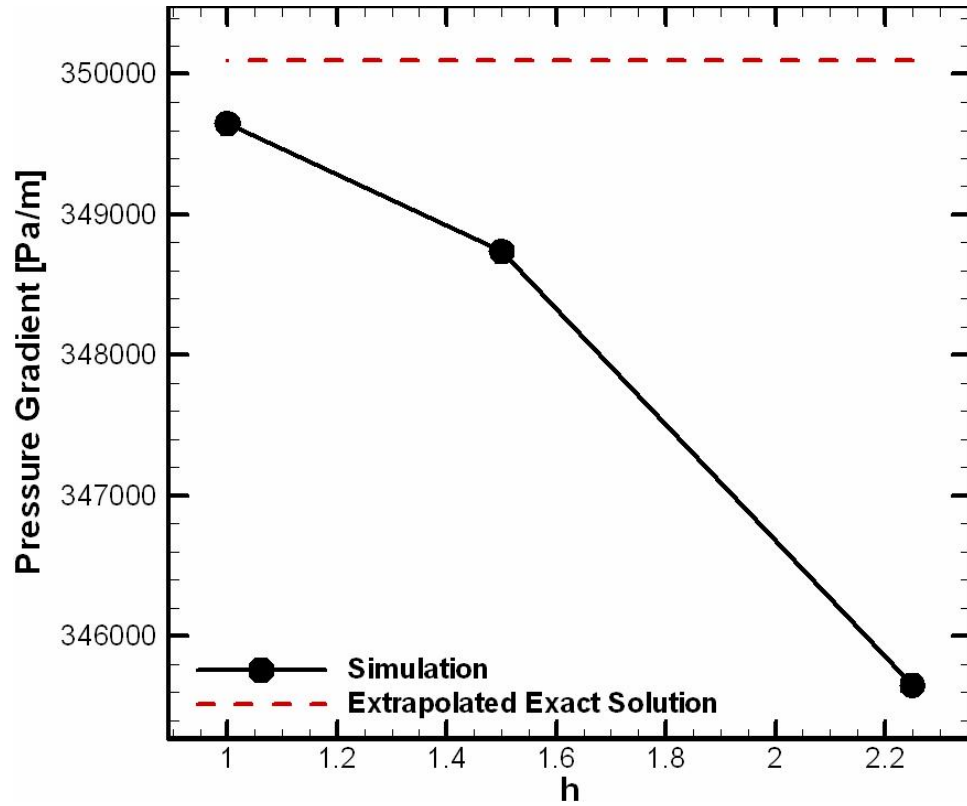


Figure 7.2: Grid convergence for packed bed at $Re = 1.0$)

In Figure 7.2 the pressure drop per unit length is plotted against the grid parameter for a Reynolds number of 1 to show that the solution is asymptotically converging as we refine the grid. Figure 7.2 also shows the estimated exact solution obtained from Richardson extrapolation using Equation 7.3.

The discretization error was calculated using Equation 7.2 for Reynolds numbers of 0.1 and 10 and is plotted against grid parameter in Figure 7.3.

In Figure 7.3, the slope of the line gives the observed order of accuracy. For the cases shown, the observed order of accuracy is around 3.

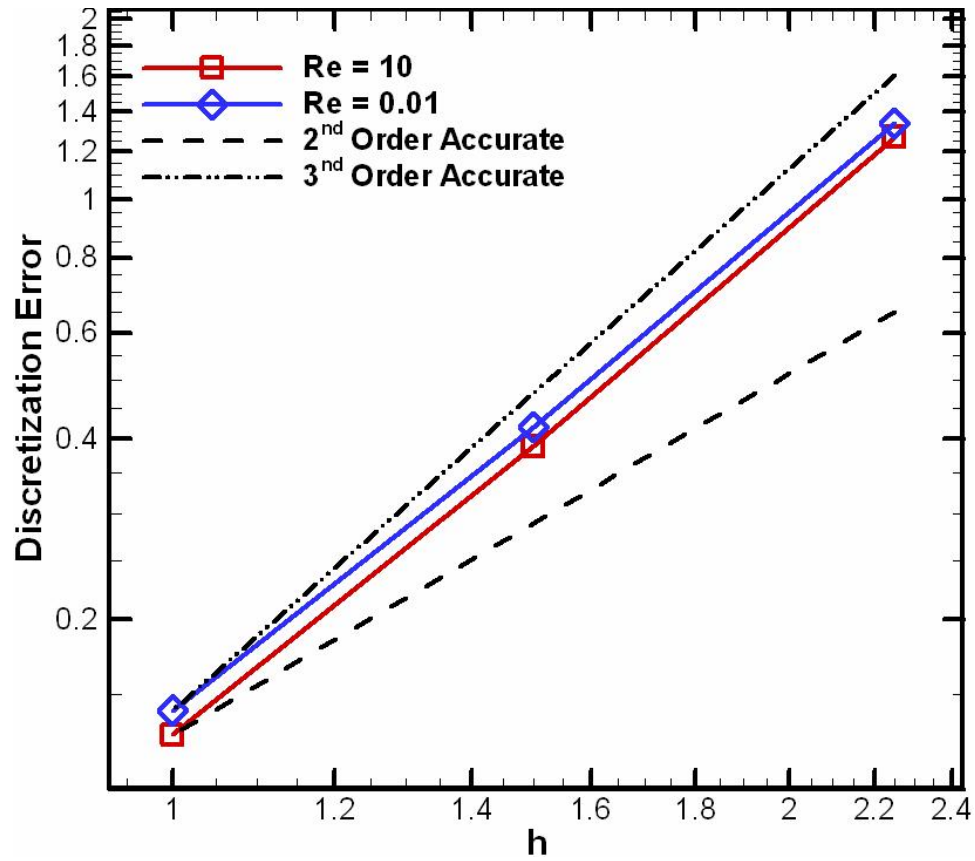


Figure 7.3: Discretization Error for a packed bed at $Re = 1.0$

Discretization error estimates for numerical simulations of packed beds are tabulated in Table 7.1 along with the details of the generated flow field grids and pressure gradients. It is observed that the estimated discretization errors range from 0.15% (fine grid) to 1.5% (coarse grid). Therefore, the medium grid is used for all packed bed simulations in this study.

Table 7.1: Discretization error in predicting pressure for packed bed

Re	Grid Level	No. of Elements	Pressure Gradient	Order of Accuracy	Exact Solution	Discretization Error [%]
10	Coarse	141,975	345,650.	2.99	350,099.95	1.27
	Medium	465,577	348,740.			0.38
	Fine	1,410,047	349,650.			0.12
0.01	Coarse	141,975	342.25	2.93	346.88961	1.33
	Medium	465,577	345.44			0.41
	Fine	1,410,047	346.40			0.14

7.1.1.2 Results and Model Validation

CFD simulations are performed using the generated flow-field meshes in order to predict the pressure drop and analyze the details of the flow in packed beds. A $Y=constant$ plane is extracted at the center of the domain from simulations with Reynolds number of 1 and velocity magnitude and pressure contours are shown in Figures 7.4 and 7.5, respectively.

The challenge gas (air) is flowing with an interstitial velocity of 1 cm/s. Contours of velocity magnitude given in Figure 7.4 show that the flow speeds up when the particles are close. The ratio of peak velocity to interstitial velocity is approximately ten for a Reynolds number of 1.

Figure 7.5 show a gradual decrease in pressure across the length of the domain. Figure 7.5 also shows that a larger gradients of pressure is observed between the particles. The pressure gradient for the case represented ($Re = 1$) is 34.58 KPa/m.

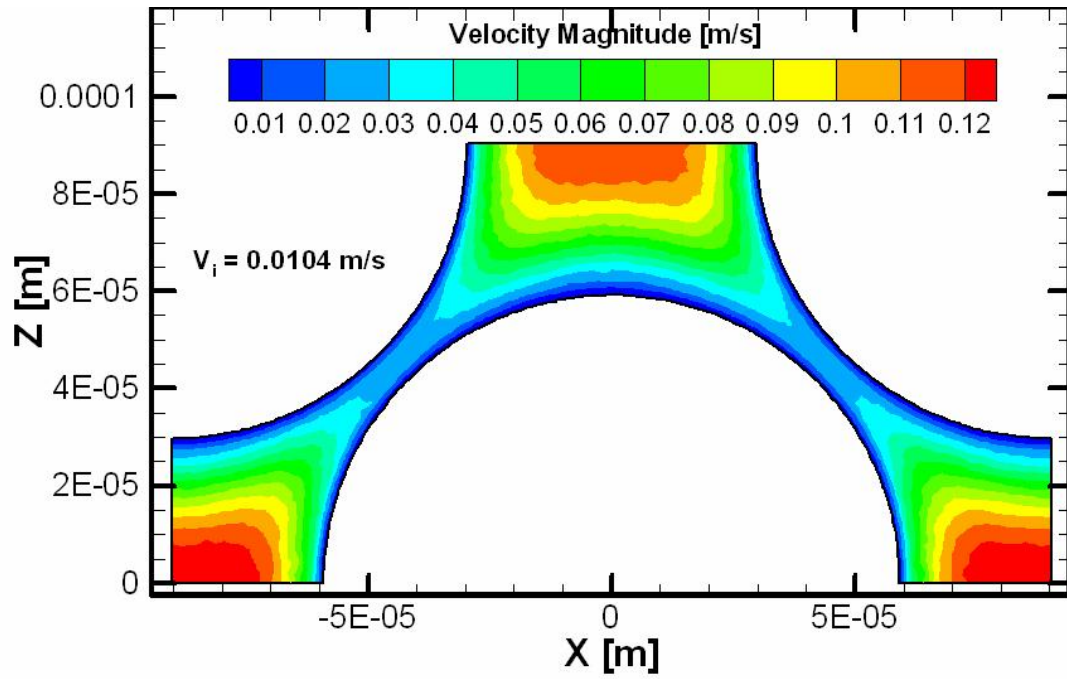


Figure 7.4: Contours of velocity magnitude : $Re=1.0$

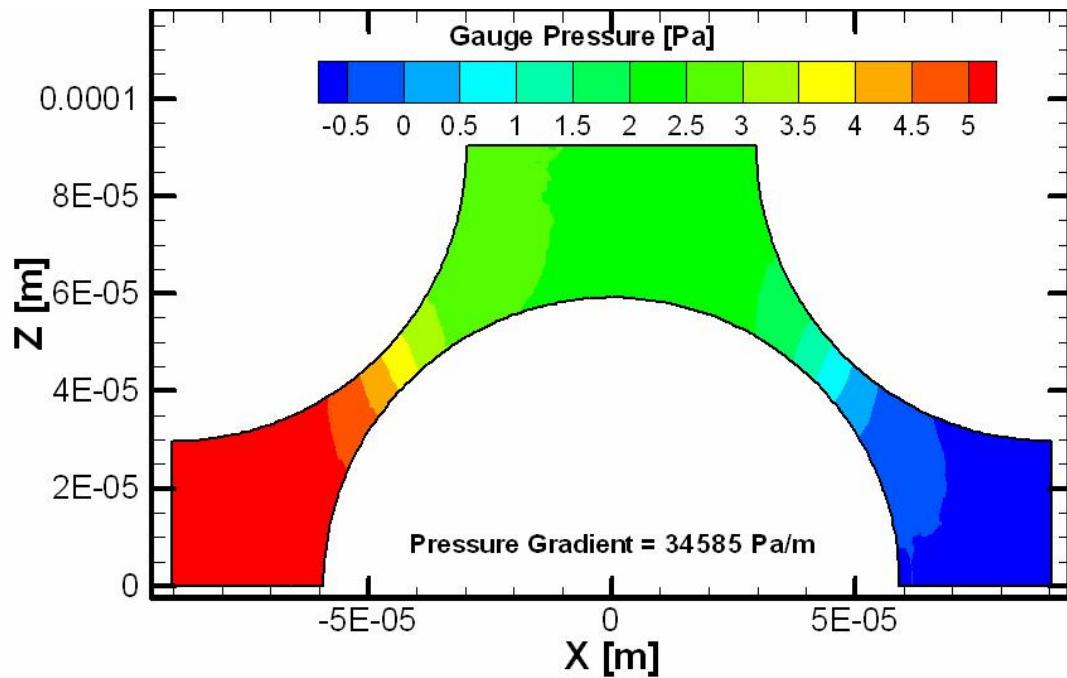


Figure 7.5: Contours of gauge pressure : $Re=1.0$

A similar analysis was performed with the planes extracted at a constant Z location (not shown here) and similar behavior was observed.

CFD predictions for the pressure drop per unit length for air flowing through packed beds are compared with the pressure from empirical correlations and those measured in the experiment [4] (for high Reynolds numbers only).

The pressure drop found from the CFD simulations, the PMP equation, and Ergun's equation is plotted against Reynolds number along with existing experimentally measured pressure drop and is shown in Figure 7.6 along with the numerical uncertainty (error bars) calculated using Richardson extrapolation (Equation 7.2). The CFD simulations are in good agreement with the empirical correlations in predicting pressure drop. Also Figure 7.6 shows that the CFD model used for predicting pressure drop shows good agreement with the experimentally measured pressure drop at high Reynolds numbers. The pressure drop obtained from CFD simulations is $\sim 20\%$ larger than that predicted by the Ergun and PMP equations for all Reynolds numbers, and is consistently 15-20% lower than from experimental measurements.

7.1.2 Immobilized Beds

Pressure drop was predicted numerically and compared with empirical correlations for immobilized/open beds whose solid fractions vary from 20% to 50% with a 150 μm (diameter) perfectly spherical particles. Note that these beds cannot actually

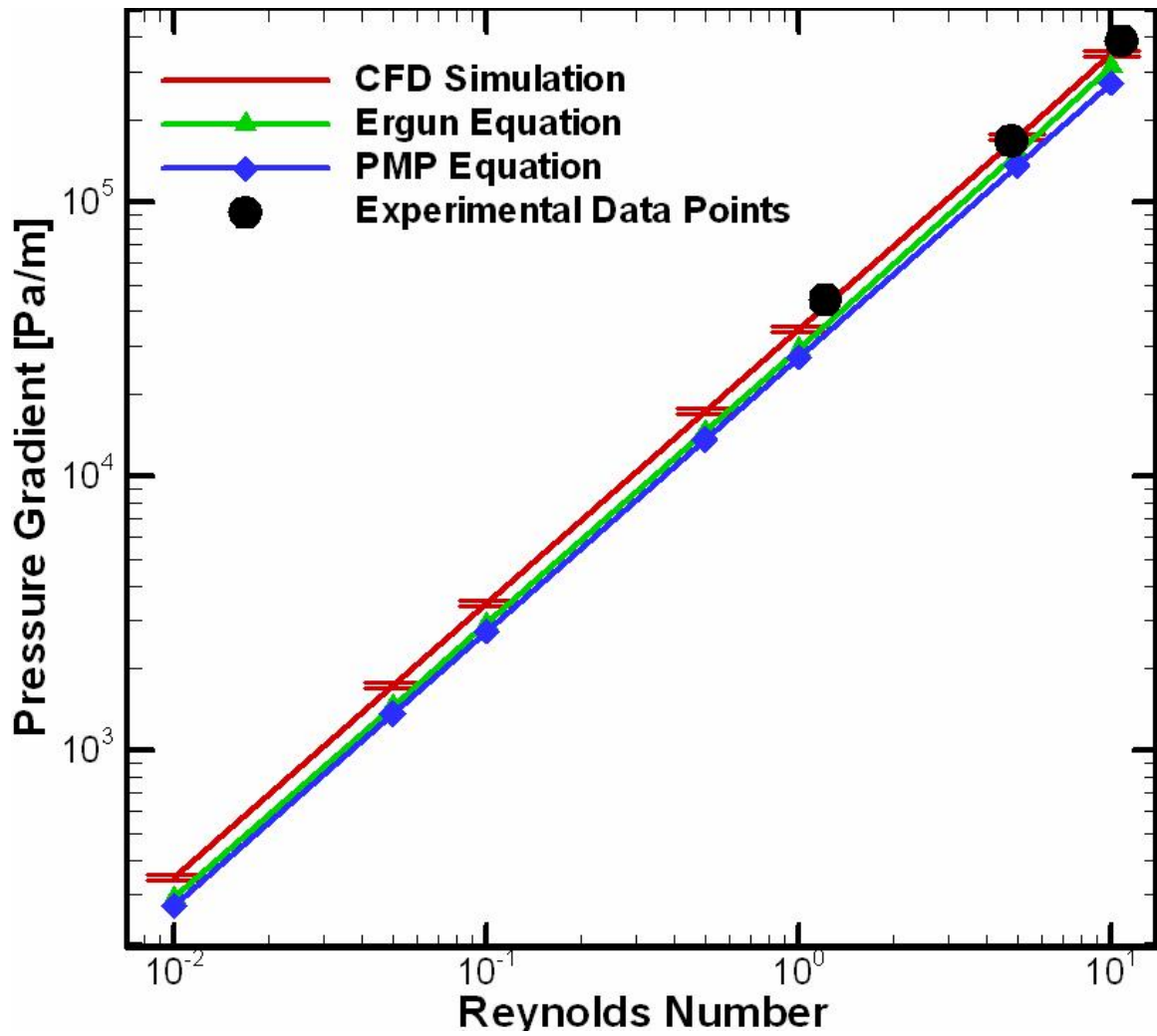


Figure 7.6: Pressure drop in packed beds obtained from simulations and empirical correlations compared with experimental data [4]; Numerical uncertainty = 0.5%

be built since the particles are effectively being "levitated" in space, a state that can be simulated but not reproduced experimentally.

7.1.2.1 Numerical Accuracy

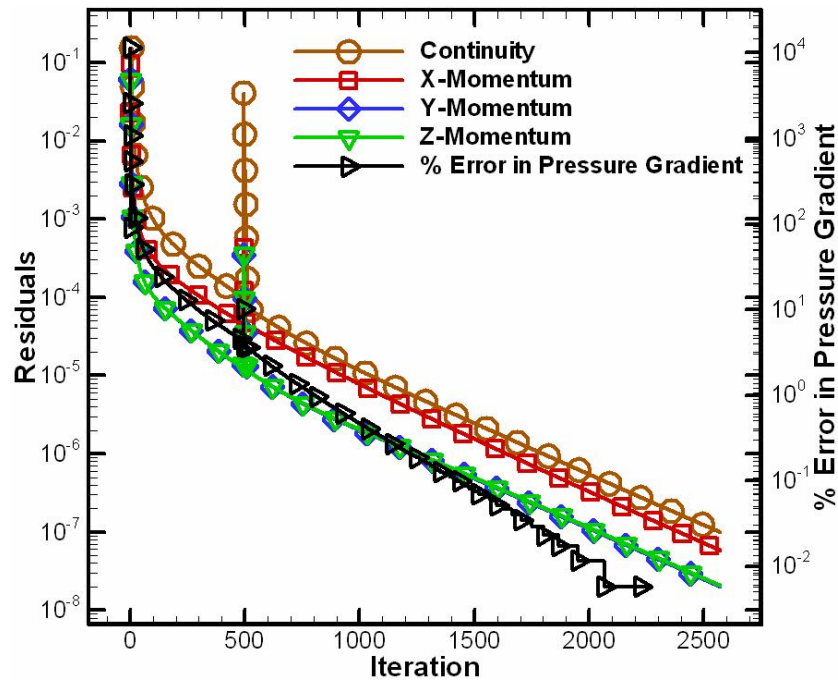


Figure 7.7: Convergence history and iterative convergence for immobilized bed ($\chi_p=30\%$ at $Re = 1.0$)

ITERATIVE ERROR: A sample residual history for the computation with a solid fraction of 30% at a Reynolds number of 1 is shown in Figure 7.7. We observe that the residuals decrease gradually with each iteration. There is a sudden rise when residuals reach 10^{-4} as the discretization scheme is changed from first to second order, then the residuals gradually decrease and approach 10^{-7} (as discussed above). The iterative

error in the pressure drop is found by comparing the pressure drop at the current iteration to the converged pressure drop (residuals $\sim 10^{-7}$) using Equation 7.1.

The iterative error in the pressure drop for the computation with a solid fraction of 30% at a Reynolds number of 1 is also shown in Figure 7.7. We observe that the percentage error in the pressure drop (right axis) decrease gradually from each iteration and approaches 0.001% as the maximum residual (left axis) approaches 10^{-6} . The value of 10^{-7} is thus used as the residual convergence tolerance for all the simulations presented herein. For this residual convergence tolerance, the iterative error in the pressure drop is estimated to be less than 0.01% and can thus be neglected relative to discretization (or grid-related) error.

DISCRETIZATION ERROR: Discretization error estimates in numerical simulations of immobilized beds are tabulated in Table 7.2 along with the details of the generated flow-field grids and pressure gradients. It is observed that the estimated discretization errors range from 1.7% (fine grid) to 2.7% (coarse grid) for the solid fraction of 50% and from 0.1% (fine grid) to 1.7% (coarse grid) for the solid fraction of 40% and from 0.12% (fine grid) to 2.4% (coarse grid) for the solid fraction of 30% and from 0.01% (fine grid) to 1.3% (coarse grid) for the solid fraction of 20%. This estimated discretization error provides guidance in choosing an appropriate grid. The medium grid is used for all solid fractions in this study which has maximum discretization error estimates of 2% for the cases examined.

Table 7.2: Discretization error in predicting pressure drop for immobilized beds

Re	Grid Level	No. of Elements	Pressure Gradient [Pa/m]	Order of Accuracy	Exact Solution	Discretization Error [%]
SOLID FRACTION = 50%						
10	Coarse	161,682	174,320.	0.7585	178,140.31	2.14
	Medium	487,330	175,250.			1.62
	Fine	1,513,253	175,970.			1.21
0.01	Coarse	161,682	172.57	0.6069	177.2687	2.65
	Medium	487,330	173.51			2.12
	Fine	1,513,253	174.28			1.68
SOLID FRACTION = 40%						
10	Coarse	194,484	87,807.	3.3914	89,353.27	1.73
	Medium	725,144	89,004.			0.39
	Fine	2,246,560	89,256.			0.10
0.01	Coarse	194,484	86.89	3.8077	88.4004	1.70
	Medium	725,144	88.12			0.32
	Fine	2,246,560	88.33			0.07
SOLID FRACTION = 30%						
10	Coarse	292,580	42,733.	1.6222	43,823.21	2.48
	Medium	1,113,484	43,294.			1.20
	Fine	3,425,514	43,535.			0.65
0.01	Coarse	292,580	42.22	3.2120	42.96	1.72
	Medium	1,113,484	42.78			0.41
	Fine	3,425,514	42.91			0.12
SOLID FRACTION = 20%						
10	Coarse	553,146	18,534.	6.05853	18,786.52	1.34
	Medium	1,964,744	18,767.			0.10
	Fine	694,055	18,785.			0.008
0.01	Coarse	553,146	18.12	7.1103	18.35	1.27
	Medium	1,964,744	18.34			0.06
	Fine	694,055	18.35			0.003

7.1.2.2 Results

As it is impossible to manufacture these immobilized/open bed, models used in CFD simulation of immobilized beds can not be validated. In this section, velocity and pressure contours in the immobilized beds at Reynolds number of 1 are analyzed. Pressure drop predicted from CFD simulations are compared with the empirical correlations (Equations 5.11 and 5.24).

A plane is extracted in the Y plane at the center of the domain from the simulations with Reynolds number of 1 and velocity magnitude and pressure contours are shown in Figures 7.8 and 7.9, respectively. Contours of velocity magnitude (Figure 7.8) show that the flow speeds up when the particles are close in the case of solid fraction = 50% but becomes more uniform as the solid fraction decreases to 20%. The ratio of peak velocity to face velocity is approximately five for a solid fraction of 50% and is decreased to two for a solid fraction of 20%. The flow is symmetric across $X = 0$ for all solid fractions at this low Re.

Figure 7.9 shows a gradual decrease in pressure across the length of the domain. The pressure drop across the length of the domain is small at low Reynolds numbers for all solid fractions though the contours look different for different solid fractions. A similar analysis was performed with the planes extracted at constant Z locations (not shown here) and similar behavior was observed.

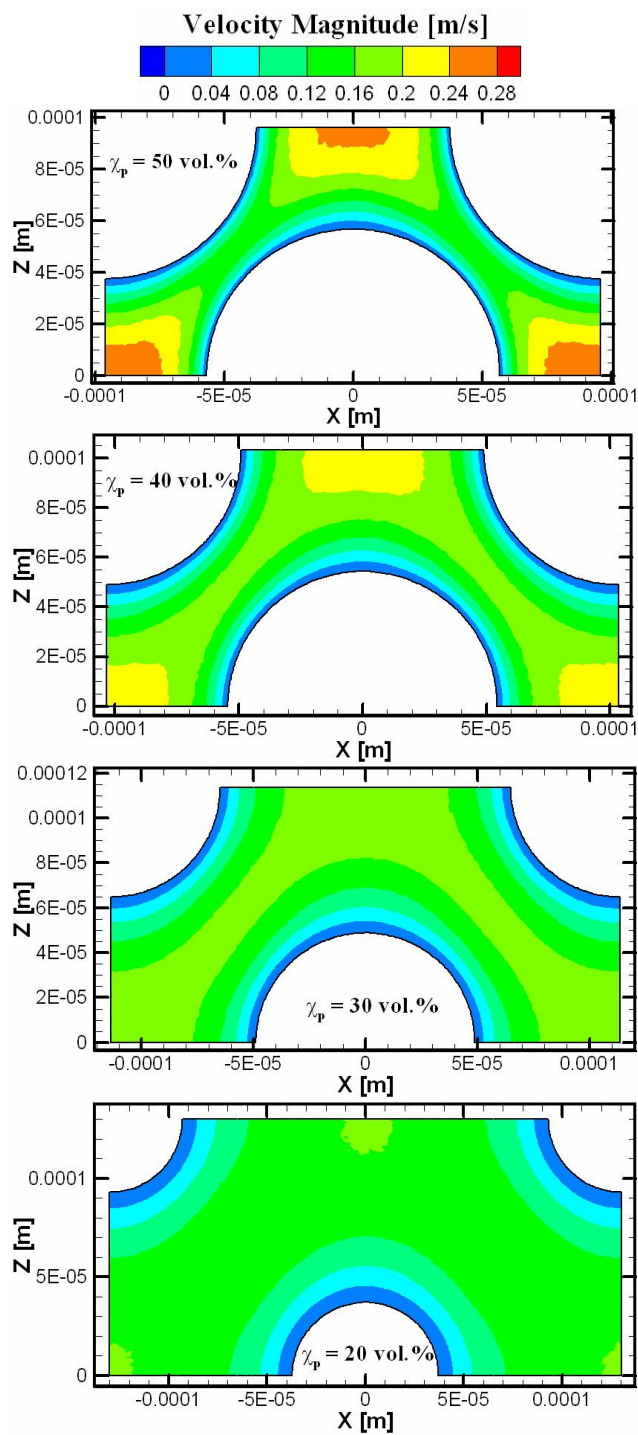


Figure 7.8: Velocity contours in constant Y-Plane for Immobilized beds

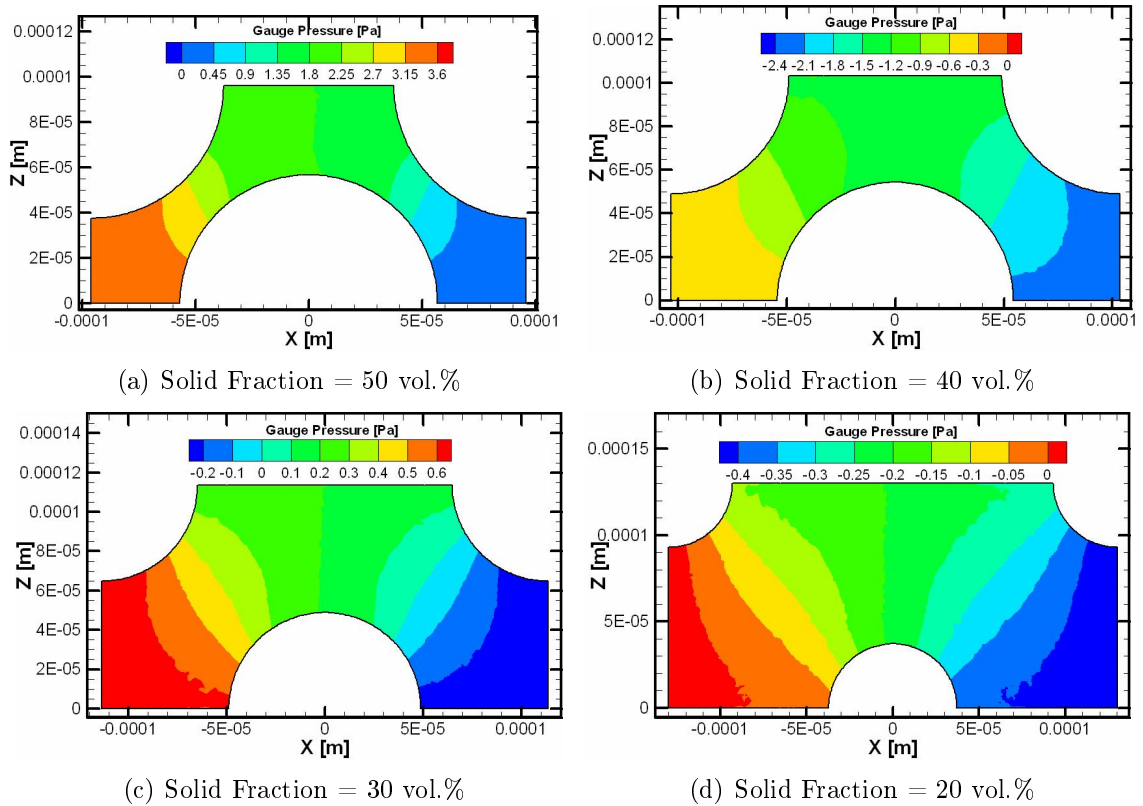


Figure 7.9: Pressure contours in constant Y-Plane for Immobilized beds

The pressure drops found from the CFD simulations, the PMP equation, and Ergun's equation are plotted against Reynolds number for all solid fractions and are shown in Figures 7.10 and 7.11. The CFD simulations are in good agreement with the empirical correlations in predicting pressure drop. Figures 7.10 and 7.11 also show with the numerical uncertainty (error bars) calculated using Richardson extrapolation (Equation 7.2). The pressure drop obtained from CFD simulations are 30% higher for solid fractions 50% and 40% and 40% higher for solid fractions 30% and 20% relative to the Ergun and PMP equations for all Reynolds numbers.

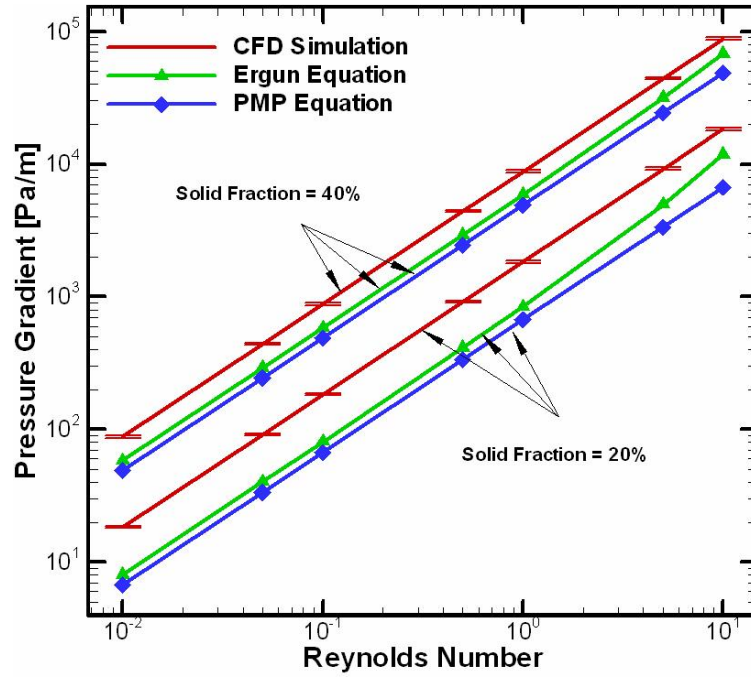


Figure 7.10: Comparison of pressure drop from simulations to empirical correlations ($\chi_p=20\%$ & 40% ; Numerical uncertainty = 1-2%)

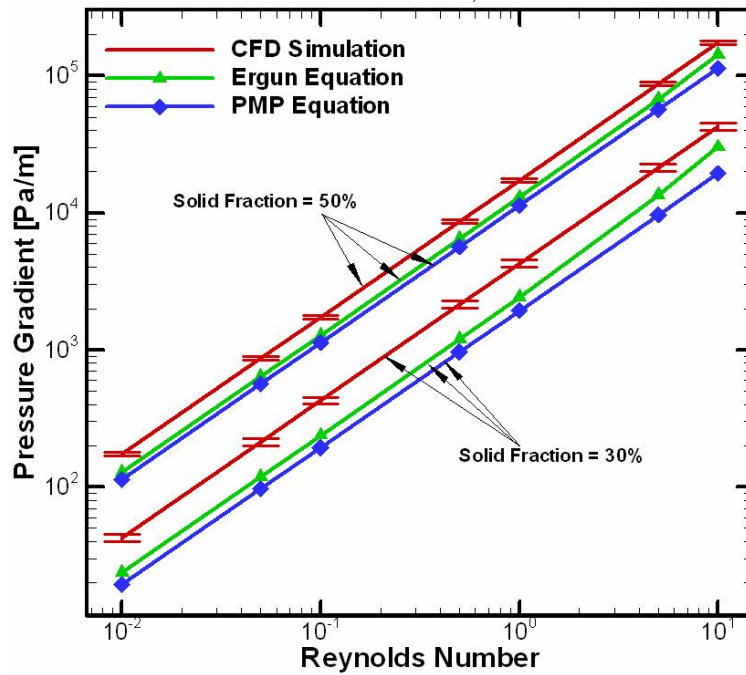


Figure 7.11: Comparison of pressure drop from simulations to empirical correlations ($\chi_p=30\%$ & 50%); Numerical uncertainty = 0.1-0.5%

7.1.3 Microfibrous Materials

This section is focused on the flow through microfibrous materials, a type of porous media. These microfibrous materials are a new class of composite materials developed by the Center for Microfibrous Materials Manufacturing (CM³) at Auburn University using traditional paper making techniques as discussed in section 3.3. Materials consisting of activated carbon powder (ACP) embedded into a mesh of nickel (Ni) and pyrolyzed cellulose (PC) fibers are used in this study. The particles are roughly spherical with diameters ranging between 100 μm and 150 μm whereas the fibers are roughly cylindrical with diameters ranging between 8 μm and 15 μm . Experiments were conducted by Cahela et al. [3] to measure the pressure drop in microfibrous materials consisting of fiber diameters of Ni and PC of 8 μm and 10 μm , respectively, and 100-120 mesh ACP. The solid volume percentages of ACP, Ni, and PC were 91.4%, 7.1%, and 1.5%, respectively. A detailed description of the materials used and the experimental setup is given in ref.[3] and experimentally measured pressure drop, as reported in ref.[3], have been discussed in Section 4.1.

Table 7.3: Properties of modeled microfibrous materials used in the CFD simulations

Material	Component	Diameter	Vol.%
Material-1	Particles	150 μm	54%
	Fibers	8 μm	5%
	Void		41%
Material-2	Particles	150 μm	48.5%
	Fibers	8 μm	4.5%
	Void		47%

7.1.3.1 Numerical Accuracy

ITERATIVE ERROR: A sample residual history for the computation with a solid fraction of 53% and a face velocity of 0.04 m/s is shown in Figure 7.12. We observe that the residuals decrease gradually with each iteration. There is a sudden rise when residuals reach 10^{-3} as the discretization scheme is changed from first to second order, then the residuals gradually decrease and approach 10^{-7} . The iterative error in the pressure drop is found by comparing the pressure drop at the current iteration to the converged pressure drop (residuals $\sim 10^{-7}$) using Equation 7.1.

The iterative error in the pressure drop is also shown in Figure 7.12. We observe that the percentage error in the pressure drop (right axis) decrease gradually from each iteration and approaches 10^{-2} as the maximum residual (left axis) approaches 10^{-6} . The value of 10^{-7} is thus used as the residual convergence tolerance for all the simulations presented herein. For this residual convergence tolerance, the iterative error in the pressure drop is estimated to be less than 0.001% and can thus be neglected.

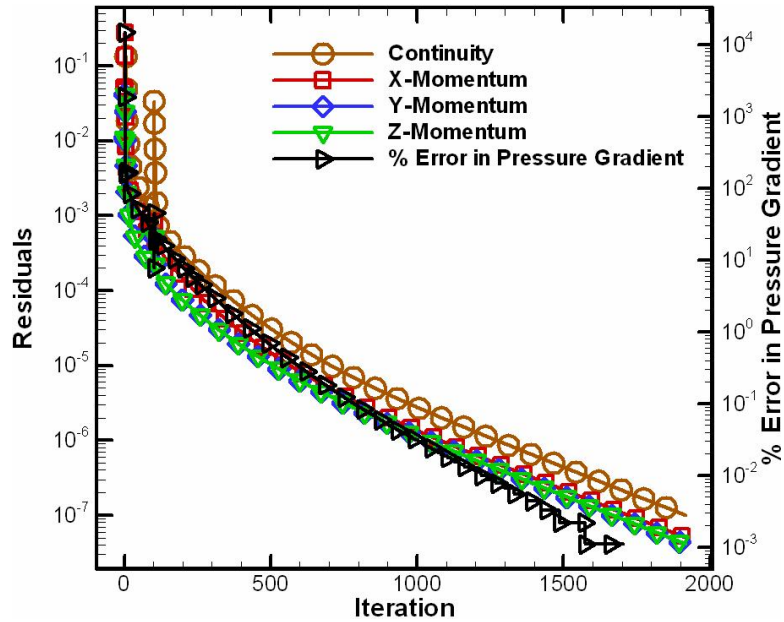


Figure 7.12: Iterative convergence for microfibrous materials ($\chi_p=53\%$ at $V_f = 0.04$ m/s)

DISCRETIZATION ERROR: Three flow-field grids were generated by uniformly refining each cell in the domain by a factor of 1.5 in all three directions (X, Y, and Z). The exact solution for the pressure drop per unit length can be estimated from generalized Richardson extrapolation [84] using Equation 7.2. Relative discretization error for solid fraction of 59% and 53% was plotted against the grid parameter to estimate the order of accuracy and is shown in Figures 7.13 and 7.14, respectively.

The slope of the line in Figures 7.13 and 7.14 gives the observed order of accuracy and the slope of the line is nearly parallel to the 2^{nd} order slope. Table 7.4 shows that the order of accuracy obtained from Equation 2.24 is nearly 1.6 for both solid fractions at high and low face velocities which is reasonable.

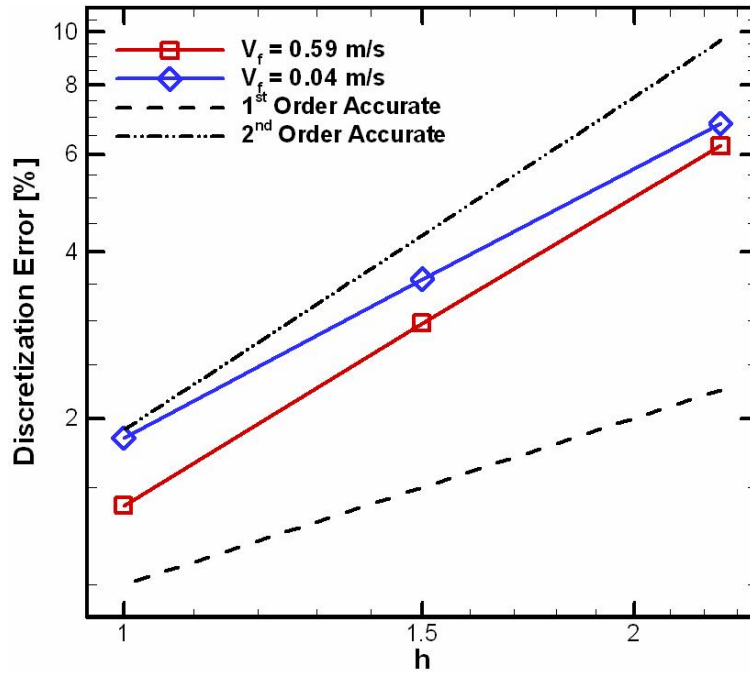


Figure 7.13: Discretization error in the pressure drop for microfibrinous materials ($\chi_p=59\%$)

Discretization error estimates in these numerical simulations are tabulated in Table 7.4 along with the details of the generated flow-field grids and pressure gradients. It is observed that the estimated discretization errors range from 1.2% (fine grid) to 6.8% (coarse grid) for the solid fraction of 59% and from 1.0% (fine grid) to 4.1% (coarse grid) for the solid fraction of 53%. This estimated discretization error provides guidance in choosing an appropriate grid. The medium grid is used for all simulations presented in this study which has maximum discretization error estimates of 3.5% for the cases examined.

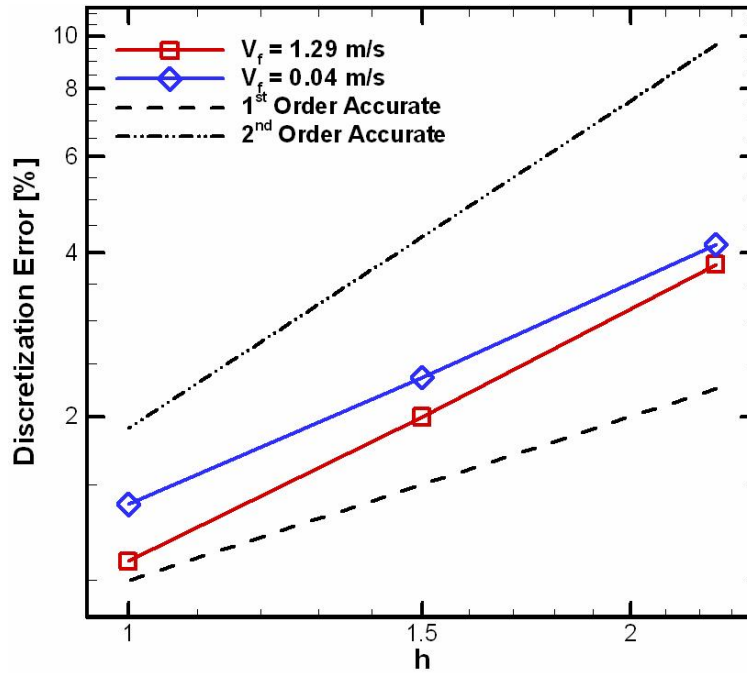
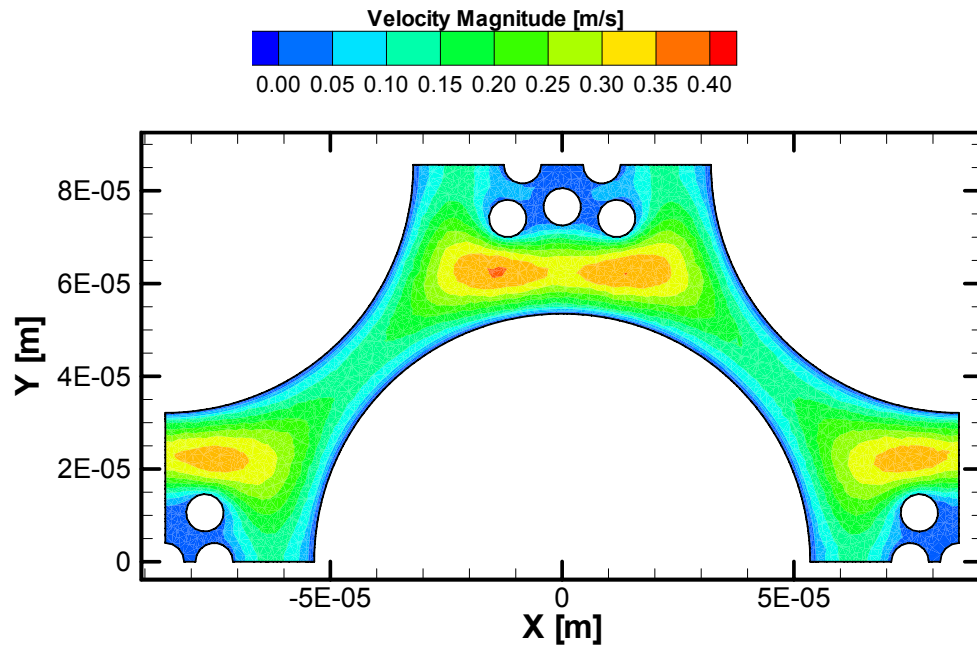


Figure 7.14: Discretization error in the pressure drop for microfibrus materials ($\chi_p=53\%$)

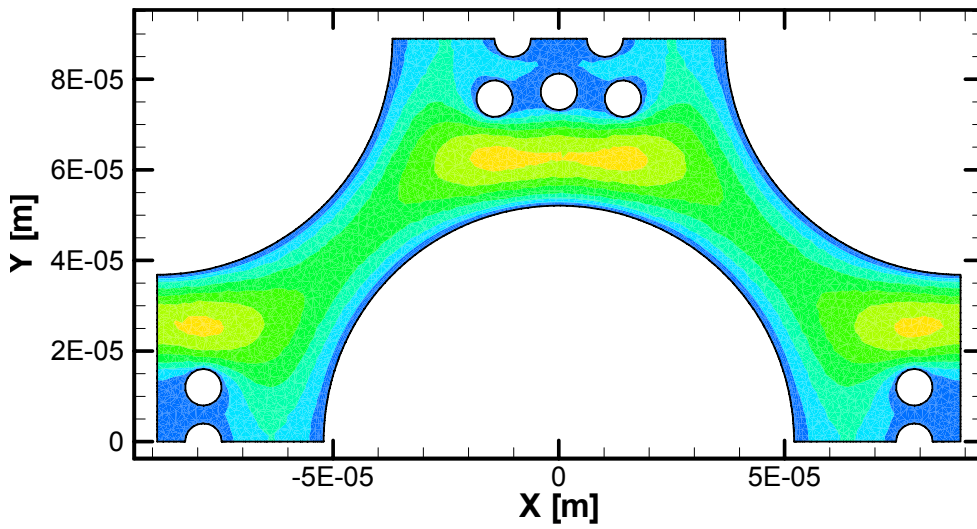
7.1.3.2 Results and Model Validation

CFD simulations were performed using the generated flow-field meshes in order to predict the pressure drop and analyze the details of the flow in microfibrus materials. A plane was extracted at the center of the domain (i.e., $Z = 2.48 \mu\text{m}$ for the case with a solid fraction of 59% and $Z = 2.445 \mu\text{m}$ for the case with a solid fraction of 53%). The velocity magnitude and pressure contours are shown in Figures 7.15 and 7.16 for air flowing at a face velocity of 0.04 m/s (the lowest velocity case).

Figure 7.15 shows that the flow speeds up between the fibers and the particles for both solid fractions. In addition, the flow slows down between the fibers due to the



(a) Solid Fraction = 59%



(b) Solid Fraction = 53%

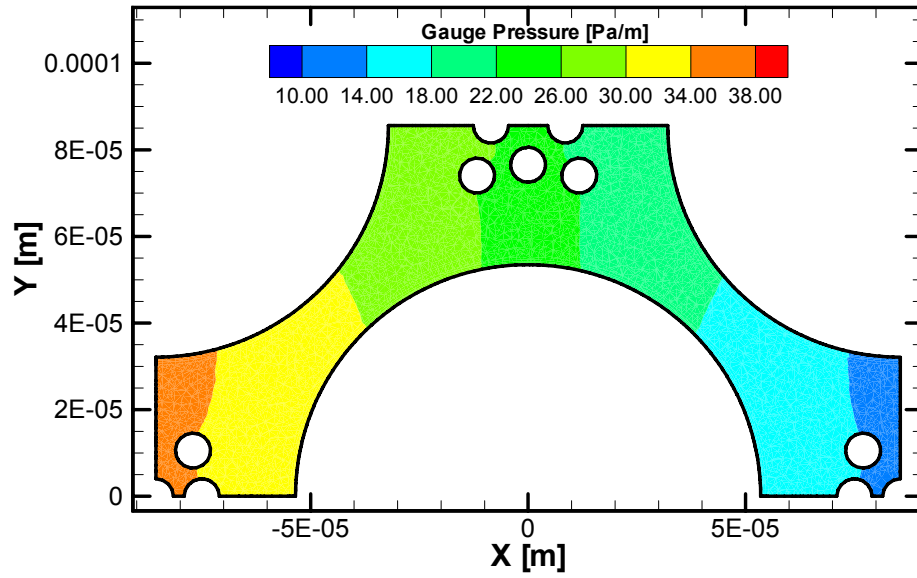
Figure 7.15: Velocity contours in constant Z -plane for microfibrous materials: $V_f = 0.04$ m/s

Table 7.4: Discretization error in predicting pressure drop for Microfibrous Materials

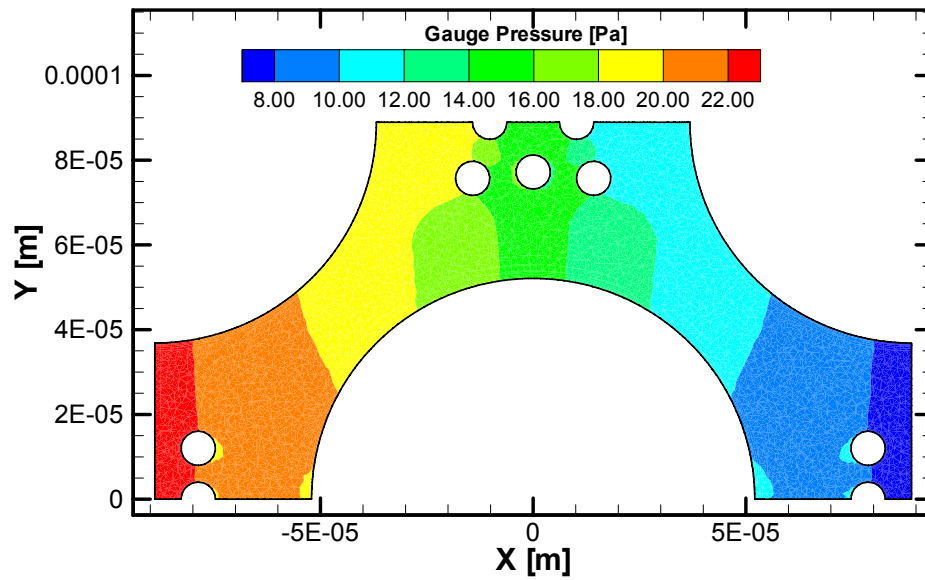
Face Velocity [m/s]	Grid Level	No. of Elements	Pressure Gradient [Pa/m]	Observed Order of Accuracy	Estimated Exact Solution	Discretization Error [%]
SOLID FRACTION = 59%						
0.04	Coarse	369,136	136,380.	1.63	146,365.8	6.8
	Medium	812,958	141,140.			3.5
	Fine	2,743,441	143,670.			1.8
0.59	Coarse	369,136	1,878,700.	1.63	2,003,163.	6.2
	Medium	812,958	1,943,600.			2.9
	Fine	2,743,441	1,978,100.			1.2
SOLID FRACTION = 53%						
0.04	Coarse	362,743	89,102.	1.60	92,949.9	4.1
	Medium	1,249,410	90,759.			2.3
	Fine	3,398,596	91,668.			1.3
0.04	Coarse	362,743	2,793,600.	1.82	2,904,112.	3.8
	Medium	1,249,410	2,846,100.			1.9
	Fine	3,398,596	2,872,600.			1.1

geometric modeling approximations which force the fibers to be closer to each other than seen in the actual microfibrous materials. The ratio of the peak velocity to the face velocity is approximately nine for the solid fraction of 59% and seven for the solid fraction of 53%. The flow is symmetric across $X = 0$ for both solid fractions at low face velocity, and although not shown here, it was observed that the flow deviates from symmetric behavior at high face velocity.

Figure 7.16 shows a gradual decrease in pressure across the length of the domain. The pressure drop across the length of the domain is small at low face velocity for both solid fractions, whereas the pressure drop was found to be large at high face velocity for both the solid fractions. A similar analysis was performed with the



(a) Solid Fraction = 59%



(b) Solid Fraction = 53%

Figure 7.16: Pressure contours in constant Z-plane for microfibrous materials: $V_f = 0.04$ m/s

planes extracted at constant Y locations (not shown here) and similar behavior was observed.

CFD predictions for the pressure drop per unit length of the bed for air flowing through microfibrrous materials are compared with the pressure drops from empirical correlations and those measured in the experiments [3] for both the solid fractions and at various face velocities. Some approximations are made while predicting the pressure drop using these empirical correlations. As discussed earlier in section 5.1, Ergun's equation is valid for the materials with one type of particle only. In order to use Ergun's equation to predict the pressure drop in a microfibrrous material, an equivalent diameter is calculated using Equation 5.22 with shape factors of 0.72, 1.5, and 1.5 for ACP, Ni, and PC, respectively [3]. The shape factors used in Ergun's equation to determine the equivalent diameter are also used in the PMP equation. A flow angle of $\theta = 20$ degrees, obtained by calibrating with the experimental data, is used for the PMP equation. The tortuosity (τ) is estimated using $\tau = \frac{1}{2}(1 - \epsilon)$ which is obtained by considering a cubic unit cell with one spherical particle [3].

The pressure drops found from the CFD simulations, the PMP equation, and Ergun's equation are plotted against the face velocity on a log-log plot for both solid fractions along with the experimentally measured pressure drop and are shown in Figure 7.17.

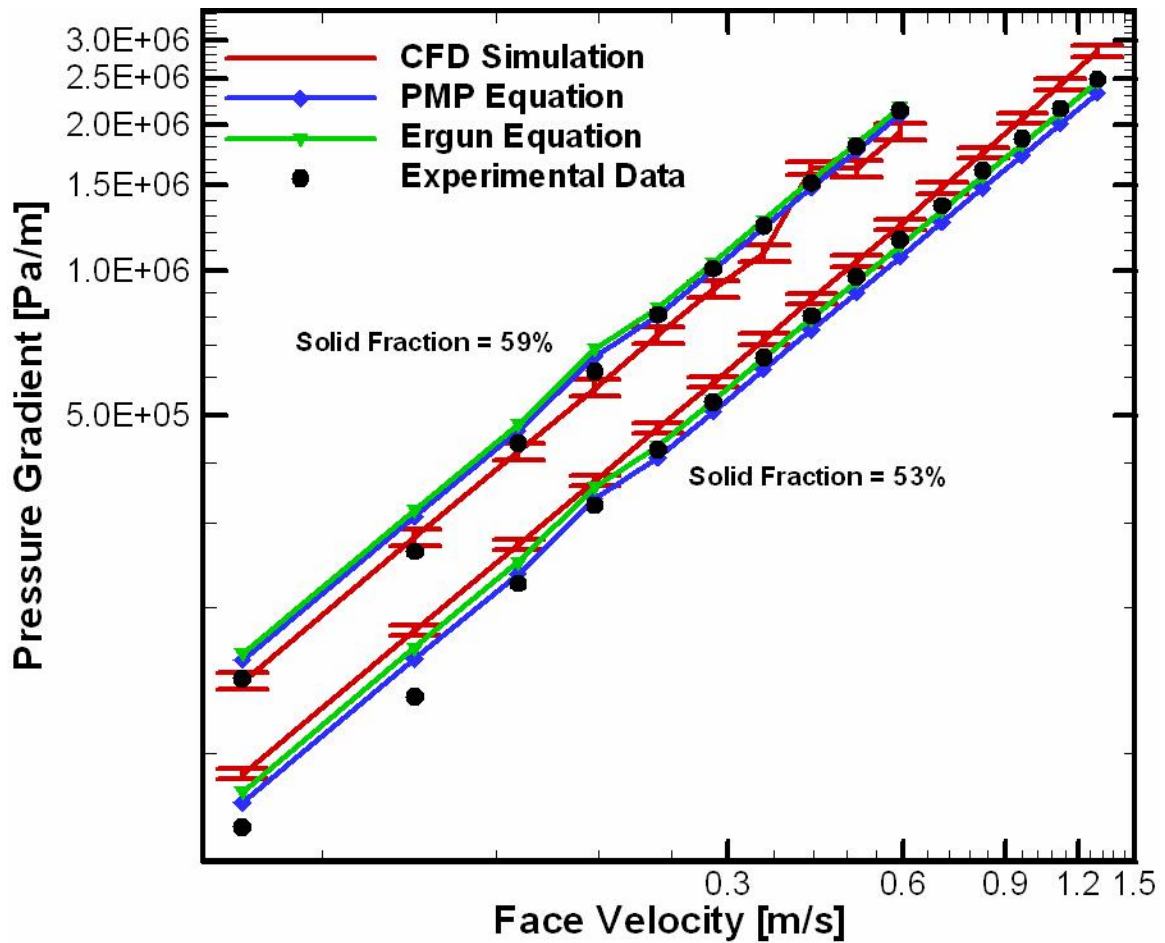


Figure 7.17: Comparison of pressure drop from simulations to empirical correlations and experimental data for microfibrous materials [3]; Numerical uncertainty = 2-4%

As discussed above, a shape factor of 0.72 is used for ACP while determining the pressure drop using the PMP and Ergun's equation, whereas in the CFD simulations smooth spheres (i.e., a shape factor of one) are used. Figure 7.17 shows good agreement between CFD simulations and empirical correlation in predicting the pressure drop for both the void fractions. The pressure drop obtained from the CFD

simulations is 8-20% lower than the empirical correlations for lower solid fraction (53%) and 8-12% higher for high solid (59%). Figure 7.17 also shows that the CFD predictions of pressure drop are in reasonably good agreement with the experimental measurements. The numerical uncertainty (error bars) used in Figure 7.17 is calculated using Richardson extrapolation (Equation 7.2). For a solid fraction of 59%, CFD simulations under-predicted the pressures drop at all face velocities compared to the experimental measurements, whereas for a solid fraction of 53%, the CFD simulations over-predicted the pressure drop at all face velocities compared to the experimental measurements.

The error in predicting the pressure drop for the CFD simulations and the empirical correlations relative to experimental measurements is calculated using Equation 7.6:

$$\% \text{ Error in } \frac{\Delta P}{L} = 100 \times \frac{\left(\frac{\Delta P}{L}\right)_{CFD/empirical} - \left(\frac{\Delta P}{L}\right)_{experimental}}{\left(\frac{\Delta P}{L}\right)_{experimental}} \quad (7.6)$$

The calculated errors in pressure drop predictions using CFD and the empirical correlations are plotted against the face velocity for both the solid fractions (53% and 59%) and are shown in Figures 7.18 and 7.19, respectively. For a solid fraction of 59% the CFD simulations are within 10% of the experimental measurements whereas for a solid fraction of 53% the CFD simulations are within 10-30% of the experimental

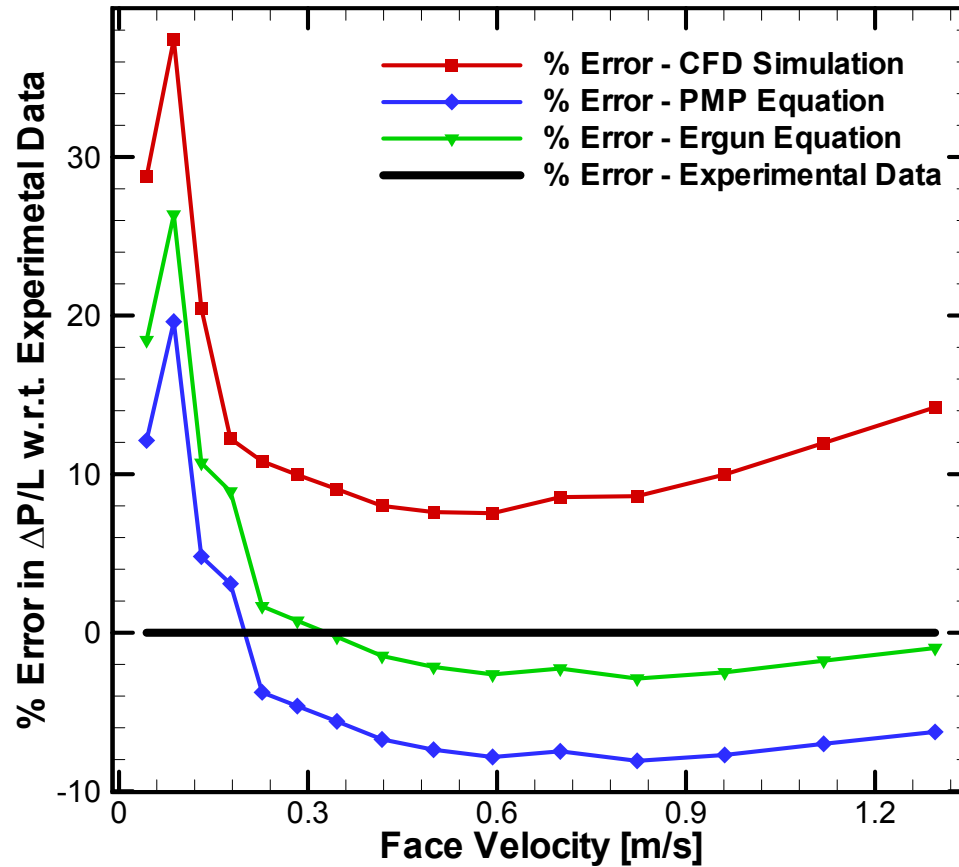


Figure 7.18: Error in predicting pressure drop in microfibrrous materials with respect to experiments [3]: $X_p=53\%$

measurements. The deviation of pressure drop obtained using the CFD simulations and empirical correlations relative to experiments have the same trend for both the solid fractions are shown in Figures 7.18 and 7.19. This consistent trend suggests that either there are physical mechanisms missing from both the simulations and the theory-based correlations, or that there are experimental bias errors which correlate with face velocity.

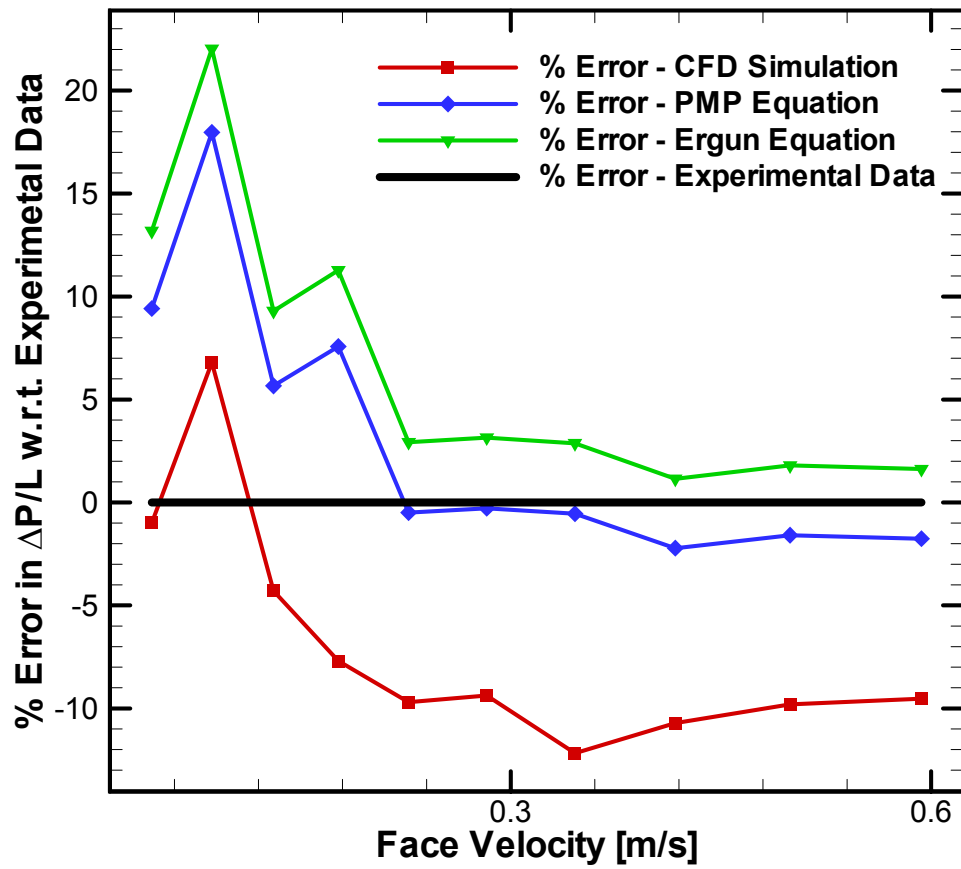


Figure 7.19: Error in predicting pressure drop in microfibrus materials with respect to experiments [3]: $X_p=59\%$

7.2 Dimensionless Analysis

In order to minimize the size of the parametric study, a dimensionless analysis is performed. In this study, the dimensionless numbers used are Reynolds number (refer Section 2.3.1), Peclet number (refer Section 2.3.2), and Damkohler number (refer Section 2.3.3). Various physical quantities that influence chemical conversion and pressure gradient in flows through microfibrous materials which can be varied using these three dimensionless numbers are: diameter of the particle d_p , interstitial velocity V_i , kinematic viscosity ν , mass diffusivity D_{AB} , and reaction rate (keeping the activation energy constant) k_{fr} . Interstitial velocity, diameter of the particle, and pre-exponential factor are varied by maintaining the dimensionless numbers constant. Kinematic viscosity and mass diffusivity were back calculated using the definitions of the dimensionless numbers.

The effect of interstitial velocity, diameter of the particle, and pre-exponential factor on log reduction and dimensionless pressure gradient is studied in this section. The dimensionless pressure gradient is defined using Equation 7.7.

$$\text{Dimensionless Pressure Gradient} = \left(\frac{\Delta P}{\frac{1}{2}\rho V_i^2} \right) \left(\frac{d_p}{L} \right) \quad (7.7)$$

Reynolds, Peclet, and Damkohler numbers were chosen equivalent for desulfurization on catalytic particles at high face velocity (~ 0.104 m/s, from experimental

data; refer Section 4) with an operating temperature of 400 °C. The particle diameter d_p is varied between 100 and 200 μm , the interstitial velocity is varied from 1 $\mu\text{m/s}$ to 100 m/s, and the reaction rate is varied by varying the pre-exponential factor (as activation energy is kept constant) between 1.7×10^{-4} and 1.7×10^4 m/s.

A three dimensional contour plot is made with diameter of the particle, log of interstitial velocity, and log of reaction rate on linear axes of X, Y, and Z, respectively, to show the how log reduction and dimensionless pressure gradient varies with d_p , V_i , and k_{fr} when the dimensionless numbers are held constant in Figures 7.20 and 7.21, respectively.

Figure 7.20 shows the variation in log reduction when the selected parameters are varied. It is observed that for all the runs, the log reduction only varied between 1.967 and 1.969, which is less than 0.1% variation. It can thus be concluded that these are the appropriate dimensionless parameters affecting the chemical reactivity.

Figure 7.20 shows the variation in dimensionless pressure gradient when the selected parameters are varied. It is observed that for all the runs, the dimensionless pressure gradient varied between 21824.4 and 22047.2 which is approximately 1.0% variation.

From this dimensionless parameter study, it can be confirmed that there is no effect of the physical quantities on log reduction and dimensionless pressure gradient when the three dimensionless numbers are maintained constant.

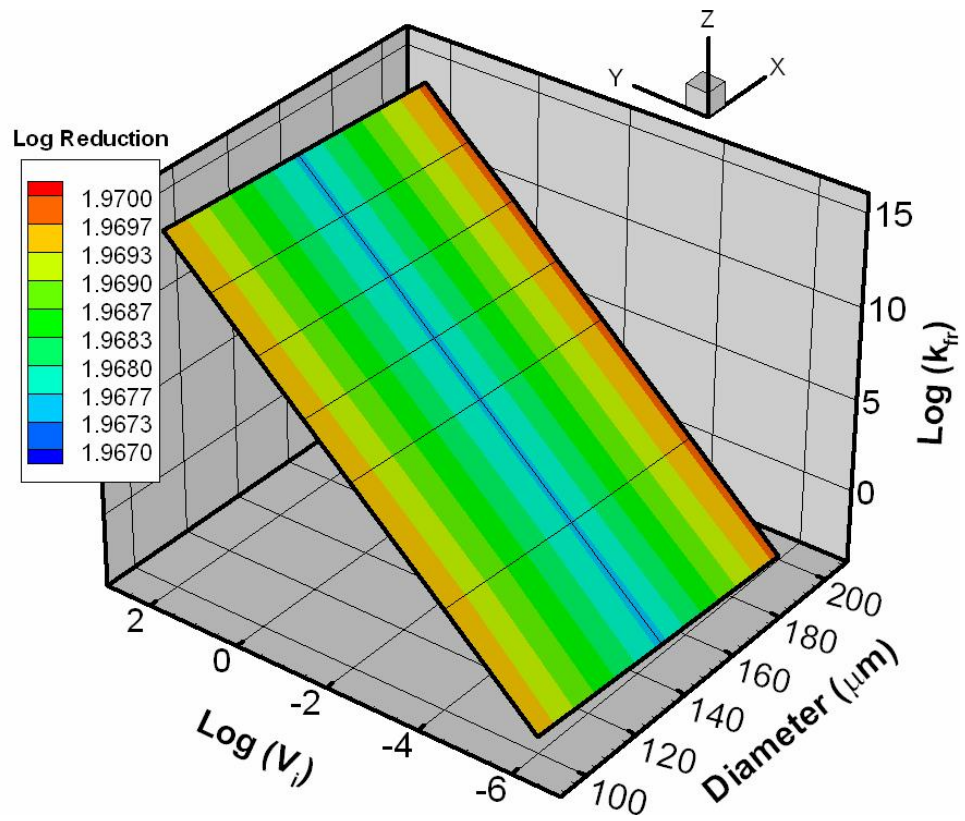


Figure 7.20: Dimensionless analysis: log reduction

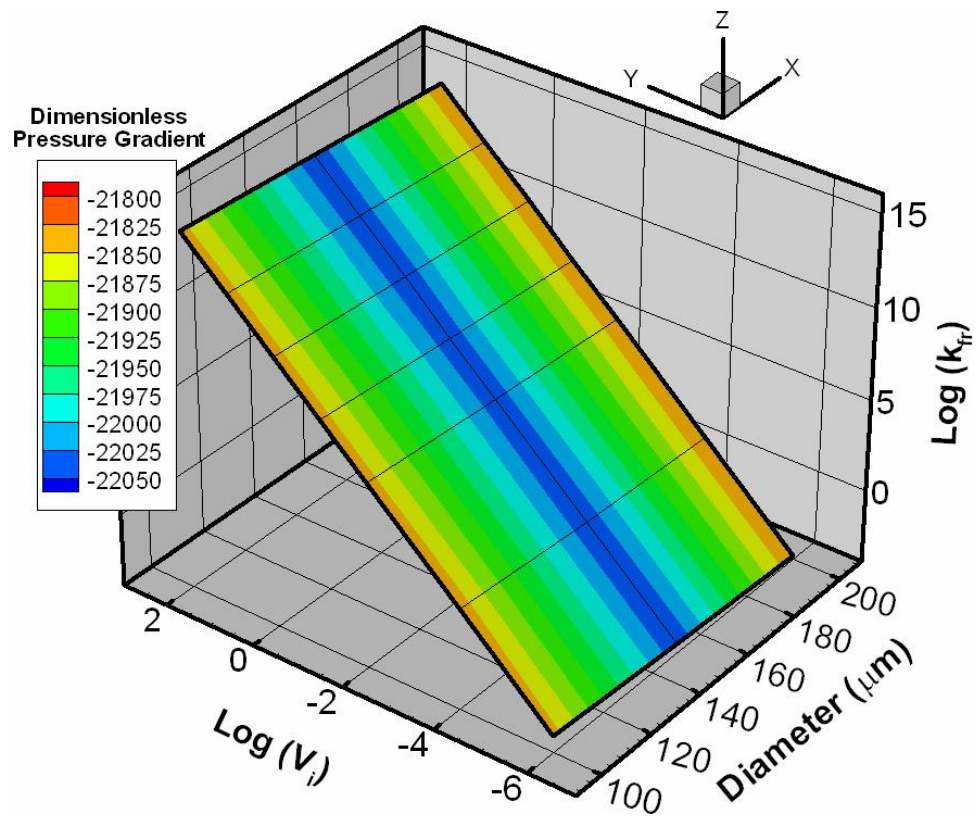


Figure 7.21: Dimensionless analysis: dimensionless pressure gradient

The range of Reynolds and Schmidt numbers are calculated for various gas phase and liquid phase applications: desulfurization, removal of trace amounts of hexane, CO oxidation, and removal of Benzothiophene from JP5 jet fuel.

Figure 7.22 shows the detailed range of Reynolds and Schmidt numbers for these applications. Typical Schmidt numbers for gas flows range between 0.5 and 5, whereas for liquid flows, they range between 700 and 1000. In this study, the focus is on desulfurization ($Sc=1.3$) and hexane removal ($Sc=2.0$). Thus, the Reynolds number is varied between 0.001 and 0.1 in the desulfurization study and between 0.01 and 1.0 in the hexane removal study.

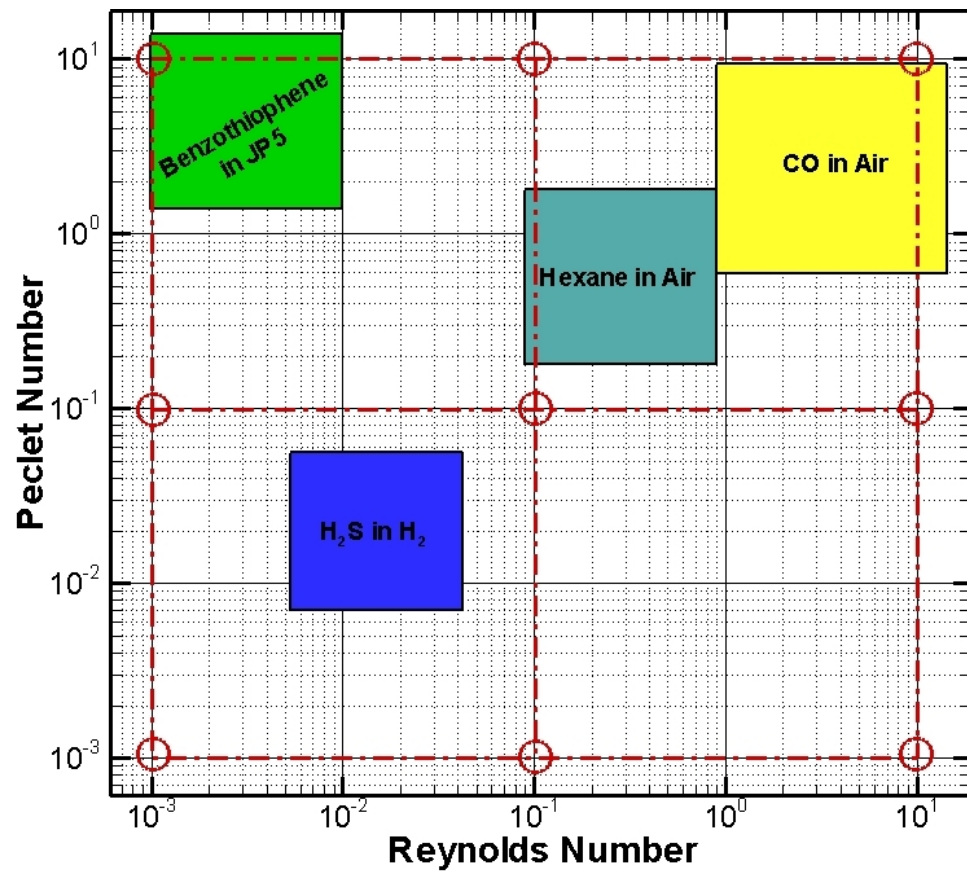


Figure 7.22: Flow properties for various gas and liquid phase applications

7.3 Chemically Reacting Gas Flows

CFD geometric model of packed beds, different microfibrinous materials have been developed using GAMBIT as discussed in the Section 6.1.2. Four unit cells were used to capture the chemical over the reasonable length of the domain. Tests were performed by varying number of unit cells and observed that the chemical conversion is varying linear with length of the domain. In order to minimize the end effects, inert cells were placed at the entrance and exit of the reacting zone which turns out to be six unit cells in the CFD geometric model used for this study.

Symmetry boundary conditions have been used on the surfaces parallel to the flow direction. By applying symmetry, only one quarter of the total domain shown in Figure 6.1 is modeled and thus computational time is reduced. The fluid inlet has been defined as a velocity inlet where we define the velocity and concentration of the challenge gas. Also inlet is defined as diffusion inlet. As we are using segregated solver in FLUENT, a commercial CFD code, the net transport species at inlet is due to convection and diffusion. The convection transport is fixed by the inlet species concentration (defined as inlet concentration) and diffusion is obtained from the gradient of computed species at the inlet [53].

7.3.1 Desulfurization

Desulfurization reaction has been modeled as it has many industrial applications (as discussed in Section 2.2.3). In this section we will discuss how the chemical reaction rate has been calibrated. We will discuss the results obtained for CFD validation comparison with experiments as well as various numerical experiments performed to study the effects of clustering and dilution on chemical conversion during desulfurization process in packed beds and microfibrous materials.

In this study, the surfaces of the particles are defined as catalytically reacting walls. The effectiveness factor was calculated and is found to be 0.9995. Thus, we can treat the particle as if all the ZnO were on the surface of the particle. The site density of ZnO on the surface of the particles is assumed to be 1 which means that the ZnO is a non-consumable sorbent. Using the Weisz-Prater criteria [57], the modulus was calculated and found to be $3.24\text{E-}4$ ($\ll 1$) which tells us that intra particle diffusion occurs rapidly and can be neglected. For the case of microfibrous materials, fiber surfaces are defined as inert walls. The temperature on the walls (both reacting and inert walls) is defined as $400\text{ }^{\circ}\text{C}$ to be consistent with experiments.

Operating conditions and fluid properties used in this study are tabulated in Table 7.5.

Table 7.5: Operating conditions and fluid properties for desulfurization study

Reaction	Inlet Conc.	Temperature (°C)	Operating Pressure (Pa)	Diffusivity	Viscosity
$H_2S + ZnO \longrightarrow$ $H_2O + ZnS$	20,000 ppmv	400	10312	2.8 cm ² /s	1.7×10 ⁻⁵ kg/m-s

7.3.1.1 Calibration of Reaction Rate for Simulations

The reaction rate has been calibrated for the simulations using experimental data of packed beds at high face velocity (≈ 0.104 m/s). A first order catalytic reaction was assumed and the reaction rate has been calculated using the Arrhenius equation (Equation 2.23).

An activation energy (E_a) of 30,313 KJ/Kg mol (≈ 7240 cal/mol) is used for desulfurization reaction between H₂S and ZnO at an operating temperature of 400 °C [85]. A trial and error method is used to calibrate the unknown pre-exponential factor (A_r) in the rate equation. Table 7.6 shows various trials performed to match experimentally measured log reduction in a 16 mm thick packed bed when the challenge gas is flowing at a face velocity of 0.104 m/s. It is observed that when the pre-exponential is approximately 17 s⁻¹, the log reduction obtained from the simulations matched with the experimentally measured value. For the remainder of the simulations that will be discussed in this paper a calibrated pre-exponential factor of 17 s⁻¹ was employed.

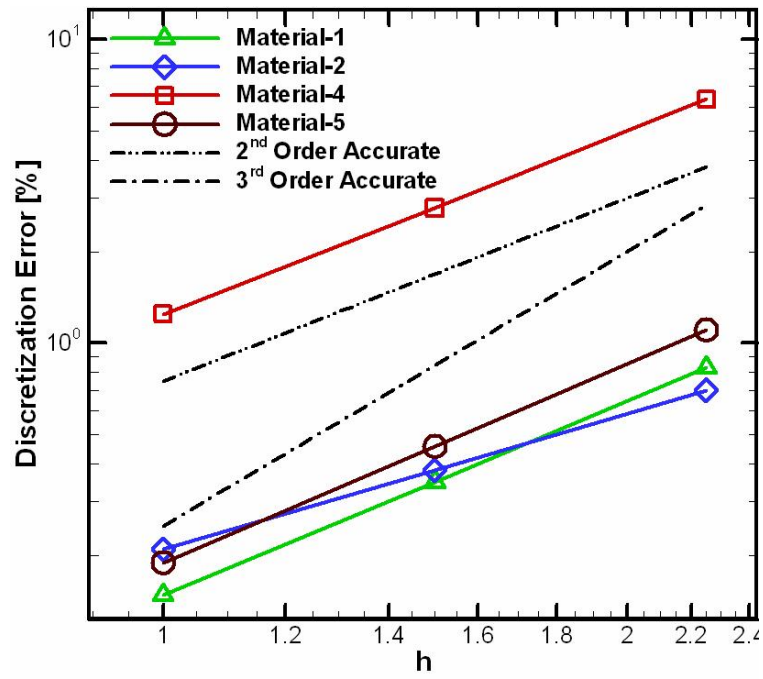
Table 7.6: Calibration of Pre-Exponential Factor

Pre-Exponential Factor (1/s)	Log Reduction $\left[\log \left(\frac{C_{inlet}}{C_{outlet}} \right) \right]$
32	36.49
18	25.09
13	15.94
16	18.75
17	19.65

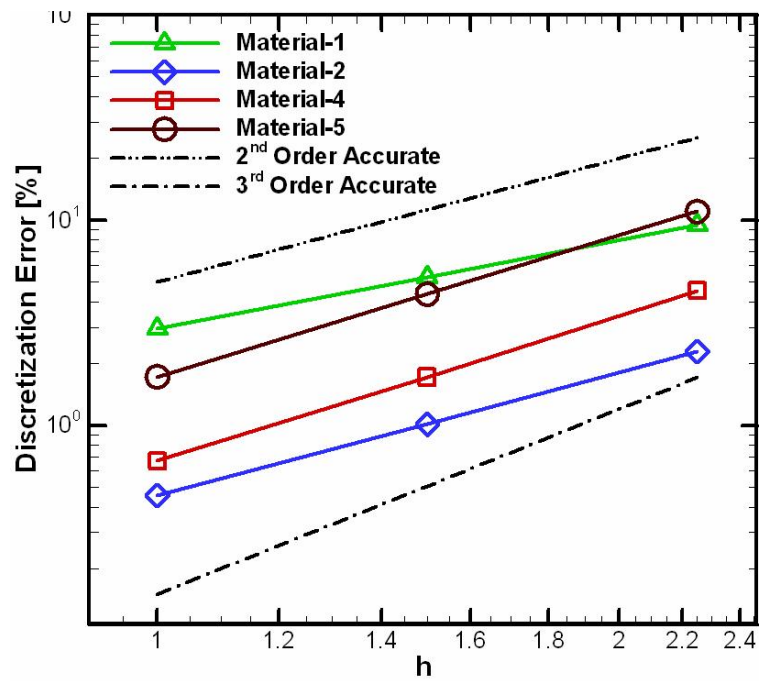
7.3.1.2 Numerical Accuracy

Three flow-field grids were generated by uniformly refining each cell in the domain by a factor of 1.5 in all three directions (X, Y, and Z). The exact solution for the log reduction and pressure drop per unit length is estimated from generalized Richardson extrapolation [84] using Equation 7.2. The relative discretization error in log reduction and pressure gradient for different materials (materials 1, 2, 4 and 5) were plotted against the grid refinement parameter h to estimate the order of accuracy and is shown in Figures 7.23(a) and 7.23(b), respectively.

The slope of the lines in Figures 7.23(a) and 7.23(b) gives the observed order of accuracy. While predicting log reduction in microfibrous materials, the slope of the lines shown in Figure 7.23(a) is between 1.75 and 2.5; while predicting pressure drop



(a)



(b)

Figure 7.23: Discretization error for different microfibrus materials: (a) log reduction; (b) pressure drop

in microfibrinous materials, the slope of the lines shown in Figure 7.23(b) is between 1.6 and 2.8. Table 7.7 shows the order of accuracy obtained (using Equation 2.24) while predicting log reduction and pressure drop in microfibrinous materials.

Discretization error estimates in these numerical simulations are tabulated in Table 7.7 along with the details of the log reduction and pressure gradients. It is observed that the estimated discretization errors range from 0.14-0.20% (fine grid) to 0.7-1.1% (coarse grid) in predicting log reduction and from 0.4-2.0% (fine grid) to 2.0-11.1% (coarse grid) in predicting pressure gradient. This estimated discretization error provides guidance in choosing an appropriate grid. The medium grid is used for all simulations presented in this study which has maximum discretization error estimates of 2.7% and 5.2% while predicting log reduction and pressure gradient, respectively. Numerical uncertainty is shown in all the simulation results discussed in this section by plotting error bars using these error estimates.

7.3.1.3 Effect of Residence Time

The log reduction in H₂S for packed beds (60% solid volume loading) and microfibrinous materials (25% solid volume loading) obtained from the simulations is compared to the experimentally obtained log reduction (discussed in Section 4.2) and is shown in Figure 7.24. Figure 7.24 shows the comparison of log reduction in packed bed and microfibrinous material between the simulation and the experimental data.

Table 7.7: Discretization error in log reduction and pressure gradient for different microfibrinous materials for desulfurization

	Grid Level	Solution	Order of Accuracy	Estimated Exact Solution	Estimated Discretization Error [%]
MATERIAL-1: $d_p = 150 \mu\text{m}$; $d_f = 8 \mu\text{m}$; $\chi_p = 20 \text{ vol.}\%$; $\chi_f = 3.0 \text{ vol.}\%$					
Log Reduction	Fine	1.642	2.39	1.644	0.148
	Medium	1.638			0.348
	Coarse	1.630			0.8293
Pressure Gradient	Fine	41,857.	1.62	43,130	2.95
	Medium	40,858.			5.26
	Coarse	39,052			9.45
MATERIAL-2: $d_p = 150 \mu\text{m}$; $d_f = 4 \mu\text{m}$; $\chi_p = 20 \text{ vol.}\%$; $\chi_f = 3.0 \text{ vol.}\%$					
Log Reduction	Fine	1.626	1.74	1.629	0.2088
	Medium	1.623			0.380
	Coarse	1.618			0.699
Pressure Gradient	Fine	27,081.	2.33	27,204	0.4537
	Medium	26,929			1.011
	Coarse	26,582			2.285
MATERIAL-4: $d_p = 150 \mu\text{m}$; $d_f = 4 \mu\text{m}$; $\chi_p = 20 \text{ vol.}\%$; $\chi_f = 1.5 \text{ vol.}\%$					
Log Reduction	Fine	1.824	2.29	1.801	1.246
	Medium	1.851			2.783
	Coarse	1.916			6.358
Pressure Gradient	Fine	290,532.	2.68	292,490.	0.669
	Medium	287,468.			1.717
	Coarse	279,232.			4.5329
MATERIAL-5: $d_p = 150 \mu\text{m}$; $d_f = 4 \mu\text{m}$; $\chi_p = 20 \text{ vol.}\%$; $\chi_f = 4.5 \text{ vol.}\%$					
Log Reduction	Fine	1.867	2.52	1.863	0.188
	Medium	1.8725			0.4571
	Coarse	1.884			1.106
Pressure Gradient	Fine	137,975.	2.64	140,396	1.72
	Medium	134,275			4.360
	Coarse	124,922			11.022

It is observed that the log reduction predicted by simulations is in good agreement with experimental results (within 2%). Due to experimental limitations, the data for microfibrinous material at different velocity are not available. So, comparison to the log reduction in microfibrinous material with simulations is done only at the low face velocity.

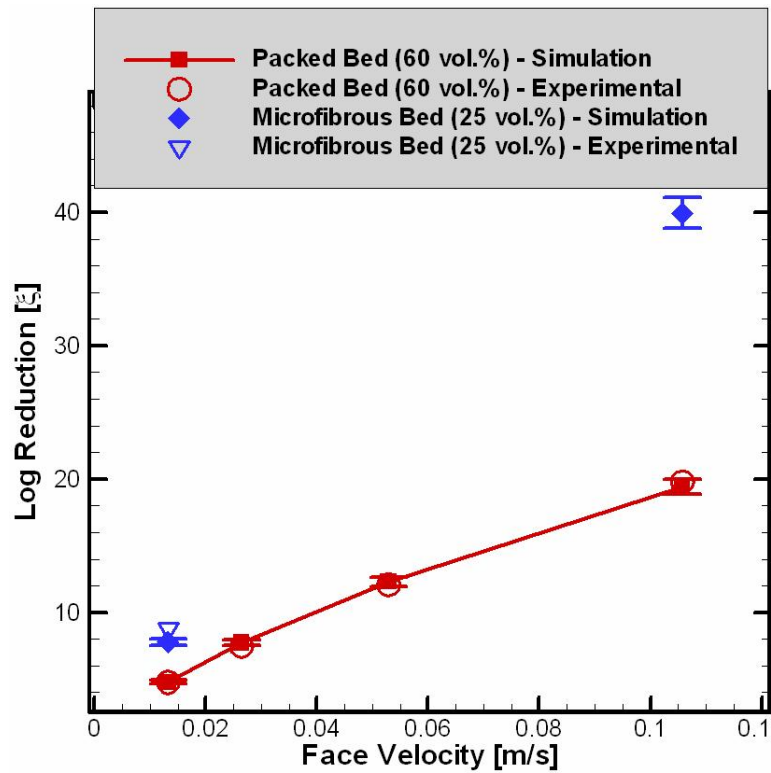


Figure 7.24: Effect of residence time: (a) packed bed with 60 vol.% loading and microfibrinous material with 25 vol. % loading

Velocity contours in a constant X-plane and contours of H_2S concentration in a constant Y-plane for the case with low face velocity (1.3 cm/s and 2 mm bed thickness) are shown in Figure 7.25. We observe that the velocity increases when

the particles are close together and the concentration of H_2S decreases as the gas reaches the end of the bed which confirms that H_2S is being decomposed into H_2 and S. Sulfur is reacting with ZnO to form ZnS which remains on the surface of the particles. In this case, the fluid is entering the bed at a interstitial velocity (ratio of face velocity to void fraction) is 0.0325 m/s and when the particles are close to each other, the velocity increased and the peaking velocity is equal to four times the interstitial velocity and ten times the face velocity (0.013 m/s).

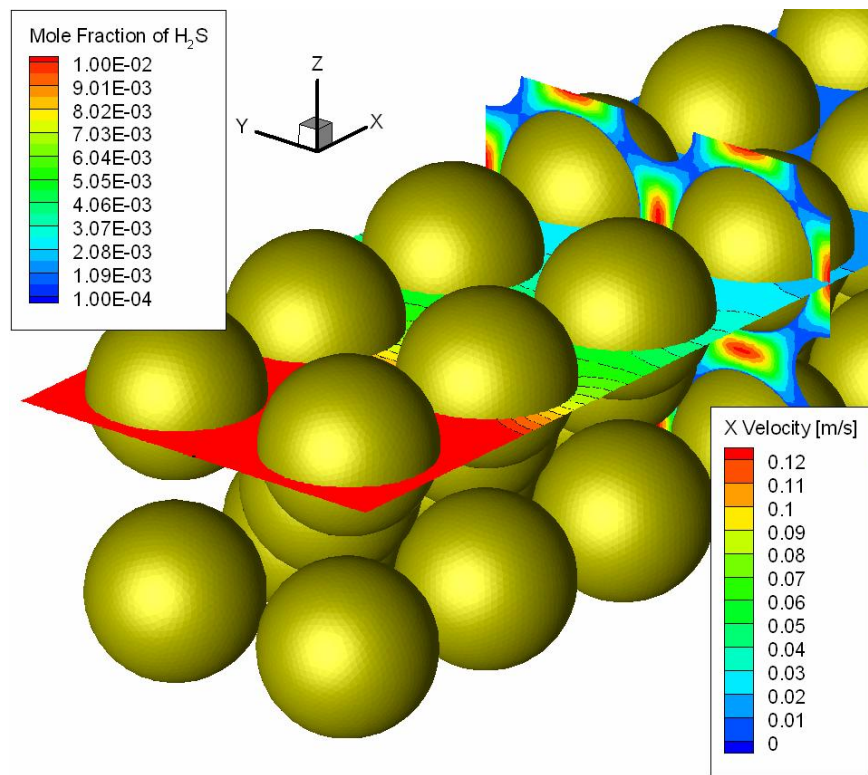


Figure 7.25: Contours of velocity and concentration in packed beds at low velocity (1.3 cm/s)

7.3.1.4 Effect of Dilution with Void

The effect of dilution on the log reduction is studied by diluting packed beds with void. The original packed beds with 60% solid volume loading were diluted with 20% and 40% void resulting in frozen beds with 40% and 20% solid volume loading. Figures 7.26(a) and 7.26(b) show the 3D geometric model of the packed bed (60% solid volume loading) and a frozen bed (5% solid volume loading) respectively. Though the frozen bed with 5% solid volume loading is not used in this study, it is shown just to get an idea how far the particles can be separated in microfibrus materials.

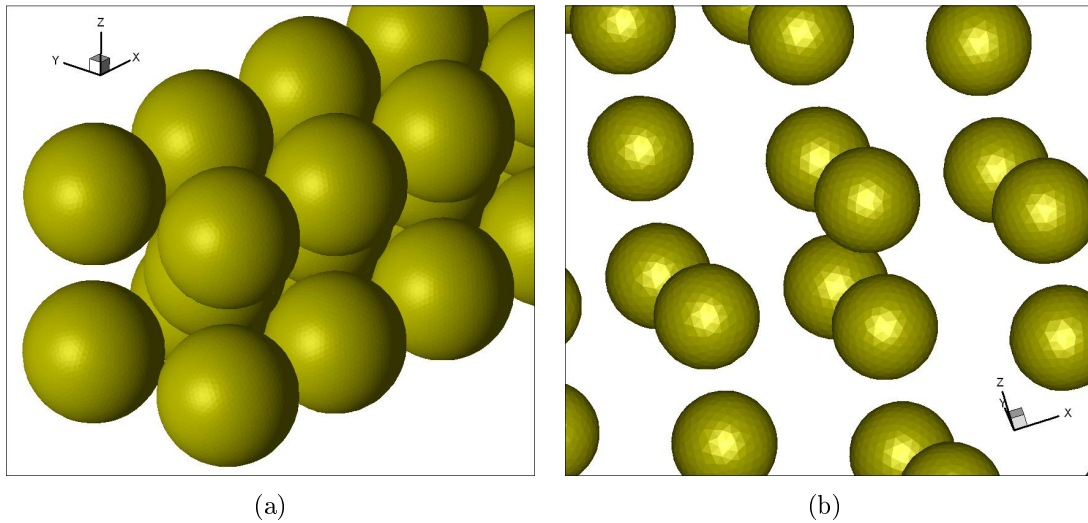


Figure 7.26: 3D Geometric Model: (a) packed bed with 60 vol.% loading and (b) diluted bed with 5 vol. % loading

These kind of frozen beds does not exist in reality, but this is an useful exercise to isolate the effects and get better understanding of the phenomena behind enhanced reactivity in microfibrrous materials.

We can estimate the effect of voidage on the log-reduction in concentration in packed beds using the film mass transfer coefficient determined by the Chilton-Colburn factor (j_D). The empirical correlation of Dwivedi et al. [86] is given by:

$$k_f = j_D Re Sc^{\frac{1}{3}} \frac{\mathcal{D}_{AB}}{d_{eq}} \quad (7.8)$$

where for gas phase mass transfer in fluidized beds ϵj_D can be written as

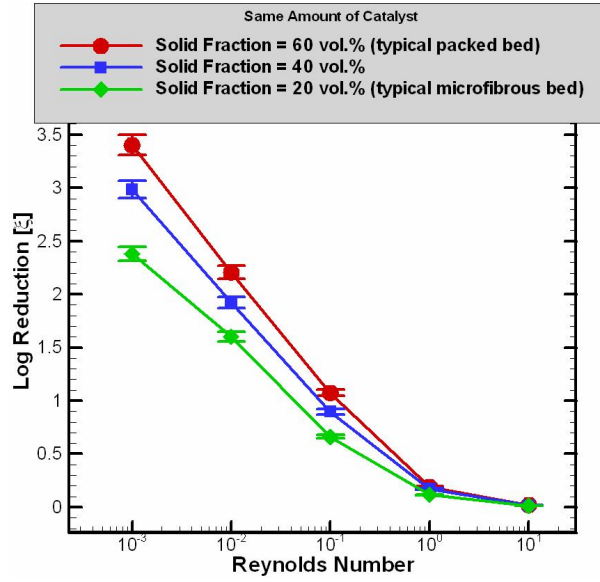
$$\epsilon_b j_D = 0.4548 Re^{-0.4069} \quad (7.9)$$

k_f can be calculated from the log reduction of the concentration as:

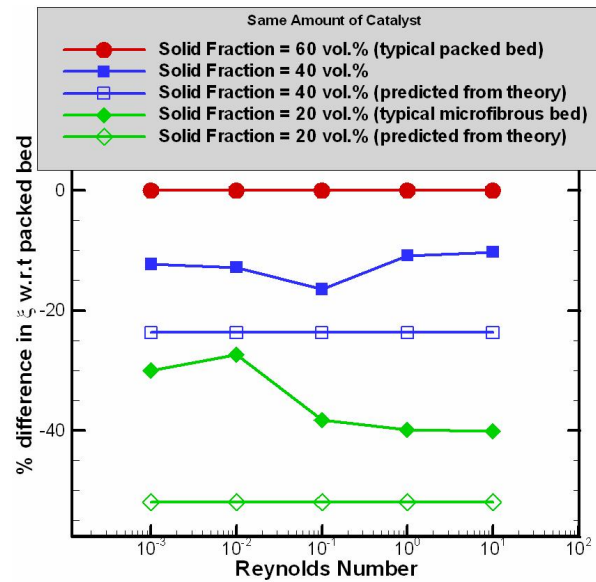
$$k_f = \frac{V_f}{L(1-\epsilon)a_v} \log \left(\frac{C_i}{C_o} \right) \quad (7.10)$$

Using Equations 7.8 - 7.10, the log reduction can be written as a function of the void fraction as shown below:

$$\log \left(\frac{C_i}{C_o} \right) = -0.4548 \frac{L}{V_f} \frac{(1-\epsilon)}{\epsilon} a_v Re^{0.5931} Sc^{\frac{1}{3}} \frac{\mathcal{D}_{AB}}{d_{eq}} \quad (7.11)$$



(a)



(b)

Figure 7.27: Effect of dilution for desulfurization: (a) variation of log reduction with Reynolds number and (b) percentage difference in log reduction with respect to packed bed at 60 vol.% loading

If the bed is diluted, then the length must be increased for the same amount of catalyst. This indicates that the product of length of the bed and the solid volume fraction remains constant i.e., $(1 - \epsilon_1) L_1 = (1 - \epsilon_2) L_2$. Now consider two cases with different voidages and from Equation 7.11,

$$\log \left(\frac{C_i}{C_o} \right) \propto L \frac{(1 - \epsilon)}{\epsilon}$$

or rearranging:

$$\frac{\log \left(\frac{C_i}{C_2} \right)}{\log \left(\frac{C_i}{C_1} \right)} = \frac{L_2}{L_1} \frac{(1 - \epsilon_2)}{\epsilon_2} \frac{\epsilon_1}{(1 - \epsilon_1)} = \frac{\epsilon_1}{\epsilon_2} \quad (7.12)$$

From Equation 7.12, when a packed bed (60% solid volume, 40% void volume) is diluted by 20% and 40% void, the log reduction in concentration decreases by 33% and 50% respectively. In simulations we predicted the same trend of decrease in log reduction by diluting the packed bed with void as we see from classical chemical engineering (Equation 7.12).

The log reduction obtained from simulations is plotted versus Reynolds number for different voidages and is shown in Figure 7.27(a). It is observed that as the packed bed is diluted with void, the log reduction decreases. Figure 7.27(b) shows the percentage difference in log reduction for diluted beds with respect to the packed bed. We observe that the log reduction decreases 12-15% when the packed bed is diluted

with 20% void ($\approx 40\%$ solid volume loading), where as it decreases 30-40% when the packed bed is diluted with 40% void ($\approx 20\%$ solid volume loading). Figure 7.27(b) also shows the difference in log reduction (from theory predictions) of diluted beds with respect to packed bed.

7.3.1.5 Effect of Clustering

A particle clustering parameter (P_c) is defined using three length scales which varies from zero to one and CFD is used to predict the log reduction to study the effect of clustering. The three different length scales that were used to define clustering parameter are length of the bed, length of the cluster, and minimum length The length

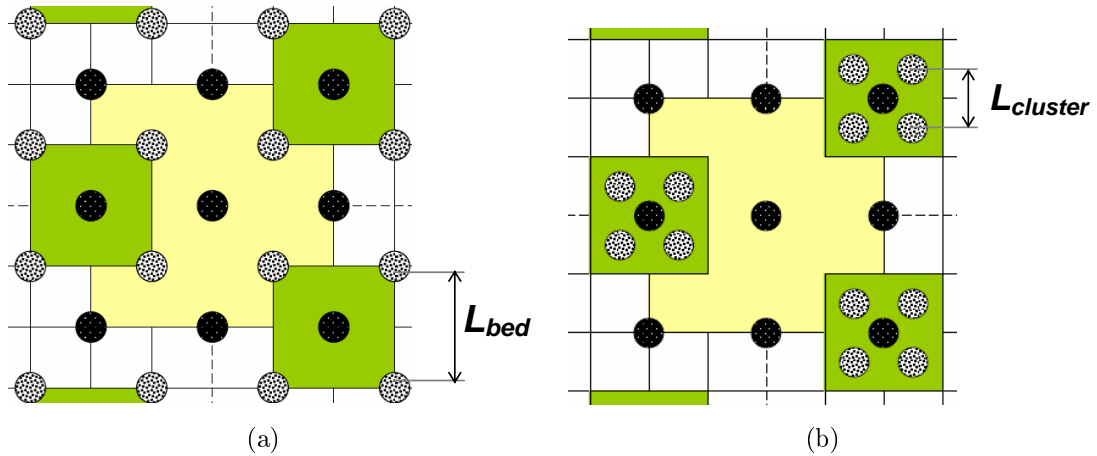


Figure 7.28: Clustering parameter: (a) uniform bed and (b) clustered bed

of the bed and the length of the cluster are graphically represented in Figure 7.28. Minimum length, L_{min} , is the length of domain when the particles touch each other.

In 2D, L_{min} is $\sqrt{2}d_p$ and for 3D, L_{min} is $\frac{2}{\sqrt{3}}d_p$. The clustering parameter is defined as the ratio of the difference between domain length of the bed and domain length of the cluster to the difference between domain length of the bed and minimum domain length of the cluster. Equation 7.13 is used to calculate the clustering parameter in this study:

$$P_c = \frac{L_{bed} - L_{cluster}}{L_{bed} - L_{min}} \quad (7.13)$$

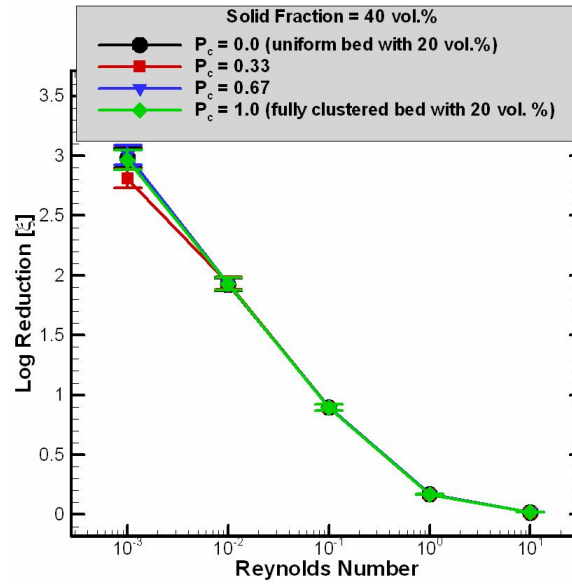
when $L_{bed} = L_{cluster}$, then the bed is uniform and we have $P_c = 0$

when $L_{cluster} = L_{min}$, then the particles are fully clustered (i.e., they are touching)

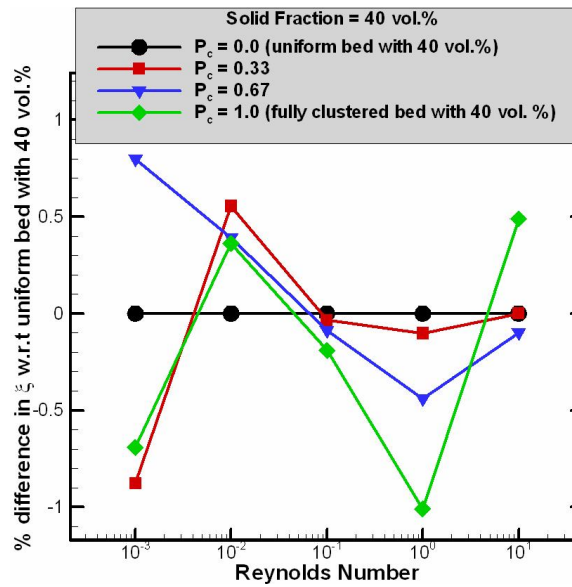
and we have $P_c = 1$

The effect of clustering on the log reduction is studied using two solid volume loading: 20% and 40%. Figures 7.29 and 7.30 shows the effect of clustering for frozen beds with solid volume loading of 40% and 20% respectively.

Figures 7.29(a) and 7.30(a) plotted with Reynolds number on X-axis (log scale) and log reduction on Y-axis (linear scale) show that clustering has no effect on the log reduction for both frozen beds. This can be explained because the diffusivity of the challenge gas (H_2S) is high. Figures 7.29(b) and 7.30(b) show the percentage difference in log reduction with respect to uniform bed whose clustering parameter is zero. It is observed that the percent difference is within 2% except for a single

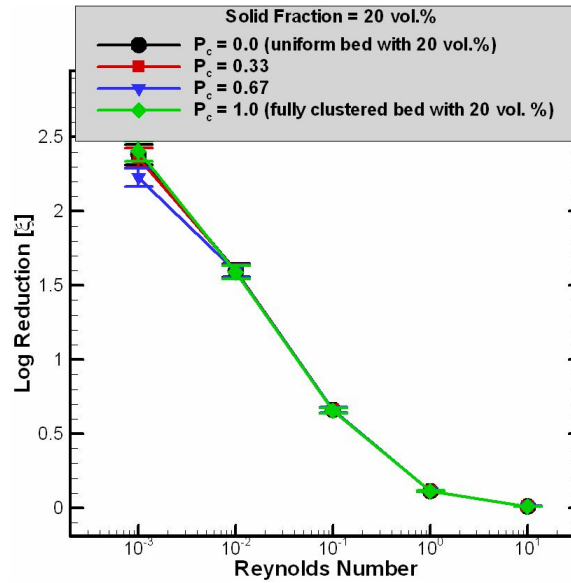


(a)

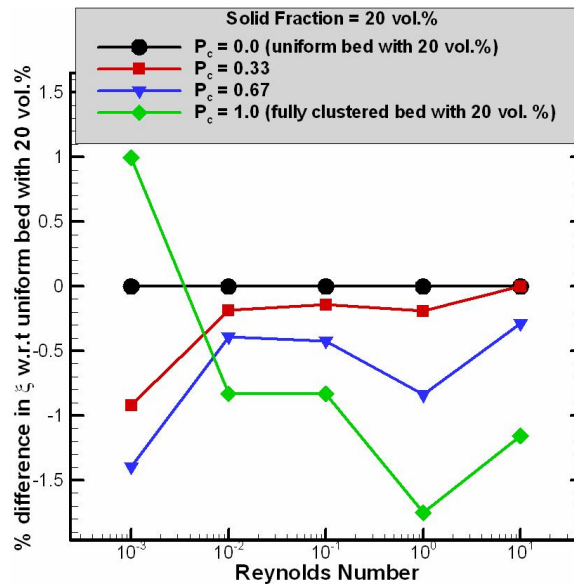


(b)

Figure 7.29: Effect of clustering in the frozen bed (40 vol. % loading) for desulfurization: (a) variation of log reduction with Reynolds number and (b) percentage difference in log reduction with respect to the uniform frozen bed



(a)



(b)

Figure 7.30: Effect of clustering in the frozen bed (20 vol. % loading) for desulfurization: (a) variation of log reduction with Reynolds number and (b) percentage difference in log reduction with respect to the uniform frozen bed

case. These small differences can be considered negligible since they are similar in magnitude to the numerical errors.

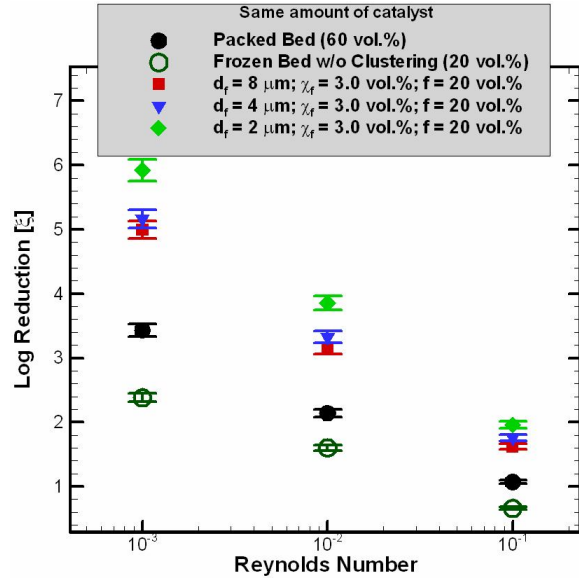
7.3.1.6 Effect of Fiber Diameter

Three different materials were modeled by varying the diameter of the fiber and maintaining constant fiber volume loading. The details of the material are given in Table 7.8.

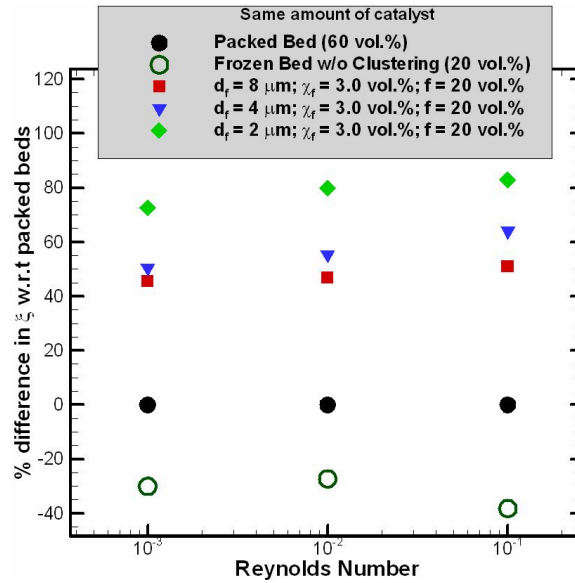
Table 7.8: Geometric properties of the microfibrinous materials modeled for CFD simulations to study the effect of fiber diameter

Material	Diameter of fiber (d_f)	Solid volume loading of the fiber (χ_f)	Diameter of particle (d_p)	Solid volume loading of the particle (χ_p)
Material-1	8 μm	3.0%	150 μm	20%
Material-2	4 μm	3.0%	150 μm	20%
Material-3	2 μm	3.0%	150 μm	20%

The diameter of the fibers are varied from 8 μm to 2 μm maintaining the rest of the parameters (diameter of particles d_p , solid volume loading of particles χ_p and fibers χ_f) constant.



(a)



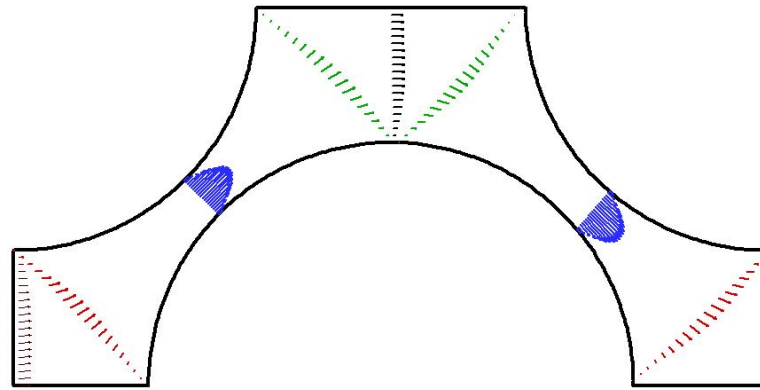
(b)

Figure 7.31: Effect of fiber diameter in microfibrus bed (20 vol. % loading) for desulfurization: (a) variation of log reduction with Reynolds number and (b) percentage difference in log reduction with respect to packed bed at 60 vol.% loading

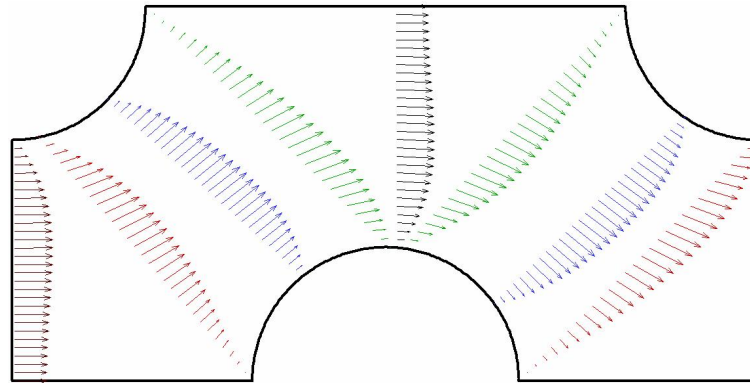
The effect of the fiber diameter has been studied and analyzed by plotting the log reduction on the Y-axis (linear scale) and Reynolds number on the X-axis (log scale) for all different materials as shown in Figure 7.31(a). Figure 7.31(a) shows that when the fibers are added to the frozen bed (20% solid volume loading), the log reduction is increased. If we observe Figure 7.27(b), we see that frozen bed with 20% volume loading has 30%-40% less chemical conversion when compared to packed beds. The fibers not only compensated for the negative effect of dilution with void but also increased the chemical conversion in comparison with packed beds. This can be clearly seen when we calculate the difference in log reduction with respect to packed beds as shown in Figure 7.31(b).

Figure 7.31(b) shows that when we add small fibers, the log reduction increased by 70-80% when compared to packed beds for same amount of catalyst. Also we see that when the fiber diameter is decreased from 8 to 2 μm , the log reduction increase by 20%.

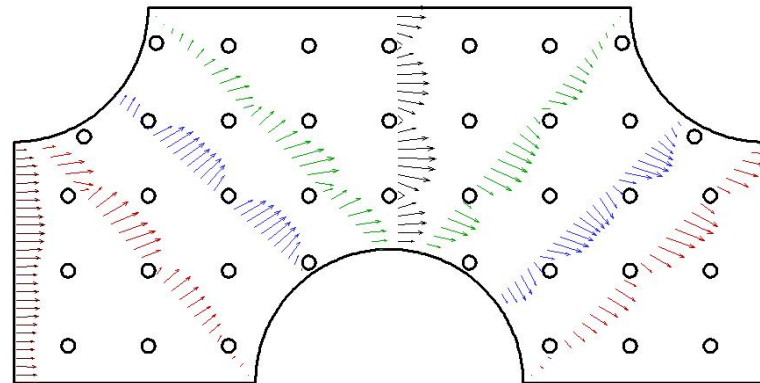
Figures 7.31(a) and 7.31(b) clearly shows that the diluting effect of fibers (i.e., moving the reactive particles away from each other) is not responsible for the increased reactivity. The increase in the chemical conversion is seen when we add fibers to the frozen bed because the fibers eliminate the peaking velocity and provides a more uniform flow. This is confirmed by Figures 7.32(a), 7.32(b), and 7.32(c) which



(a)



(b)



(c)

Figure 7.32: Effect of fibers on velocity profile: (a) packed bed (60 vol.% loading) (b) frozen bed (20 vol.% loading) (c) microfibrous bed bed (20 vol.% loading)

give velocity vectors for the packed bed, void-diluted bed, and fiber diluted bed, respectively. The velocity profiles shown in Figures 7.32(a), 7.32(b), and 7.32(c) are extracted from 3D simulations. In Figure 7.32(a), the velocity profile between the particles is parabolic with a high peaking velocity. When the bed is diluted with void (i.e., when the particles are moved away from each other), the velocity profile (shown in Figure 7.32(b)) between in the particles is still parabolic but the peaking velocity is less when compared to that of packed bed (in Figure 7.32(a)). When the fibers are added to the frozen bed, the peaking velocities between the particles are eliminated and provides a more uniform flow through out the bed as shown in Figure 7.32(c).

When the diameter of the fiber is decreased from 8 to 2 μm for the same fiber loading, the number of fibers will be increased by a factor of 16 which will further promote flow uniformity. Thus, we see more chemical conversion when we decrease the fiber diameter.

7.3.1.7 Effect of Fiber Loading

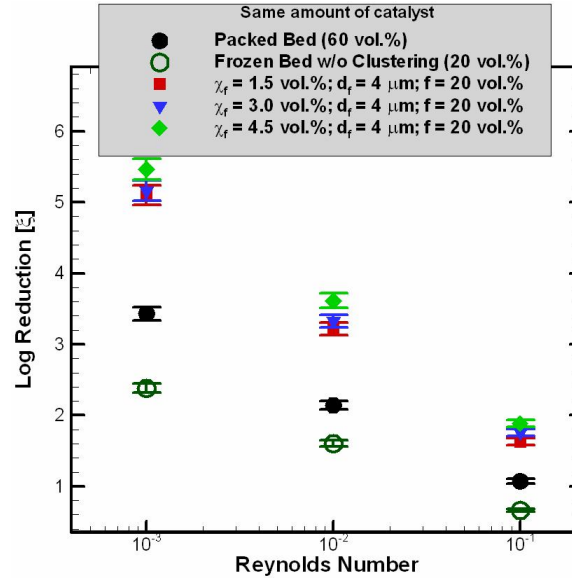
The effect of fiber loading has been studied in the same way that the effect of fiber diameter was studied. Three different materials were modeled by varying the fiber loading and maintaining a constant fiber diameter. The details of the material are given in Table 7.9.

Table 7.9: Geometric properties of the microfibrous materials modeled for CFD simulations to study the effect of fiber loading

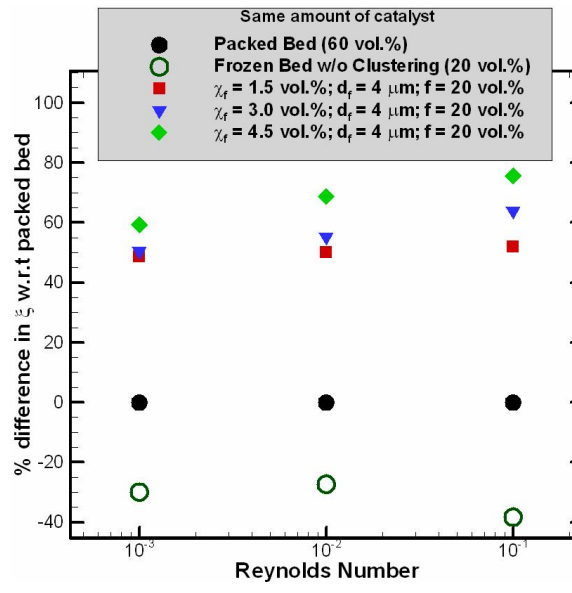
Material	Diameter of fiber (d_f)	Solid volume loading of the fiber (χ_f)	Diameter of particle (d_p)	Solid volume loading of the particle (χ_p)
Material-4	4 μm	1.5%	150 μm	20%
Material-2	4 μm	3.0%	150 μm	20%
Material-5	4 μm	4.5%	150 μm	20%

The volume loading of the fibers is varied from 1.5% to 4.5% maintaining the rest of the parameters (diameter of particles d_p , solid volume loading of particles χ_p and diameter of the fibers d_f) constant.

The effect of fiber loading has been studied and analyzed by plotting log reduction on the Y-axis (linear scale) and Reynolds number on the X-axis (log scale) for all different materials as shown in Figure 7.33(a). The same trend, an increase in chemical conversion with the addition of fibers, has been observed in this study also. When the solid volume loading of the fibers increased from 1.5% to 4.5%, the number of fibers increases by a factor of three and the log reduction increased by 10-25%. It is shown that an increase in volume loading increases the number of fibers and in turn



(a)

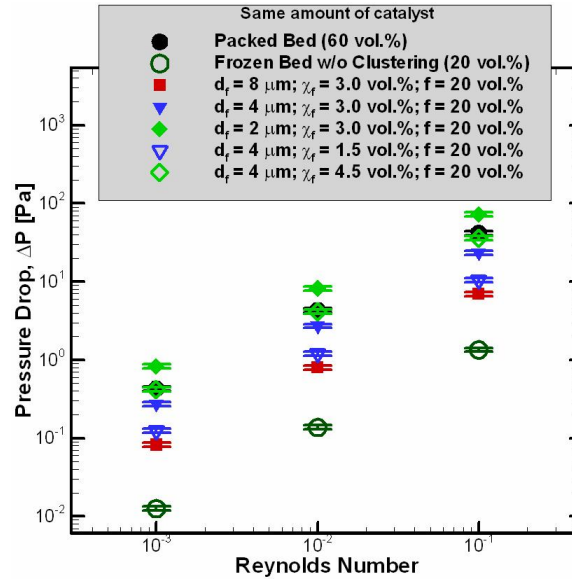


(b)

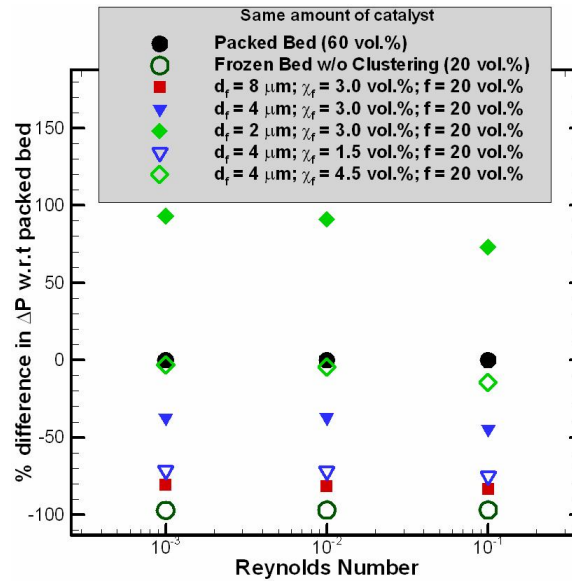
Figure 7.33: Effect of fiber loading in microfibrus bed (20 vol. % loading) for desulfurization: (a) variation of log reduction with Reynolds number and (b) percentage difference in log reduction with respect to packed bed at 60 vol.% loading

increases the chemical conversion. As was the case for the fiber diameter study, an increase in the fiber loading serves to promote flow uniformity.

Pressure drop is one of the main factors in designing reactor beds. Pressure drops predicted in packed beds, frozen beds, and various microfibrinous materials (Materials 1 to 5) at different Reynolds numbers are plotted in Figure 7.34(a). It is observed that pressure drop decreased when the packed bed is diluted with void. As the fibers are added to the diluted bed they impede the flow and increase the pressure drop in the bed. Although the pressure drop in the microfibrinous material is higher than that of the diluted bed, it is generally less when compared to a typical packed bed except for one material (i.e., with many small diameter fibers). Figure 7.34(b) shows the percentage difference in pressure drop with respect to packed bed. It is shown that except for one material (with many small diameter fibers) the rest of the microfibrinous materials have lower pressure drops when compared to the packed bed.



(a)



(b)

Figure 7.34: Effect of fibers on pressure drop for desulfurization: (a) variation of pressure drop with Reynolds number and (b) percentage difference in the pressure drop with respect to packed bed (60 vol.% loading)

7.3.2 Hexane Removal

Removal of trace amounts of hexane from air is studied because it is often used as a laboratory surrogate for the nerve gas Sarin (as discussed in Section 2.2.4) is studied. In this section we discuss how the chemical reaction is modeled and the underlying assumptions made. We will also discuss the results obtained from numerical experiments performed to study the effects of clustering and dilution on chemical conversion during the process of hexane removal from air in packed beds and microfibrinous materials. Due to limitations in experimental data, these results are not validated experimentally.

The geometric models used in this study are same as those used for desulfurization study. In this study, the surfaces of the particles are defined as catalytically reacting walls. These surface walls are assumed to be highly reactive and the reaction rate is very high compared to diffusion. Thus, this reaction is purely external mass transfer controlled. It is also assumed that the particles are perfect adsorbants, whereas in reality the hexane reaction rate changes with time. Thus, before the catalytic surface gets polluted, the reaction is extremely fast. In this study, we assume that the particles do not get polluted and thus modeled the reaction as infinitely fast. For infinitely fast reactions, the concentration of the species is fixed to be zero on the surface of the particles. For the case of microfibrinous materials, fiber surfaces

are defined as inert walls. The temperature on the walls (both reacting and inert) is defined as 40 °C to be consistent with experiments.

Operating conditions and fluid properties used in this study are tabulated in Table 7.10.

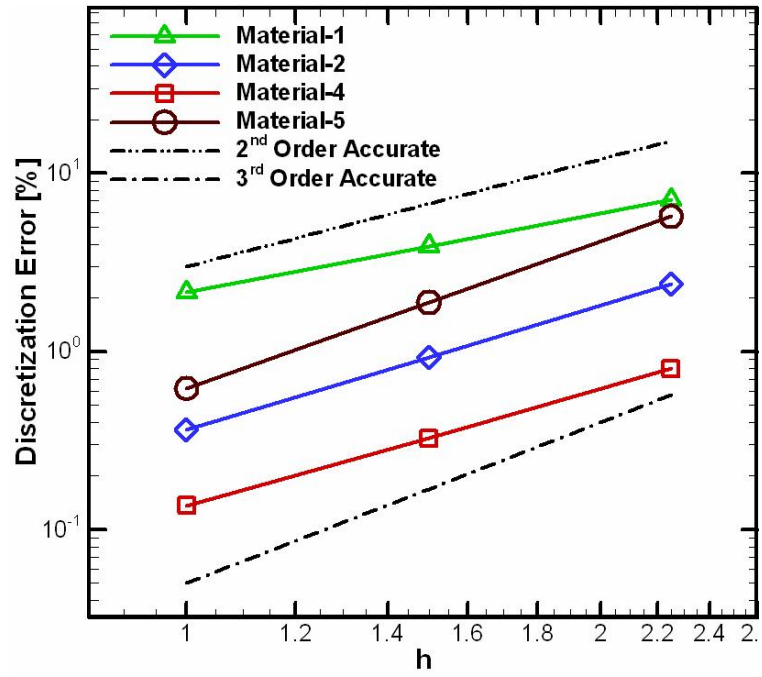
Table 7.10: Operating conditions and fluid properties for hexane study

Reaction	Inlet Conc.	Temperature (°C)	Operating Pressure (Pa)	Diffusivity	Viscosity
$C_6H_{14} + Air \longrightarrow$ <i>Air</i>	100 ppmv	40	10312	0.083 cm ² /s	1.9×10^{-5} kg/m-s

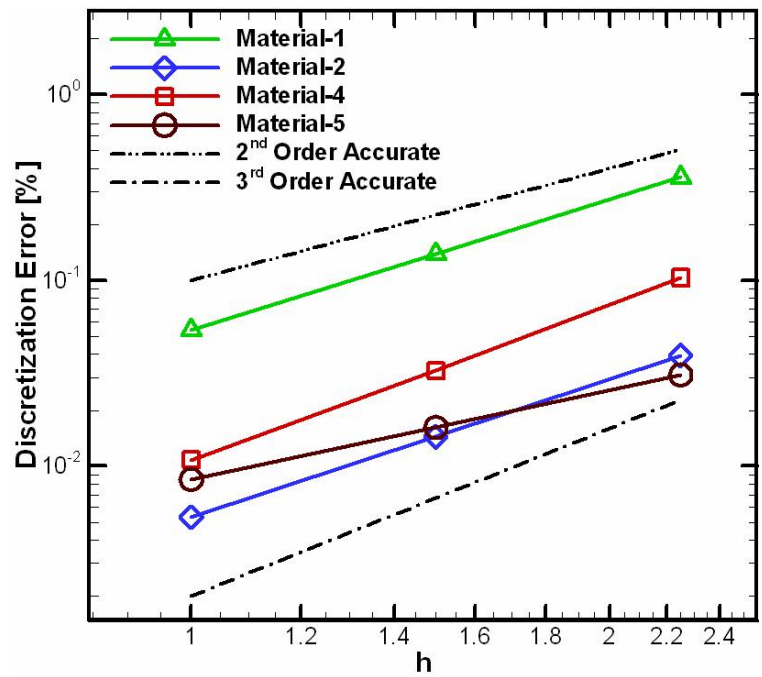
7.3.2.1 Numerical Accuracy

Three flow-field grids were generated by uniformly refining each cell in the domain by a factor of 1.5 in all three directions (X, Y, and Z). The exact solution for the log reduction and pressure drop per unit length is estimated from generalized Richardson extrapolation [84] using Equation 7.2. The relative discretization error in log reduction and pressure gradient for different materials (materials 1, 2, 4 and 5) were plotted against the grid refinement parameter h to estimate the order of accuracy and is shown in Figures 7.35(a) and 7.35(b), respectively.

The slope of the lines in Figures 7.35(a) and 7.35(b) gives the observed order of accuracy. While predicting log reduction in microfibrous materials, the slope of the



(a)



(b)

Figure 7.35: Discretization error for different microfibrous materials: (a) log reduction; (b) pressure drop

lines shown in Figure 7.35(a) is between 1.6 and 3.2; while predicting pressure drop in microfibrinous materials, the slope of the lines shown in Figure 7.35(b) is between 1.8 and 3.2. Table 7.11 shows the order of accuracy obtained (using Equation 2.24) while predicting log reduction and pressure drop in microfibrinous materials.

Discretization error estimates in these numerical simulations are tabulated in Table 7.11 along with the details of the log reduction and pressure gradients. It is observed that the estimated discretization errors range from 0.13-2.1% (fine grid) to 0.8-7.1% (coarse grid) in predicting log reduction and from 0.005-0.05% (fine grid) to 0.03-0.3% (coarse grid) in predicting pressure gradient. This estimated discretization error provides guidance in choosing an appropriate grid. The medium grid is used for all simulations presented in this study which has maximum discretization error estimates of 4.0% and 0.2% while predicting log reduction and pressure gradient, respectively. Numerical uncertainty is shown in all the simulation results discussed in this section by plotting error bars using these error estimates.

7.3.2.2 Effect of Dilution with Void

The effect of dilution on the log reduction is studied in the same way as for the desulfurization case. As discussed in Section 7.3.1.4, the original packed beds with 60% solid volume loading were diluted with 20% and 40% void resulting in frozen beds with 40% and 20% solid volume loading. Figures 7.26(a) and 7.26(b) show the

Table 7.11: Discretization error in log reduction and pressure gradient for different microfibrinous materials for hexane removal

	Grid Level	Solution	Order of Accuracy	Estimated Exact Solution	Estimated Discretization Error [%]
MATERIAL-1: $d_p = 150 \mu\text{m}$; $d_f = 8 \mu\text{m}$; $\chi_p = 20 \text{ vol.}\%$; $\chi_f = 3.0 \text{ vol.}\%$					
Log Reduction	Fine	23.95	1.668	24.47	2.1529
	Medium	23.52			3.9097
	Coarse	22.73			7.1372
Pressure Gradient	Fine	13,060.	2.633	13,067	0.053
	Medium	13,049.			0.138
	Coarse	13,021.			0.358
MATERIAL-2: $d_p = 150 \mu\text{m}$; $d_f = 4 \mu\text{m}$; $\chi_p = 20 \text{ vol.}\%$; $\chi_f = 3.0 \text{ vol.}\%$					
Log Reduction	Fine	26.409	2.721	26.505	0.3635
	Medium	26.26			0.926
	Coarse	25.869			2.401
Pressure Gradient	Fine	43,285.	2.88	43,287.	0.005
	Medium	43,281.			0.014
	Coarse	43,270.			0.0395
MATERIAL-4: $d_p = 150 \mu\text{m}$; $d_f = 4 \mu\text{m}$; $\chi_p = 20 \text{ vol.}\%$; $\chi_f = 1.5 \text{ vol.}\%$					
Log Reduction	Fine	26.30	2.489	26.33	0.1362
	Medium	26.25			0.3261
	Coarse	26.125			0.8007
Pressure Gradient	Fine	19,329.	3.168	19,332.	0.010
	Medium	19,325.			0.0327
	Coarse	19,312.			0.1032
MATERIAL-5: $d_p = 150 \mu\text{m}$; $d_f = 4 \mu\text{m}$; $\chi_p = 20 \text{ vol.}\%$; $\chi_f = 4.5 \text{ vol.}\%$					
Log Reduction	Fine	27.05	3.172	27.22	0.620
	Medium	26.70			1.888
	Coarse	26.65			5.744
Pressure Gradient	Fine	66,431.	1.840	66,436.	0.008
	Medium	66,425.			0.0162
	Coarse	66,416.			0.031

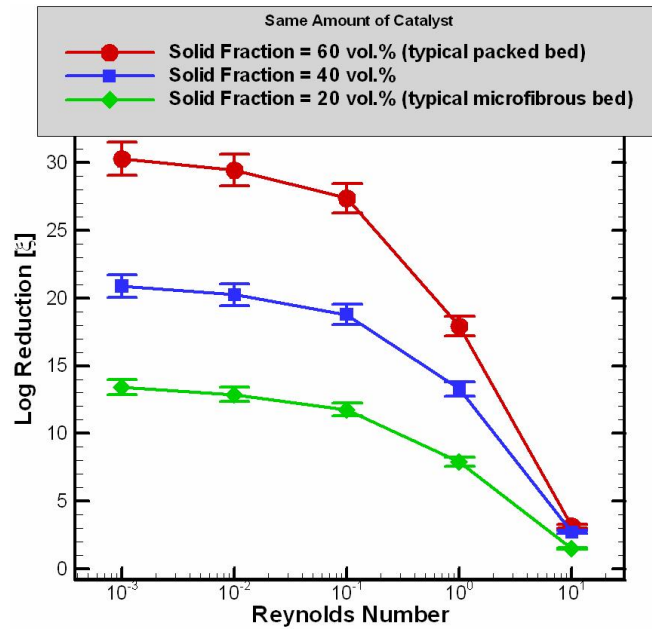
difference between the geometric model of packed bed (60% solid volume loading) and a frozen bed (5% solid volume loading), respectively.

The log reduction obtained from simulation is plotted versus Reynolds number for various solid fractions and is shown in Figure 7.36(a). It is observed that the log reduction decreases when the packed bed is diluted with void.

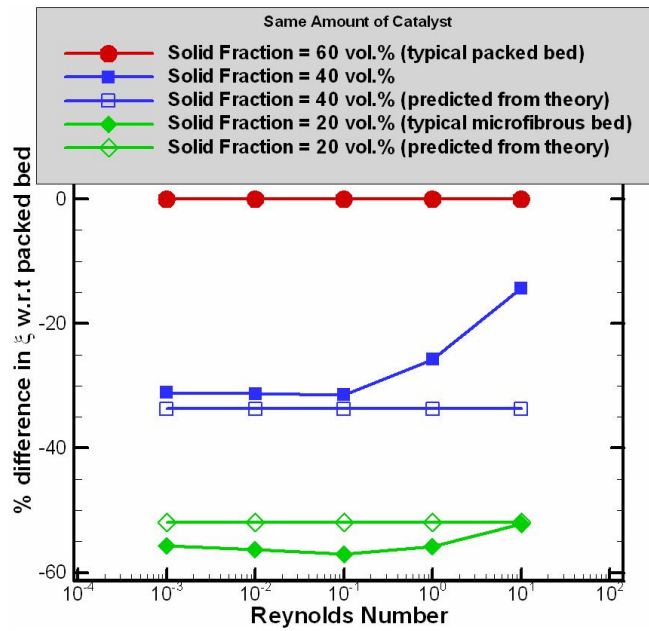
Equation 7.12 is used to estimate the effect of dilution with void. The percentage difference in log reduction with respect to packed bed at 60% volume loading is plotted versus Reynolds number in Figure 7.36(b) along with the results obtained from simulations. Simulation and theory predictions are very close and it is observed that when the packed bed is diluted with 20% void, the log reduction decreased by 30% at low velocities and 10-25% at high velocities. When the packed bed is diluted with 40% void, the log reduction decreased by 55%. From Equation 7.12, when a packed bed is diluted by 20% and 40% void, the log reduction is decrease by 35% and 50% respectively. The same trend is observed (dilution with void has a negative effect on log reduction) for both desulfurization and hexane removal irrespective of diffusivity and viscosity difference.

7.3.2.3 Effect of Clustering

As we discussed in Section 7.3.1.5, clustering parameter (Equation 7.28) is used to study the effect of clustering. Two solid volume fractions (40 vol.% and 20 vol.%) and



(a)



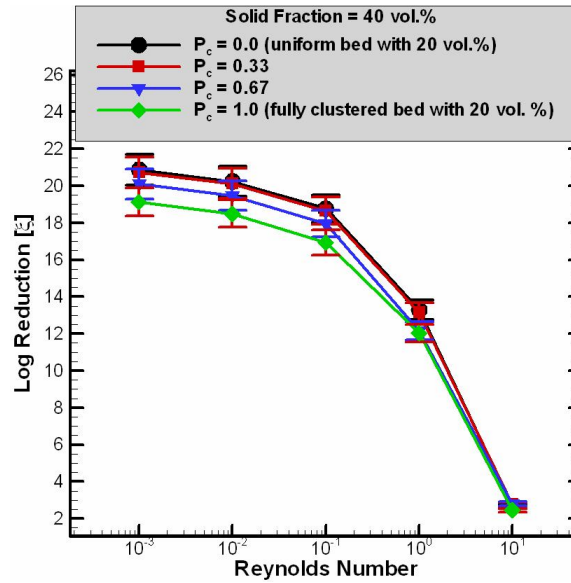
(b)

Figure 7.36: Effect of dilution for hexane removal: (a) variation of log reduction with Reynolds number and (b) percentage difference in log reduction with respect to packed bed at 60 vol.% loading

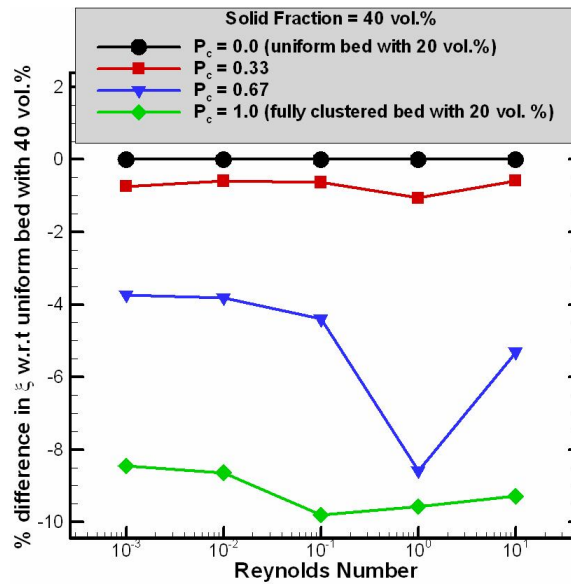
four clustering parameters ($P_c = 0, 0.33, 0.67, \text{ and } 1.0$) were used to analyze the effect of clustering on chemical conversion to remove trace amounts of hexane from air.

The effect of clustering in the frozen bed with 40% solid volume loading is shown in Figure 7.37. Log reduction is plotted versus Reynolds number for different clustering parameters in Figure 7.37(a). It is observed that clustering of particles in the frozen bed has some effect on chemical conversion for hexane. This can be clearly seen in Figure 7.37(b) where the percentage difference in log reduction is calculated with respect to a uniform frozen bed ($P_c = 0$) and plotted versus Reynolds number. Figure 7.37(b) shows that as the clustering parameter increases (i.e., corner particles move towards center particles), the chemical conversion decreases. When the clustering parameter is 0.33, the difference is very small and can be neglected as it is similar in magnitude to the numerical errors that are discussed above. However, when the clustering parameter is increased to 0.67 and 1.0, the log reduction decreased by 4-6% and 8-10% with respect to a uniform bed whose clustering parameter is zero.

A similar analysis is done with the frozen bed with 20% solid volume loading. Log reduction is plotted versus Reynolds number for different clustering parameters in Figure 7.38(a). It is observed that clustering of particles in the frozen bed with 20% solid volume loading has a larger negative effect on chemical conversion when compared to the frozen bed with 40% solid volume loading. The percentage error in log reduction with respect to the uniform bed ($P_c=0$) is plotted for different clustering

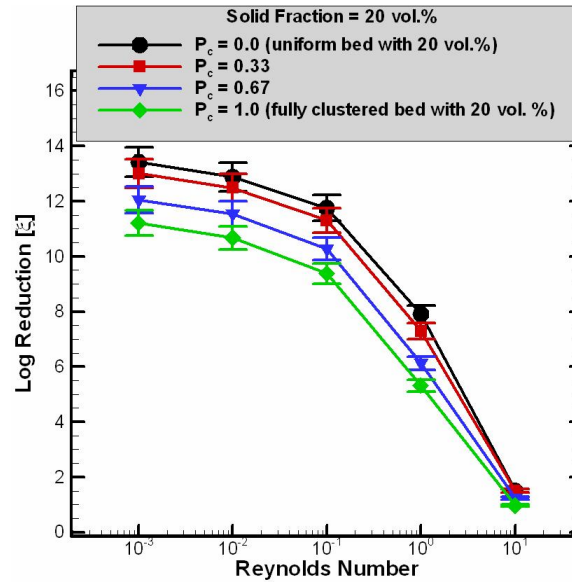


(a)

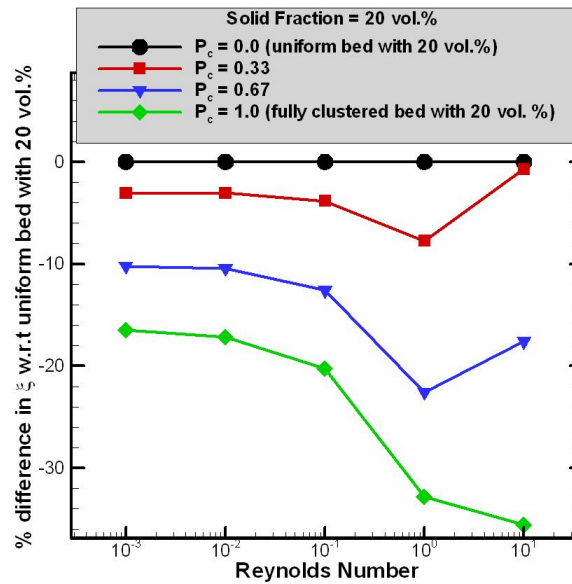


(b)

Figure 7.37: Effect of clustering in a frozen bed (40 vol. % loading) for hexane removal: (a) variation of log reduction with Reynolds number and (b) percentage difference in log reduction with respect to a uniform frozen bed



(a)



(b)

Figure 7.38: Effect of clustering in frozen bed (20 vol. % loading) for hexane removal: (a) variation of log reduction with Reynolds number and (b) percentage difference in log reduction with respect to uniform frozen bed

parameters and is shown in Figure 7.38(b). As we increase the clustering parameter, we see less chemical conversion. When the clustering parameter is small ($=0.33$), the difference is in the magnitude of the numerical error and can be neglected. Whereas when the clustering parameter increased to 1.0, the chemical conversion decreased by 20-28% at low Reynolds numbers and by 30-40% at high Reynolds numbers.

This negative effect of clustering on log reduction can be explained on the basis of the mass diffusivity of the challenge gas. In the case of desulfurization, the mass diffusivity of the challenge gas is $2.8 \text{ cm}^2/\text{s}$, which is relatively high. Thus, the molecules can radially diffuse quickly and can thus still see the reacting particles. Whereas in the case of hexane removal, the mass diffusivity of the challenge gas is $0.086 \text{ cm}^2/\text{s}$, which is 30 times smaller than that of challenge gas used for desulfurization. At this low mass diffusivity, the molecules of the challenge gas do not have enough time to diffuse radially and see the entire surface area of the reacting particles when they are clustered. The molecules bypass the cluster, effectively treating the cluster of particles as a single large particle, thus resulting in reduced chemical conversion.

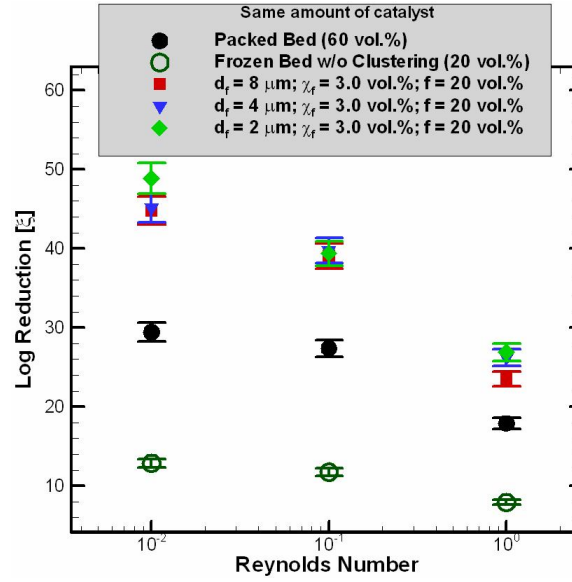
7.3.2.4 Effect of Fiber Diameter

The same materials (materials 1-3) that were used to study the effect of fiber diameter in the desulfurization case are also used to study hexane removal. The diameter of the fibers is varied from $8 \mu\text{m}$ to $2 \mu\text{m}$ while maintaining the rest of the

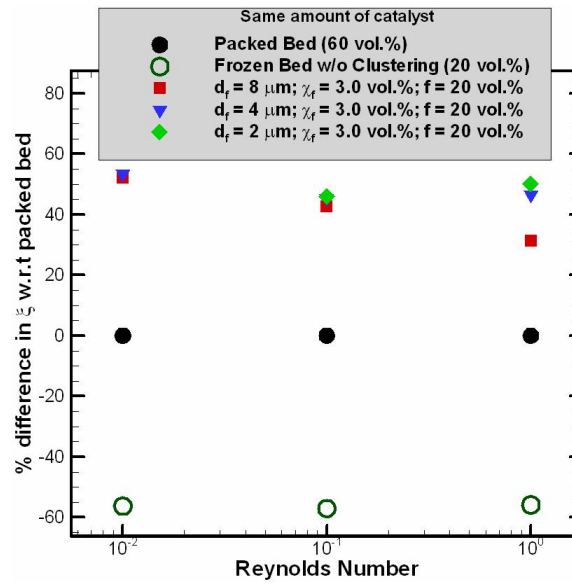
parameters (d_p , χ_p , and χ_f) constant. The geometric details of the materials used in this section were given in Table 7.8.

The effect of fiber diameter has been studied and analyzed by plotting log reduction on the Y-axis and Reynolds number on the X-axis for all three materials along with packed beds (60 vol.% loading) and frozen beds (20 vol.% loading) in Figure 7.39(a). All comparisons were made for the same amount of catalyst loading. It is observed that irrespective of the diameter of the fibers, when the fibers are added to frozen beds, the log reduction increased. In this case also, fibers not only compensated for the negative effect of dilution with void but also increase chemical conversion relative to the packed bed, similar to what was observed for desulfurization.

When the fibers are added, we see roughly a 60% increase in chemical conversion with respect to packed beds as shown in Figure 7.39(b). Though the diameter of the fibers is varied, there is not much effect on chemical conversion. When the fiber diameter is reduced from 8 μm to 2 μm , the chemical conversion increased by just 10 %. Similar to the case of desulfurization, decreasing the diameter of the fibers increases the number of fibers which promotes more flow uniformity and thus increases reactivity.



(a)



(b)

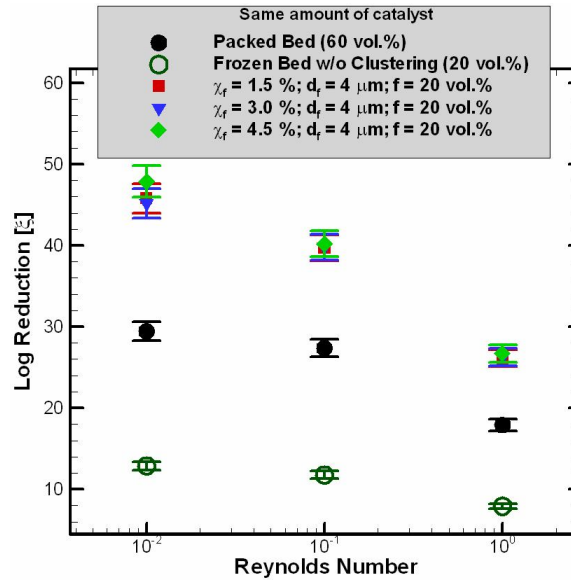
Figure 7.39: Effect of fiber diameter in microfibrus beds (20 vol. % loading) for hexane removal: (a) variation of log reduction with Reynolds number and (b) percentage difference in log reduction with respect to packed bed at 60 vol.% loading

7.3.2.5 Effect of Fiber Loading

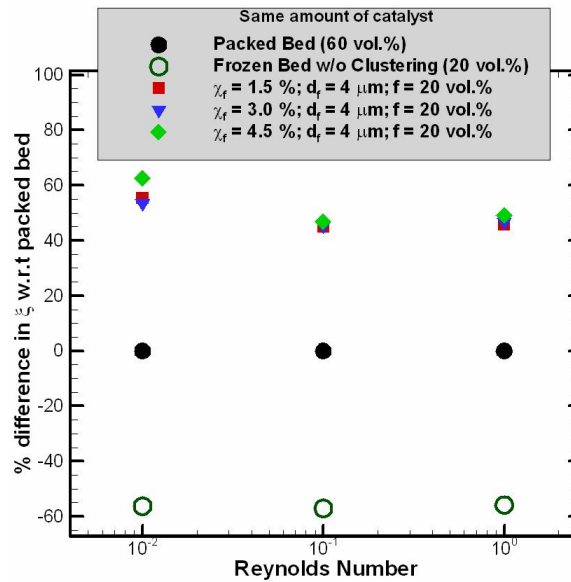
The same materials (materials 2, 4, and 5) that were used to study the effect of fiber fraction in desulfurization case are used in this section for hexane removal. The volume loading of the fibers is varied from 1.5% to 4.5% while maintaining the rest of the parameters (d_p , d_f , and χ_p) constant. The geometric details of the materials used in this section were given in Table 7.9.

The effect of fiber loading has been studied and analyzed by plotting log reduction versus Reynolds numbers for the three materials along with packed beds (60 vol.% loading) and frozen beds (20 vol.% loading) as shown in Figure 7.40(a). The effect of fiber loading on the log reduction is smaller when compared to the effect of fiber diameter. When different fibers were added to frozen beds, irrespective of fiber loading, Figure 7.33(b) shows that log reduction increased by 50-60% with respect to packed bed.

As discussed in Section 7.3.1.7, pressure drop is one of the main factors to consider when designing reactor beds. During the removal of hexane from air, the pressure drop was predicted in packed beds, various microfibrinous materials, and frozen beds using the CFD simulations. The pressure drop predicted by the simulations in different geometries are for the same amount of catalyst loading. Pressure drop is plotted versus Reynolds number for all different geometries discussed in this section in Figure 7.41(a). It is observed that the pressure drop decreased when the packed bed is diluted with

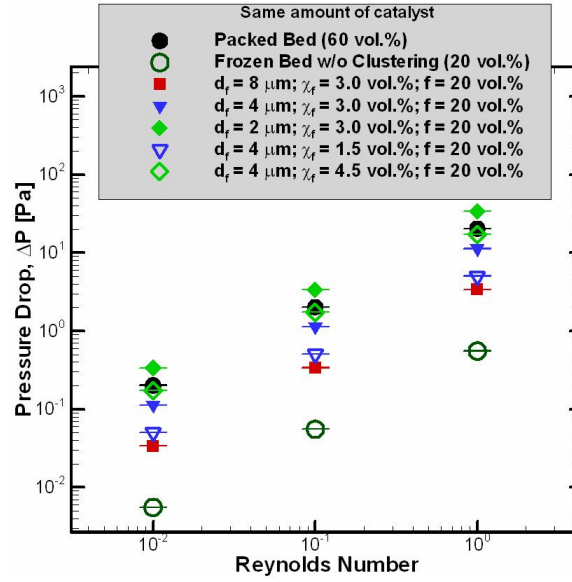


(a)

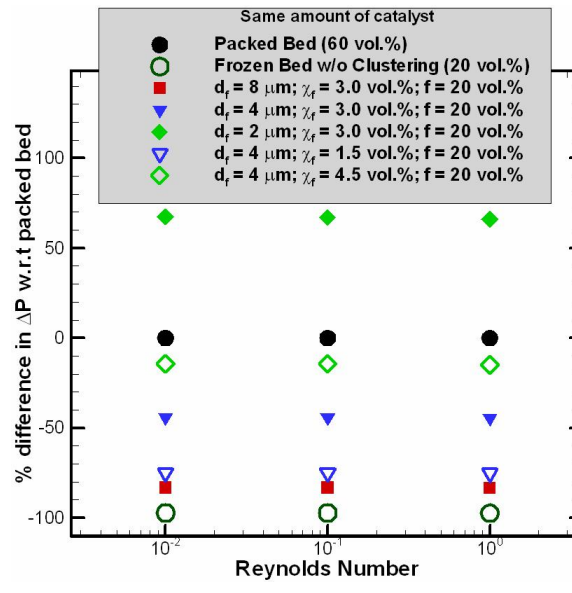


(b)

Figure 7.40: Effect of fiber loading in Microfibrous bed (20 vol. % loading) for hexane removal: (a) variation of log reduction with Reynolds number and (b) percentage difference in log reduction with respect to packed bed at 60 vol.% loading



(a)



(b)

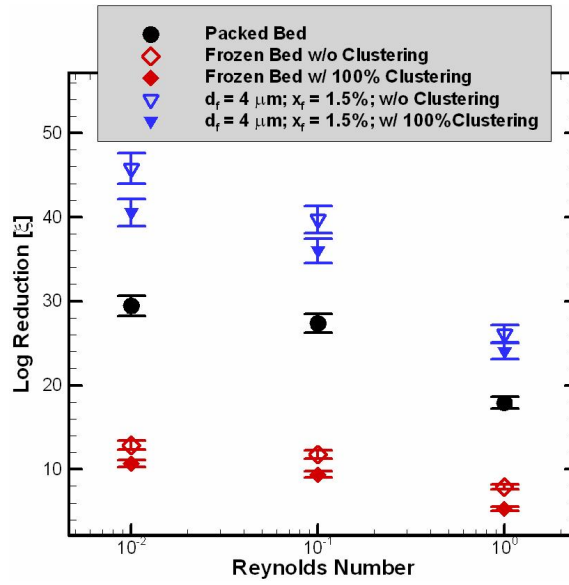
Figure 7.41: Effect of fibers on pressure gradient: (a) variation of pressure drop with Reynolds number and (b) percentage difference in the pressure drop with respect to the packed bed with 60 vol.% loading

void. When the fibers were added to the frozen bed, then the pressure drop increased. Except for the material with numerous, small diameter fibers, the other materials have low pressure drops when compared to packed beds. The percentage difference in the pressure drop with respect to the packed bed is plotted against Reynolds number in Figure 7.41(b). It is shown that for the material with numerous, small diameter fibers the pressure drop is nearly 70% higher compared to the packed bed; whereas for the rest of the materials, the pressure drop is smaller by up to a factor of two.

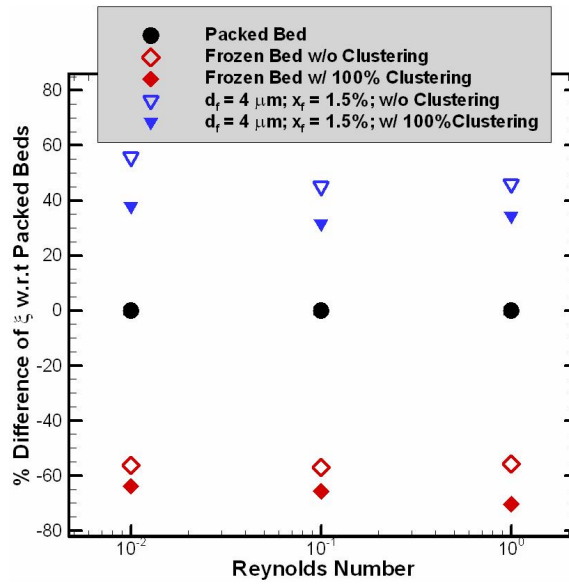
7.3.2.6 Effect of Clustering in Microfibrous Materials

In Section 7.3.2.3, we observed that clustering of the particles has a negative effect on log reduction when the diffusivity of the challenge gas is low. The effect of clustering is studied and analyzed in microfibrous materials to see whether fibers can mitigate the negative effects of particle clustering on the reactivity.

Due to complications in generating the clustered microfibrous material with a large number of fibers, only three materials were modeled and analyzed in this study. For simplicity, all three materials were modeled with maximum clustering (i.e., $P_c=1.0$). The geometric properties of the materials used are tabulated in Table 7.12.



(a)



(b)

Figure 7.42: Effect of clustering in microfibrus beds ($d_p = 150 \mu\text{m}$; $d_f = 4 \mu\text{m}$; $\chi_p = 20 \text{ vol.}\%$; $\chi_f = 1.5 \text{ vol.}\%$): (a) variation of log reduction with Reynolds number and (b) percentage difference in log reduction with respect to packed bed at 60 vol.% loading

Table 7.12: Geometric properties of the microfibrous materials modeled for CFD simulations to study the effect of clustering in microfibrous materials

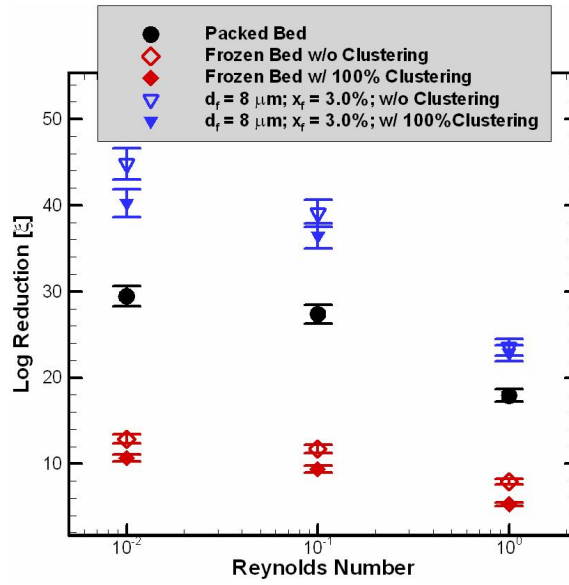
Material	Diameter of fiber (d_f)	Solid volume loading of the fiber (χ_f)	Diameter of particle (d_p)	Solid volume loading of the particle (χ_p)
Material-1	8 μm	3.0%	150 μm	20%
Material-2	4 μm	3.0%	150 μm	20%
Material-4	4 μm	1.5%	150 μm	20%

The effect of clustering on microfibrous materials has been studied and analyzed by plotting log reduction on Y-axis (linear scale) and Reynolds number on the X-axis (log scale) for materials 1, 2, and 4 (with a clustering parameter of one) which are shown in Figures 7.42(a), 7.43(a), and 7.44(a), respectively. In all these three figures, results obtained for materials 1, 2, and 4 (with a clustering parameter of one) were compared to packed beds and frozen beds (with a clustering parameter of zero and one) along with materials 1, 2, and 4 with a clustering parameter of zero. It is observed that when the fibers are added to the highly clustered ($P_c=1.0$) frozen bed, the log reduction increased by 35-40%. When the particles in frozen beds are moved closer to maximum clustering, the log reduction decreased by 55-60% when compared to packed beds and decreased by 20-35% when compared to frozen beds

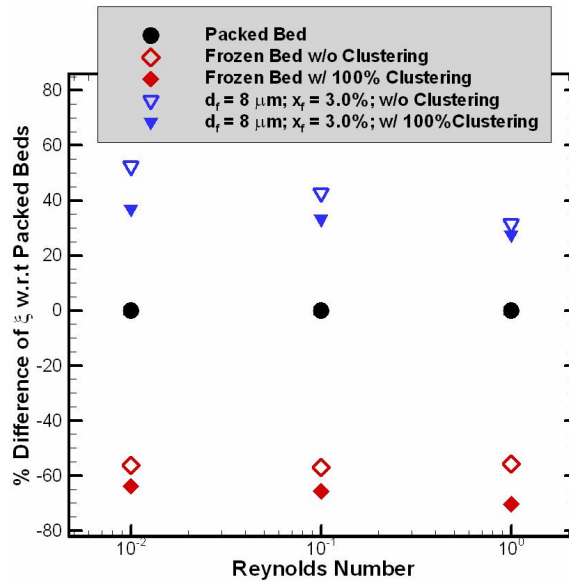
without clustering. However, when fibers are added, the clustering effect is minimized, thereby increasing the chemical conversion of the clustered bed.

The percentage difference in log reduction for all these materials with respect to the packed bed is plotted versus Reynolds number in Figures 7.42(b), 7.43(b), and 7.44(b). It is observed that when the fibers were added to the maximum clustered frozen bed (20 vol.% loading, $P_c=1.0$), the log reduction increased by 40% compared to the packed bed, but decreased only by 5-10% when compared to the same microfibrinous material without clustering.

If we re-examine Figure 7.38(b), the maximum clustered ($P_c=1.0$) frozen bed had 20-35% less reactivity when compared to the uniform bed (i.e., the frozen bed without clustering). Now, when fibers are added to both frozen beds, the reduction is only 5-10%. This tells us that fibers help in mitigating the effects of clustering by promoting flow uniformity in the material, thus increasing chemical reactivity.

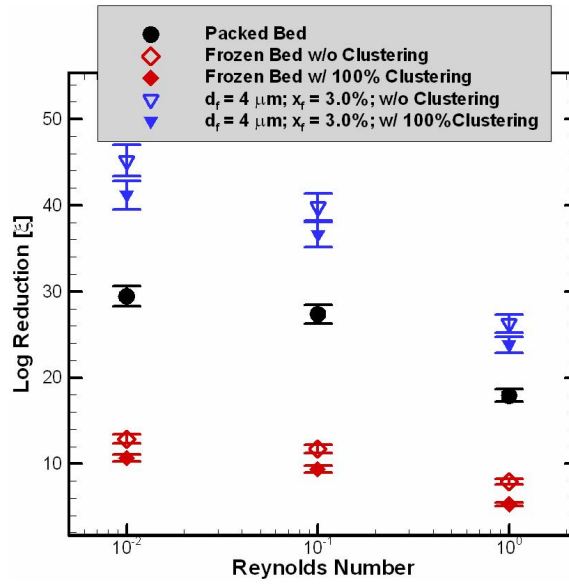


(a)

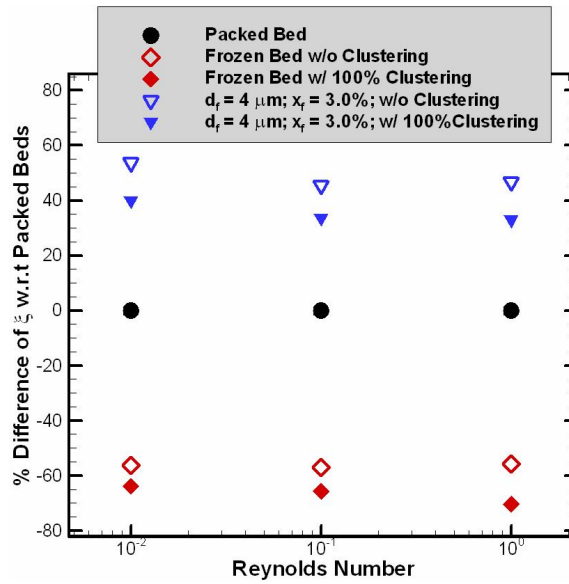


(b)

Figure 7.43: Effect of clustering in microfibrus beds ($d_p = 150 \mu\text{m}$; $d_f = 8 \mu\text{m}$; $\chi_p = 20 \text{ vol.}\%$; $\chi_f = 3.0 \text{ vol.}\%$): (a) variation of log reduction with Reynolds number and (b) percentage difference in log reduction with respect to packed bed at 60 vol.% loading



(a)



(b)

Figure 7.44: Effect of clustering in microfibrus beds ($d_p = 150 \mu\text{m}$; $d_f = 4 \mu\text{m}$; $\chi_p = 20 \text{ vol.}\%$; $\chi_f = 3.0 \text{ vol.}\%$): (a) variation of log reduction with Reynolds number and (b) percentage difference in log reduction with respect to packed bed at 60 vol.% loading

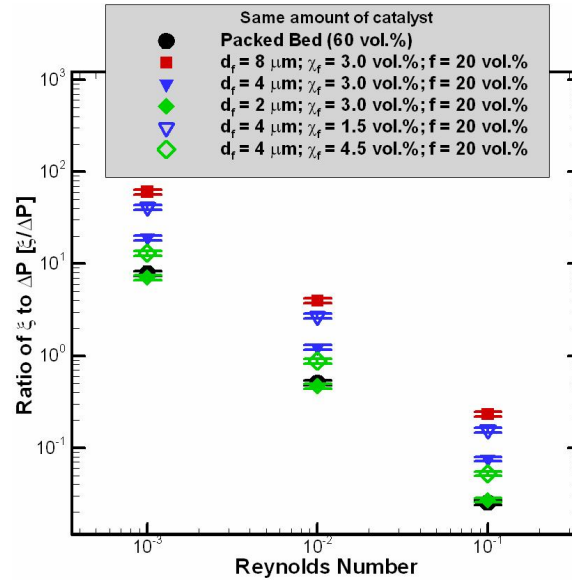
CHAPTER 8

SIMULATION BASED DESIGN OF NEW MICROFIBROUS MATERIALS

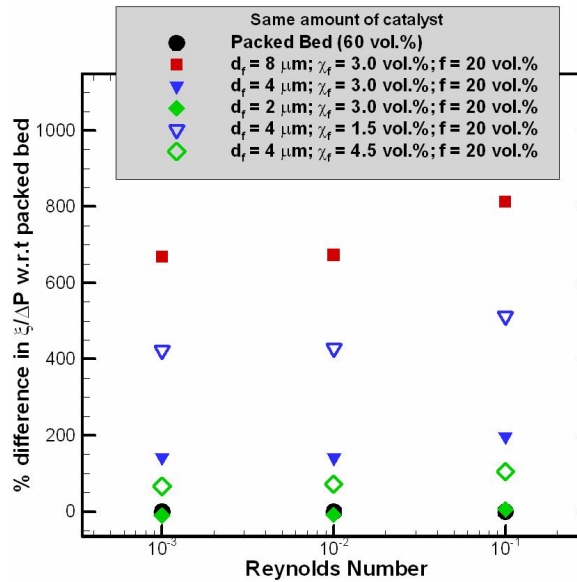
8.1 Desulfurization

The ultimate goal of this work is to use CFD as a design tool and propose a design space for new microfibrinous materials with enhanced chemical reactivity. In order design a new material for desulfurization, it is necessary to analyze the pressure drop along with the chemical conversion. Thus, a new parameter is defined which includes the both pressure drop and chemical conversion. It is defined as the ratio of the log reduction to the pressure drop for a fixed amount of catalyst, where larger ratios indicate better materials.

The ratio of log reduction to pressure drop is plotted against Reynolds number for different microfibrinous materials and is compared with packed beds in Figure 8.1(a). Figure 8.1(b) shows that for all microfibrinous materials examined, the ratio is higher than the packed bed ratio except for one material (i.e., the one with many, small diameter fibers). When the material is made of small fibers, the ratio is 5% smaller compared to packed beds. For the rest of the materials, the ratio is higher by a factor of two to six when compared to packed beds.



(a)



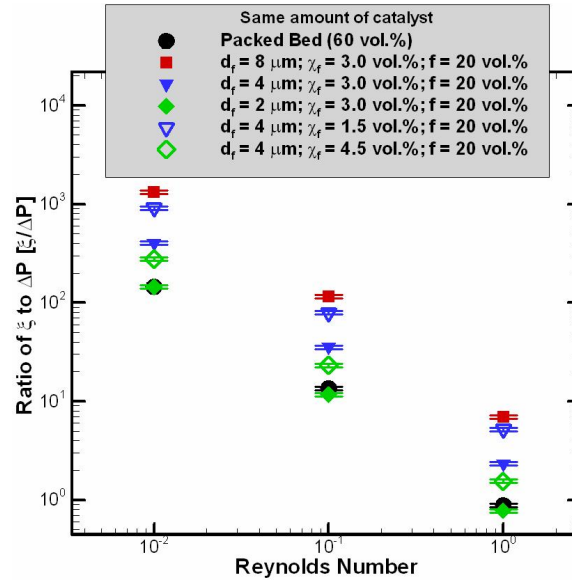
(b)

Figure 8.1: Effect of fibers on ratio of log reduction to pressure gradient for desulfurization: (a) variation of the ratio with Reynolds number and (b) percentage difference in the ratio with respect to packed bed (60 vol.% loading)

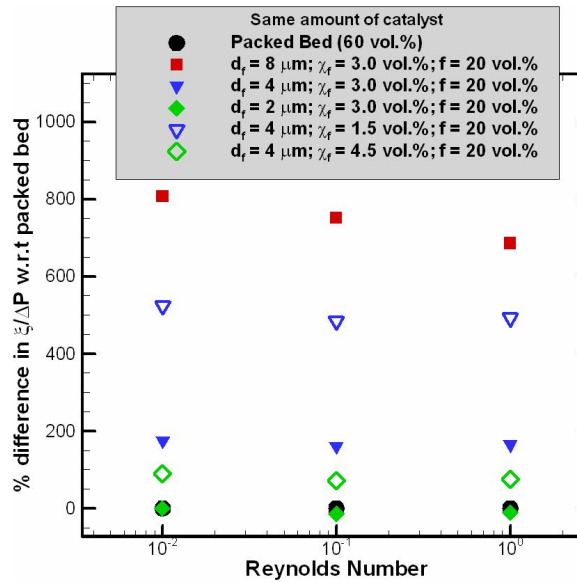
8.2 Hexane Removal

The ratio of log reduction to pressure drop is plotted against Reynolds number for different microfibrinous materials and is compared with packed beds for the case of hexane removal in air in Figure 8.2(a). Figure 8.1(b) shows that for all microfibrinous materials examined, the ratio is higher than the packed bed ratio except for one material (again, the one with many, small diameter fibers). When the material is made of small fibers, the ratio is nearly equal to packed bed ratio. For the rest of the materials, the ratio is higher by a factor of two to eight when compared to packed beds.

According to this study, chemical conversion for both desulfurization and hexane removal in air depends on the number of fibers in the material. Based on our current findings, we need fewer larger diameter fibers in order to obtain enhanced chemical reactivity for a given pressure drop across the bed when compared to typical packed beds (assuming the same amount of catalyst is used). If the pressure drop in the reactor is not an important factor, then we need many smaller diameter fibers as it is giving nearly 80% and 60% higher conversion for desulfurization and hexane removal, respectively, when compared to packed beds.



(a)



(b)

Figure 8.2: Effect of fibers on ratio of log reduction to pressure gradient for hexane removal: (a) variation of the ratio with Reynolds number and (b) percentage difference in the ratio with respect to packed bed (60 vol.% loading)

CHAPTER 9

SUMMARY AND CONCLUSIONS

The goal of this research was to develop a design space for new microfibrinous materials with enhanced chemical reactivity. In order to achieve the goal, the research has been done in three phases:

1. FLUID DYNAMICS OF THE FLOW: CFD has been used to predict the pressure drop in packed beds, frozen/immobilized beds, and microfibrinous materials and then compared to empirical correlations like the Ergun equation [48] and the PMP equation [3] along with experimental data.
2. CHEMICAL REACTIONS: CFD has been used to study the effect of residence time, channeling/flow maldistribution, and dilution with void in packed beds and frozen beds. The effect of fiber diameter and fiber volume loading on the log-reduction in microfibrinous materials has also been analyzed. This task provides a better understanding of surface reaction phenomena in microfibrinous materials
3. PROPOSAL OF DESIGN SPACE: Based on the understanding of the basic physical and chemical processes that occur in microfibrinous flows, a design space

for new microfibrinous material with enhanced chemical reactivity with optimum pressure drop has been proposed.

In this chapter, various numerical experiments that are performed in each phase are summarized and the results are discussed briefly.

FLUID DYNAMICS OF THE FLOW: In this phase, the goal is to analyze the flow through the microfibrinous material and predict pressure drop. All the results obtained during this phase are discussed in Section 7.1. Pressure drop was predicted in packed beds (60 vol.% loading), frozen/immobilized beds (20-50 vol% loading), and microfibrinous materials. The predictions from CFD are compared with empirical correlations (the Ergun and PMP equations) and with experimental data [3]. With significant geometric approximations as discussed in Section 6.1.1, the numerical simulations are within 30% of the experiments (without any experimental uncertainty estimation) and are considered reasonable. The trend in modeling errors in pressure drop relative to experimental data was the same for the CFD simulations and the empirical correlations. The likely source of this consistent error trend is a bias error in the experimental data which correlates with the face velocity. Because of geometric approximations, the CFD model is not perfect, but it does have the advantage that it can be extended to new microfibrinous materials.

CHEMICAL REACTIONS: In this phase, diffusion and surface chemical reaction are studied to understand the underlying mechanism for enhanced chemical reactivity. Two applications that were studied in this research.

Desulfurization: Results obtained in this study were presented with detailed discussion in Section 7.3.1. The reaction rate in the simulations is calibrated from experimental data for a packed bed at high face velocity by varying one adjustable parameter (i.e., pre-exponential factor). This calibrated pre-exponential factor has been used for all simulations in the desulfurization study. The effect of residence time was studied and the results (log reduction and apparent rate constant) were compared with the experimental data of Yang [4]. The results are in good agreement (within 2%) for both packed beds and microfibrinous materials. The effect of dilution with void on log reduction is studied by adding void (20-40%) to packed beds. It is observed that dilution with void has a negative effect on log reduction which is in agreement with theory. A simple parameter is defined to study the effect of clustering. The clustering parameter (P_c) is varied between 0 and 1 and the effect of clustering on log reduction has been studied. It has been observed that due to high mass diffusivity, clustering has no effect on log reduction for desulfurization. The effect of fiber size is studied by varying the fiber diameter and maintaining the rest of the geometric properties as constant. The diameter of fibers varied from 2-8 μm . It is observed that when the pressure drop is not important, microfibrinous material with smaller

size fibers will result in enhanced chemical reactivity of up to 70-80%. Finally, by changing the fiber volume loading from 1.5-4.5% and maintaining rest of the geometric properties, effect of fiber loading was analyzed. It is observed that microfibrinous materials with larger fiber volume loading (more fibers) are required to enhance the chemical reactivity by up to 60-80%.

Hexane Removal: Results obtained in this study are presented with detailed discussion in Section 7.3.2. In this study, very fast surface reactions are assumed and thus the concentration of hexane on the surface of the particle is set to zero (pure adsorption). The effect of dilution, clustering, fiber diameter, and fiber loading were studied in a similar manner as for desulfurization. The effects of dilution, fiber diameter, and fiber loading were similar to those seen for desulfurization; however, clustering has a significant effect on log reduction for hexane removal. It is observed that with maximum clustering ($P_c=1$), the logs of reduction decreased by 30% and 50% with respect to packed beds for frozen beds with 40% and 20% volume loading. This significant effect of clustering led us to study the effect of fibers on microfibrinous material with clustering. In this study, fibers were added to clustered bed. It was observed that fibers break up clustering and obtained nearly equal conversion when compared to the corresponding microfibrinous material without clustering.

PROPOSAL OF DESIGN SPACE: The ultimate goal of this research is to identify promising new material designs. In order to identify such a design space, the ratio

of the log reduction to the pressure drop for a fixed amount of catalyst is used. This ratio is compared to different materials that are used in the study of fiber loading and fiber diameter for both gas phase application. For both applications, it is observed that the microfibrous material with fewer (lower fiber volume loading), large (bigger fiber diameter) fibers showed the enhanced chemical reactivity with optimum pressure drop. If pressure drop is not important, then the material would require many (high fiber volume loading), smaller (lower fiber diameter) fibers for enhanced reactivity. The results of this research show a factor of eight and six increase in the logs of reduction of H₂S and hexane per pressure drop for 8 micron diameter fibers at 3.0% fiber loading and with 80% total void. Thus, CFD has been used as a tool to design new microfibrous materials and the proposed design criteria for microfibrous materials with enhanced chemical reactivity with optimum pressure drop points towards fewer, larger diameter fibers.

BIBLIOGRAPHY

- [1] H. S. Fogler. *Elements of Chemical Reaction Engineering*. Prentice-Hall of India Pvt. Ltd., second edition, 2001. ISBN 81-203-075-3.
- [2] R. L. Panton. *Incompressible Flow*. John Wiley and Sons, Inc., second edition, 1995. ISBN 0-471-59358-3.
- [3] D. R. Cahela and B. J. Tatarchuk. Permeability of sintered microfibrinous composites for heterogeneous catalysis and other chemical processing opportunities. *Catalysis Today*, 69:33–39, 2001.
- [4] H. Yang. *Gas Phase Desulfurization Using Regenerable Microfibrinous Entrapped Metal Oxide Based Sorbent for Logistic PEM Fuel Cell Applications*. Dissertation, Auburn University, Auburn, AL - 36849, 2007.
- [5] G. Karniadakis, A. Beskok, and N. Aluru. *Microflows and Nanoflows: Fundamentals and Simulation*. Springer-Verlag, New York, second edition, 2005.
- [6] J. M. Thomas. *Principles and Practice of Heterogeneous Catalysis*. VCH Publishers Inc, New York, 1997.

- [7] B. J. Tatarchuk, M. R. Rose, A. Krishnagopalan, J. N. Zabasajja, and D. Kohler. Mixed fiber composite structures high surface area-high conductivity mixtures. US *Patent*, 5 080 963, 1992.
- [8] B. J. Tatarchuk, M. R. Rose, and A. Krishnagopalan. Mixed fiber composite structures. US *Patent*, 5 102 745, 1992.
- [9] B. J. Tatarchuk, M. R. Rose, A. Krishnagopalan, J. N. Zabasajja, and D. Kohler. Preparation of mixed fiber composite structures. US *Patent*, 5 304 330, 1994.
- [10] B. K. Chang, Y. Lu, and B. J. Tatarchuk. Microfibrous entrapment of small catalyst or sorbent particulates for high contacting-efficiency removal of trace contaminants including CO and H₂S from practical reformates for PEM H₂O₂ fuel cells. *Chemical Engineering Journal*, 115(3):195–202, June 2006.
- [11] B. K. Chang, Y. Lu, H. Y. Yang, and B. J. Tatarchuk. Facile regeneration vitreous microfibrous entrapped supported ZnO sorbent with high contacting efficiency for bulk H₂S removal from reformat streams in fuel cell applications. *Journal of Materials Engineering and Performance*, 15(4):439–441, 2006.
- [12] Y. Lu, N. Sathitsuksanoh, H. Y. Yang, B. K. Chang, A. P. Queen, and B. J. Tatarchuk. Microfibrous entrapped supported-ZnO sorbents with high contacting efficiency for trace H₂S removal in PEMFC applications. *ACS Symposium*

- Series: Microreactor Technology and Process Intensification*, 914:406–422, 2005.
- [13] M. W. Meffert. *Preparation and Characterization of Sintered Metal Microfiber-based Composite Materials for Heterogeneous Catalyst Applications*. Dissertation, Auburn University, Auburn, AL - 36849, 1998.
- [14] B. K. Chang, Y. Lu, and B. J. Tatarchuk. Microfibrous entrapment of small catalyst or sorbent particulates for high contacting-efficiency removal of trace CO from practical reformates for PEM H₂O₂ fuel cells. *Journal of Materials Engineering and Performance*, 15(4):453–456, 2006.
- [15] A. P. Queen. High efficiency adsorption filters via packed bed + polishing sorbent architectures for regenerable collective protection equipment. Thesis, Auburn University, Auburn, AL - 36849, 2005.
- [16] R. R. Kalluri, D. R. Cahela, and B. J. Tatarchuk. Microfibrous entrapped small particle adsorbents for high efficiency heterogeneous contacting. *Submitted*, 2006.
- [17] D. K. Harris, D. R. Cahela, and B. J. Tatarchuk. Wet layup and sintering of metal-containing microfibrous composites for chemical process opportunities. *Composites: Part A-Applied Science and Manufacturing*, 32(8):1117–1126, 2001.

- [18] A. H. Epstein and S. D. Senturia. Microengineering: Macro power from micro machinery. *Science*, 276:1211, 1997.
- [19] P.J. French. MEMS/MOEMS technology capabilities and trends. *MEMS and MOEMS Technology and Applications*, pages 1–40, 2000.
- [20] W. Ehrfeld and U. Ehrfeld. Progress and profit through micro technologies, commercial applications of MEMS/MOEMS. *MEMS Components and Applications for Industry, Automobiles, Aerospace, and Communication*, pages xi–xx, 2001.
- [21] C. Hagleitner, A. Hierlemann, D. Lange, A. Kummer, N. Kerness, O.Brand, and H. Baltes. Smart single-chip gas sensor microsystem. *Nature*, 414(6861): 293–296, 1999.
- [22] E. S. Kolesar and R. R. Restin. Review and summary of a silicon micromachined gas chromatography system. *IEEE Transactions on Components Packaging and Manufacturing Technology Part B-Advanced Packaging*, 21(4):424–328, 1998.
- [23] L. Lofdahl and M. Gad el Hak. MEMS applications in turbulence and flow control. *Progress in Aerospace Sciences*, 35(2):101–203, 1999.
- [24] M. Gad el Hak. Flow control: The future. *Journal of Aircraft*, 38(3):402–418, 1999.

- [25] J. Choi, W.P. Jeon, and H. Choi. Control of flow around an airfoil using piezoceramic actuators. *AIAA Journal*, 40(5):1008–1010, 2002.
- [26] M. McNeely. Microturbine designed for mechanical drive applications. *Diesel Progress North American Edition*, 64(5):38–40, 1998.
- [27] S. Blankinship. New miniturbine takes aim at microturbine market. *Power Engineering*, 105(10):77–77, 2001.
- [28] C. M. Ho and Y. C. Tai. Micro-electro-mechanical systems (MEMS) and fluid flows. *Annual Review of Fluid Mechanics*, 30:579–612, 1998.
- [29] M. Gad el Hak. The fluid mechanics of microdevices - the freeman scholar lecture. *Journal of Fluids Engineering*, 121:5–33, 1999.
- [30] J. Choi, W.P. Jeon, and H. Choi. Physical challenges and simulation of micro fluidic transport. *AIAA Conference*, 2001-0718.
- [31] G. E. Karniadakis and A. Beskok. *Micro Flows: Fundamentals and Simulation*. Springer-Verlag New York, Inc., 2002.
- [32] K. C. Pong, C. M. Ho, J. Liu, and Y. C. Tai. Non-linear pressure distribution in uniform microchannels. *ASME Winter Annual Meeting: Application of Microfabrication to Fluid Mechanics*, pages 51–56, 1994.

- [33] E.B. Arkilic. *Measurement of the Mass Flow and Tangential Momentum Accommodation Coefficient in Silicon Micromachined Channels*. Ph.d. dissertation, MIT, 1997.
- [34] L.S. Fan, Y.C. Tai, and R.S. Muller. IC-processed electrostatic micromotors. *Tech. Dig. Int. Electron Dev. Meet. (IEDM)*, pages 666–669, 1988.
- [35] H. K. Versteeg and W. Malalasekera. *An Introduction to Computational Fluid Dynamics*. Addison-Wesley Pub. Co., 1996.
- [36] J. N. and D. K. Gartling. *The Finite Element Method in Heat Transfer and Fluid Dynamics*. CRC Press, 1994.
- [37] G. E. Karniadakis and S. J. Sherwin. *Spectral/HP Element Methods for CFD*. Oxford University Press, 1999.
- [38] A. Beskok. *Simulations and Models for Gas Flows in Microgeometries*. Ph.d. dissertation, Princeton University, 1996.
- [39] A. Beskok and G. E. Karniadakis. A model for flows in channels, pipes, and ducts at micro and nano scales. *Microscale Thermophysical Engineering*, 3:43–77, 1999.
- [40] K. Hennighausen. *Fluid Mechanics of Microscale Flight*. Ph.d. dissertation, University of Minnesota, 2001.

- [41] *Numerical Simulation of Low Reynolds Number Slip Flow Past a Confined Microsphere*, Canada, 20-25 July 2002. 23rd International Symposium on Rarefied Gas Dynamics.
- [42] M. Sahimi. *Applications of Percolation Theory*. (Taylor & Francis, 1994.
- [43] P. M. Adler. *Porous Media: Geometry and Transport*. Butterworth-Heinemann, 1992.
- [44] D. Ping, F. Shi-De, and Z. Ying. Numerical analysis of fluid flow through a cylinder array using a lattice boltzmann model. *Chinese Physics*, 13(4):434–440, 2004.
- [45] F. A. L. Dullien. *Porous Media—Fluid Transport and Pore Structure*. Academic, 1979.
- [46] D. R. Koch and A. J. C. Ladd. Moderate reynolds number flows through periodic and random arrays of aligned cylinders,. *Journal of Fluid Mechanics*, 349:31–66, 1997.
- [47] D. A. Edwards, M. Shapiro, P. Bar-Yoseph, and M. Shapira. The influence of reynolds number upon the apparent permeability of spatially periodic arrays of cylinders. *Physics of Fluids*, 2(1):45–55, 1990.

- [48] S. Ergun. Fluid flow through packed columns. *Chemical Engineering Progress*, 48(2):89–94, February 1952.
- [49] T. D. Papathanasiou, B. Markicevic, and E. D. Dendy. Computational evaluation of the ergun and forchheimer equations for fibrous porous media. *Physics of Fluids*, 13(10):2795–2805, 1990.
- [50] J. S. Andrade, U. M. S. Costa, M. P. Almeida, and H. A. Makse H. E. Stanley. Inertial effect on fluid flow through disordered porous media. *Physical Review Letters*, 82(26):5249–5252, 1999.
- [51] R. E. Hicks. Pressure drop in packed beds of spheres. *Industrial and Engineering Chemistry Fundamentals*, 9(3):500–502, 1970.
- [52] J. C. Tannehill, D. A. Anderson, and R. H. Pletcher. *Computational Fluid Mechanics and Heat Transfer*. Taylor and Francis, second edition, 2004. ISBN 1-56032-046-X.
- [53] *Fluent User’s Guide*. Fluent, 6.3 edition, 2006. Vols. 1-3.
- [54] J. D. Anderson. *Computational Fluid Dynamics: The Basics with Applications*. McGraw Hill, Inc., 1995. ISBN 0-07-001685-2.
- [55] C. E. Kolb, D. R. Worsnop, M. S. Zahniser, P. Davidovits, L. F. Keyser, M. T. Leu, M. J. Molina, D. R. Hanson, A. R. Ravishankara, L. R. Williams, and

- M. A. Tolbert. Laboratory studies of atmospheric heterogeneous chemistry. *Adv. Ser. Phys. Chem*, 3:771, 1995.
- [56] O. Levenspiel. *Chemical Reaction Engineering*. John Wiley and Sons, Inc., 1972. ISBN 0-471-53016-6.
- [57] G. F. Froment and K. B. Bischoff. *Chemical Reactor Analysis and Design*. John Wiley and Sons, 1979.
- [58] J. L Williams. Monolith structures, materials, properties and uses. *Catalysis Today*, 69:3–9, 2001.
- [59] D. Kunii and O. Levenspiel. *Fluidization Engineering*. Butterworth and Heine-
mann, second edition, 1991. ISBN 0-409-90233-0.
- [60] C. S. Song and X. L. Ma. Ultra-deep desulfurization of liquid hydrocarbon
fuels: Chemistry and process. *Journal of Green Energy*, 1:167–191, 2004.
- [61] A. A. Vargas-Tah, R. C. García, L. F. P. Archila, J. R. Solis, and A. J. Lopez.
A study on sulfur reduction in fcc gasoline using ZnMgAl spinels. *Catalysis
Today*, pages 107–108, 713–718, 2005.
- [62] R. Ben-Slimane and M. T. Hepworth. Desulfurization of hot coal-derived fuel
gases with manganese-based regenerable sorbents. *Energy and Fuels*, 8:1184–
1191, 1994.

- [63] L. D. Gasper-Galvin, A. T. Atimatay, and R. P. Gupta. Zeolite-supported metal oxide sorbents for hot gas desulfurization. *Industrial and Engineering Chemistry Research*, 37:4157–4166, 1998.
- [64] S. Lew, K. Jothimurugesan, and M. Flytzani-Stephanopoulos. High-temperature H₂S removal from fuel gases by regenerable zinc oxide-titanium dioxide sorbents. *Industrial and Engineering Chemistry Research*, 28:535–541, 1989.
- [65] T. Fukunaga, H. Katsuno, H. Matsumoto, and O. Takahashi and Y. Akai. Development of kerosene fuel processing system for PEFC. *Catalysis Today*, 84:197–203, 2003.
- [66] J. Zheng, J. J. Strohm, M. Hoehn, and C. Song. Pre-reforming of jet fuels on modified Rh/CeO₂-Al₂O₃ catalysts for solid oxide fuels cell. *ACS: Division of Petroleum Chemistry*, 49:21–24, 2004.
- [67] O. Kibazohi, S. Yun, and W. A. Anderson. Removal of hexane in biofilters packed with perlite and a peat-perlite mixture. *World Journal of Microbiology and Biotechnology*, 20:337–343, 2003.
- [68] R. Atkinson. Atmospheric chemistry of VOCs and NO_x. *Atmospheric Environment*, 34:2063–2101, 2001.

- [69] C. Y. Lu and M. Y. Wey. Simultaneous removal of VOCs and NO by activated carbon impregnated with transition metal catalysts in combustion flue gas. *Fuel Processing Technology*, 88:557–567, 2007.
- [70] S. Ahn and B. J. Tatarchuk. Fibrous metal-carbon composite structures as gas diffusion electrodes for use in alkaline electrolyte. *Journal of Applied Electrochemistry*, 27:9–17, 1997.
- [71] D. R. Cahela, B. K. Chang, M. Karanjikar, E. A. Luna, and B. J. Tatarchuk. Aiche annual meeting. In *Microfibrous and Micro-Structured Adsorbents and Catalysts Media: Enhancement in Effectiveness Caused by Static Mixing*, November 7-12 2004.
- [72] B. K. Chang and B. J. Tatarchuk. Microfibrous materials. In *AIChE Annual Meeting*. AIChE Annual Meeting, November 16-21 2003.
- [73] D. A. Kohler, J. N. Zabasajja, A. Krishnagopalan, and B. J. Tatarchuk. Metal-carbon composite materials from fiber precursors. *Journal of the Electrochemical Society*, 137(1):136–141, 1990.
- [74] Y. Lu and B. J. Tatarchuk. Microfibrous entrapped supported-ZnO sorbents with high contacting efficiency for trace H₂S removal in PEMFC applications.

In *226th ACS National Meeting*. 226th ACS National Meeting, September 7-11 2003.

- [75] C. J. Marrion, D. R. Cahela, S. Ahn, and B. J. Tatarchuk. Composite fiber structures for catalysts and electrodes. *Journal of Power Sources*, 47:297–302, 1994.
- [76] R. A. Overbeek, A. M. Khonsari, Y. F. Chang, L. L. Murrell, B. J. Tatarchuk, and M. W. Meffert. US patent. US *Patent*, 6 231 792, 2001.
- [77] B. J. Tatarchuk. Microfibrous materials. US *Patent*, 5 096 663, 1992.
- [78] M. R. Karanjikar, Y. Lu, B. K. Chang, and B. J. Tatarchuk. Logistic fuel to hydrogen: Fuel processing using microfibrous entrapped catalysts and sorbents for pem fuel cells. In *Proceeding of the 41st Power Sources Conference*. Proceeding of the 41st Power Sources Conference, June 14-17 2004.
- [79] M. R. Karanjikar. *Low Temperature Oxidation of Carbon Monoxide Using Microfibrous Entrapped Catalysts for Fire Escape Mask Application*. Dissertation, Auburn University, Auburn, AL - 36849, 2005.
- [80] S. Middleman. *An Introduction to Fluid Dynamics: Principles of Analysis and Design, Chapter 10: Flow Through Porous Media*. John Wiley and Sons, Inc., 1998.

- [81] P. C. Carman. Flow of gases through porous media. *Academic Press*, page 12, 1956.
- [82] J. L. Fowler and R. L. Hertel. Flow of gas through porous media. *Journal of Applied Physics*, 11:496–502, 1940.
- [83] C. J. Roy. Review of code and solution verification procedures for computational simulation. *Journal of Computational Physics*, 205(1):131–156, 2005.
- [84] P. J. Roache. *Fundamentals of Computational Fluid Dynamics*. HERmosa Publishers, 1998.
- [85] P. R. Westmoreland, J. B. Gibson, and D. P. Harrison. Comparative kinetics of high-temperature reaction between H₂S and selected metal oxides. *Environmental Science & Technology*, 11(5):488–491, 1977.
- [86] P. N. Dwivedi and S. N. Upadhyay. Particle-fluid mass transfer in fixed and fluidized beds. *I & EC Proc. Des. Dev.*, 16(2):157–165, 1977.
- [87] N. T. Nguyen and S. T. Wereley. *Fundamentals And Applications of Microfluidics*. Artech House, 2002. ISBN 1-58053-343-4.
- [88] E. S. Oran and J. P. Boris. *Numerical Simulation of Reactive Flow*. Elsevier, 1987. ISBN 0-444-01251-6.

- [89] T. J. Chung. *Computational Fluid Dynamics*. Cambridge University Press, first edition, 2002. ISBN 0-521-54082-8.
- [90] R. W. Fox and A. T. McDonald. *Introduction to Fluid Mechanics*. John Wiley and Sons, Inc., fifth edition, 1998. ISBN 9971-51-355-2.
- [91] M. J. McNenly, M. A. Gallis, and I. D. Boyd. Empirical slip and viscosity model performance for microscale gas flow. *International Journal for Numerical Methods in Fluids*, 49:1169–1191, 2005.
- [92] M. J. McNenly, M. A. Gallis, and I. D. Boyd. Slip model performance for microscale gas flows. In *36th AIAA Thermophysics Conference*, number AIAA-2003-4050 in AIAA. 36th AIAA Thermophysics Conference, 2003.
- [93] S. D. Senturia. *Microsystem Design*. Kluwer Academic Publishers, 2001.
- [94] J. C. Harley, Y. Huang, H. H. Bau, and J. N. Zemel. Gas flow in micro-channels. *Journal of Fluid Mechanics*, 284:257–274, 1995.
- [95] R. Bayt. *Analysis, Fabrication and Testing of a MEMS-based Micro Propulsion System*. Ph.d. dissertation, MIT, 1999.
- [96] D. M. Freeman, A. J. Aranyosi, M. J. Gordon, and S. S. Hong. Multidimensional motion analysis of MEMS using computer microvision. *Solid-State Sensor and Actuator Workshop*, pages 150–155, 1998.

- [97] N. R. Aluru and G. Li. Finite cloud method: A true meshless technique based on reproducing kernel approximation. *International Journal for Numerical Methods in Engineering*, 50(10):2373–2410, 2001.
- [98] R. S. Myong. A computational method for euŠs generalized hydrodynamic equations of rarefied and microscale gasdynamics. *Journal of Computational Physics*, 168:47–72, 2001.
- [99] X. Wang. *A Fast 3-D Fluid Simulation Program for Micro-Electro-Mechanical Systems*. Ph.d. dissertation, MIT, 2002.
- [100] G. A. Bird. *Molecular Gas Dynamics and the Direct Simulation of Gas Flows*. Oxford Science Publications, 1994.
- [101] W. W. Liou and Y. Fang. The development of a burnett equations solver for microfluid flow and heat transfer simulations. *AIAA Conference*, 2001.
- [102] J. Fan and C. Shen. Statistical simulation of low-speed unidirectional flows in transition regime. *Proceedings of the 21th International Symposium on Rarefied Gas Dynamics*, 168:245–252, 1999.
- [103] J. Fan and C. Shen. Statistical simulation of low-speed rarefied gas flows. *Journal of Computational Physics*, 167:393–412, 2001.

- [104] J. Fan, I. D. Boyd, C. Cai, K. Hennighausen, and G. V. Candler. Computation of rarefied flows around a NACA 0012 airfoil. *AIAA Journal*, 39(4):618–625, 2001.
- [105] J. S. Andrade, M. P. Almeida, J. M Filho, S. Havlin and B. Suki, and H. E. Stanley. Fluid flow through porous media: The role of stagnant zones. *Physical Review Letters*, 79(20):3901–3904, 1997.

APPENDIX A

VERIFICATION OF VELOCITY SLIP BOUNDARY CONDITION

The commercial CFD code Fluent is used for the current simulations [53]. The purpose of this section is to verify the formulation of slip boundary condition in Fluent. 2D Poiseuille flow (pressure driven flow) is used as a test case and a schematic is given in Figure A.1 showing the boundary conditions. The top and bottom bound-

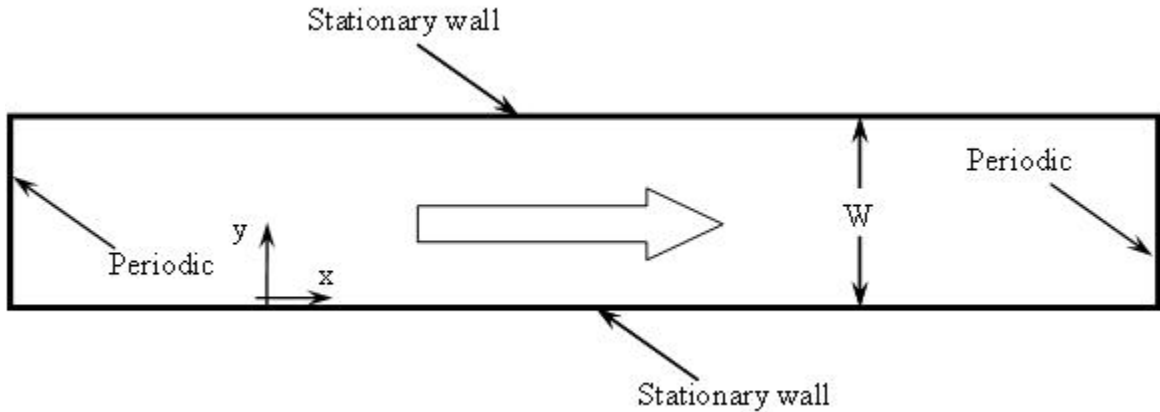


Figure A.1: Illustration of test case geometry for Poiseuille flow

aries are stationary walls, while the left and right sides are linked together with the periodic boundary condition which matches velocity components but allows a pressure gradient. Maxwell's first-order velocity-slip boundary condition (Eq. A.1) as

given by [5] is applied to the stationary walls.

$$U_s - U_w = \frac{2 - \sigma_v}{\sigma_v} \lambda \frac{\partial U}{\partial n} \quad (\text{A.1})$$

Velocity profiles are available for this type of benchmark solution from the simulation by [91, 92] and an analytic solution also exists. Velocity profiles obtained from CFD simulations using Fluent are compared to the profiles obtained by [91, 92] and to the analytic solution. Air is used as a working fluid which enters the domain with a flow velocity of 20 m/s. The temperature of the walls is fixed at 273 K. Several tests are conducted by varying the Knudsen number from 0.01 to 1.0. The tangential momentum accommodation coefficient (σ_v), defined as the fraction of tangential momentum the gas molecules exchange with the surfaces, is taken as unity which means the molecules are reflected from the wall with zero average tangential velocity, or diffuse reflection [5]. The analytic solution for velocity profiles in Poiseuille flow using the first-order velocity-slip boundary condition was derived in [5] and is given by

$$U(x, y) = -\frac{dp}{dx} \frac{W^2}{2\mu} \left[-\left(\frac{y}{W}\right)^2 + \left(\frac{y}{W}\right) + C_1 Kn + 2C_2 Kn^2 \right] \quad (\text{A.2})$$

For Maxwell's first-order velocity-slip boundary condition, C_1 and C_2 are equal to 1 and 0, respectively. The results obtained from the CFD simulations are compared

with literature and the analytic solution for Knudsen numbers 0.01, 0.1, 1.0 and is shown in Figures A.2, A.3, A.4.

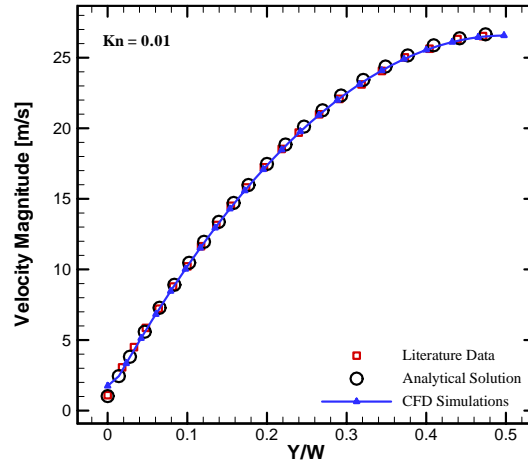


Figure A.2: Comparison of velocity profiles for Poiseuille flow at $Kn=0.01$

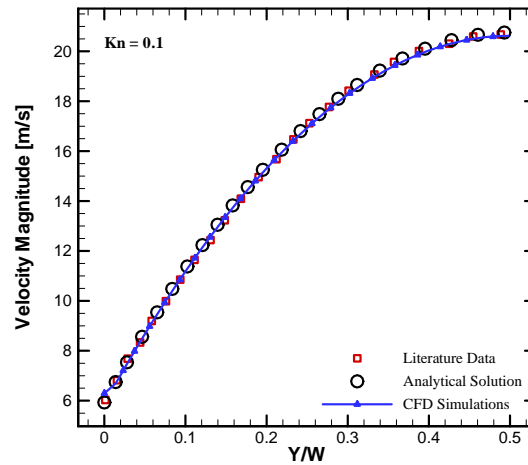


Figure A.3: Comparison of velocity profiles for Poiseuille flow at $Kn=0.1$

The distance measured from the bottom wall is non-dimensionalized with the total distance between the two stationary walls (W). Velocities are plotted against

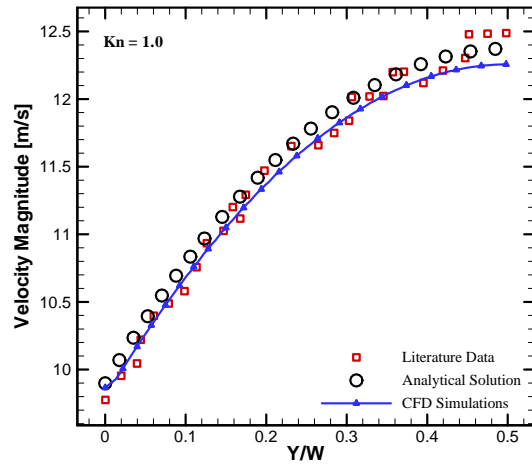


Figure A.4: Comparison of velocity profiles for Poiseuille flow at $Kn=1.0$

the non-dimensional height of the domain for different Knudsen numbers in Figures A.2, A.3, A.4. The results obtained from CFD simulations are in good agreement with both the analytic solution and the results from [91, 92] for the three Knudsen numbers tested. Figures A.2, A.3, A.4 also show the increase in the velocity at the wall with the increase in the Knudsen number. For Knudsen numbers of 0.01, 0.1, and 1.0, the wall velocities are approximately 1, 6, and 10 m/s, respectively.

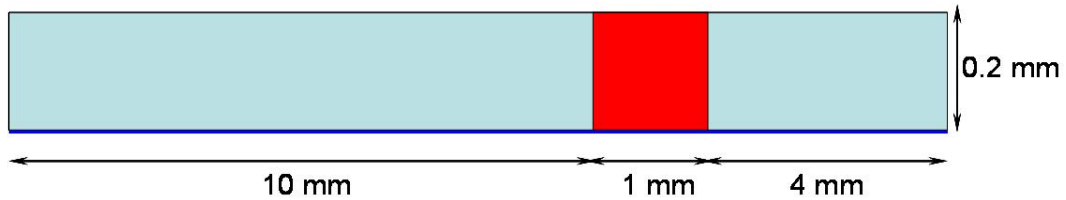
APPENDIX B

EFFECT OF INLET DIFFUSION

A study was done to analyze the effect of inlet diffusion on concentration profiles in the reactor. This study was done with two type of reactors: (1) 2D rectangular channel reactor and (2) 2D packed bed reactor.

B.1 Rectangular Channel Reactor

Case 1: 2D Rectangular Channel with Buffer



Case 2: 2D Rectangular Channel without Buffer

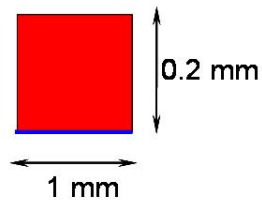


Figure B.1: Schematic geometry of the rectangular channel reactor (red denotes reactive region)

In this case the reactor is a simple 2D rectangular channel. An inert buffer is added at the inlet and outlet to study the effect of the buffer along with effect of inlet

diffusion. Figure B.1 shows the dimensions of the reactor and the buffer used at inlet and outlet.

FLUENT [53] is used to solve the governing equations with appropriate boundary conditions. The bottom is defined as symmetry. The top wall in the reactor (red colored zone) is defined as a reacting wall. Velocity and the inlet concentration of the challenge gas are defined at the inlet.

In this study, the mass diffusivity is varied between 0.083 (hexane diffusivity) and $2.8 \text{ cm}^2/\text{s}$ (H_2S diffusivity). Face velocities are varied between 1 and 100 cm/s .

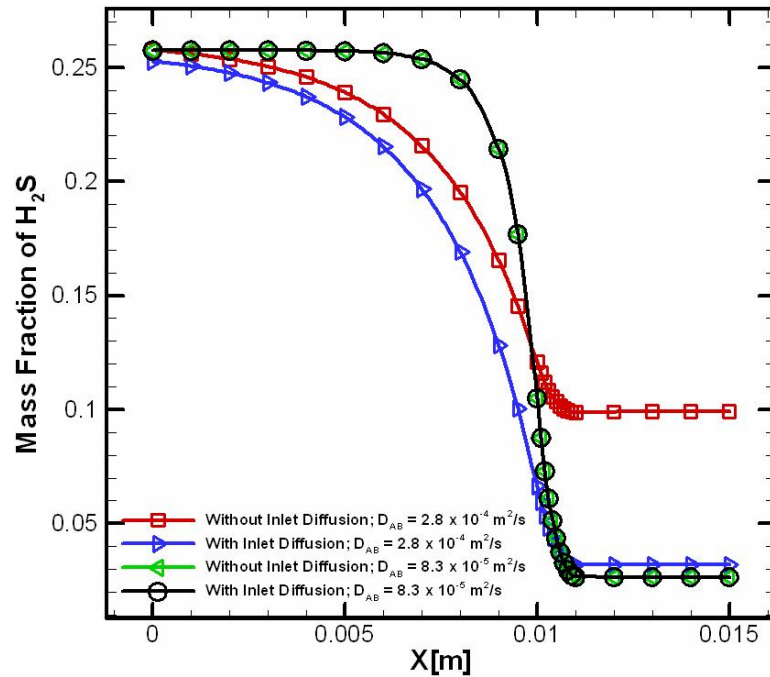


Figure B.2: Effect of inlet diffusion for different mass diffusivities at $V_f = 10 \text{ cm}/\text{s}$

Figure B.2 shows the effect of inlet diffusion by plotting concentration of H_2S on Y-axis (log scale) versus X. It is observed that inlet diffusion has no effect on the concentration profiles for low diffusivity ($0.083 \text{ cm}^2/\text{s}$). For the gas with high diffusivity, the concentration profiles are different because of insufficient inlet buffer length. Thus, if the reactor has a long entrance inlet, the concentration profiles will match in the case of high diffusivity.

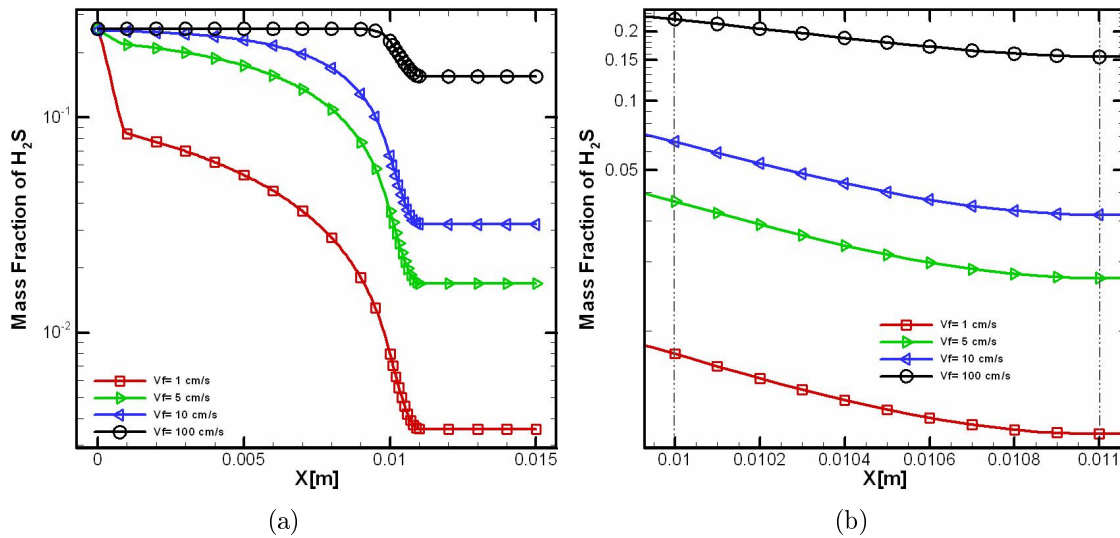


Figure B.3: Effect of inlet diffusivity at different velocities: (a) entire domain (b) closeup of the reaction zone

Figure B.3 shows the concentration profiles along the length of the domain for different face velocities. It is observed that the current length of the inlet buffer is not sufficient for low velocity flows.

Contours of the concentration of H_2S are shown in Figure B.4. It is observed that as the velocity of the flow decreases the concentration gradient at the inlet increases which explains the need for additional buffer length at the inlet.

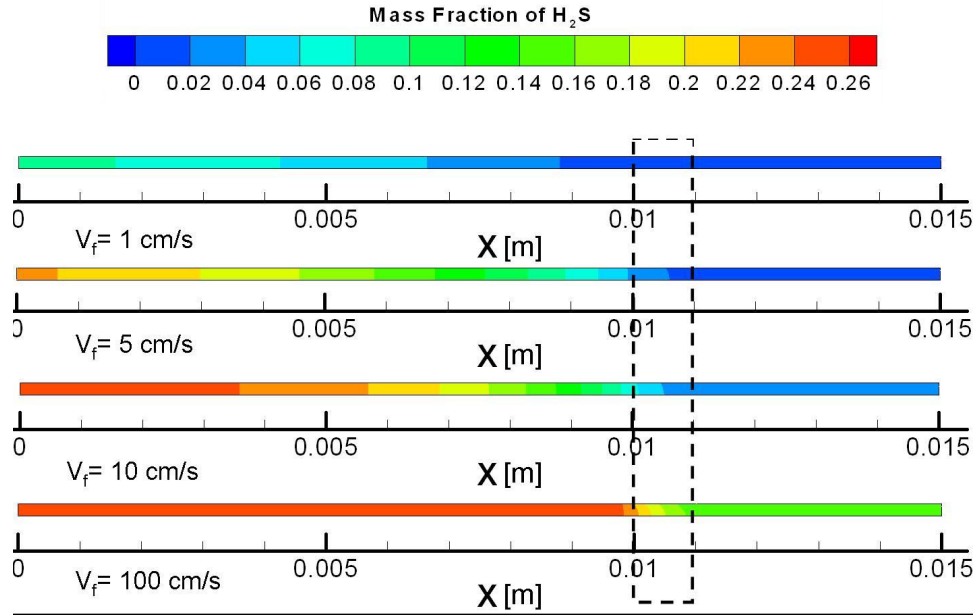


Figure B.4: Concentration contours in the rectangular reactor with buffer at different velocities

In Figure B.3(a), the buffer length is exactly sufficient for the case with face velocity of 10 cm/s. If we increase the inlet buffer by a factor of 10 then it will be sufficient even at low velocities; however, adding more buffer increase the computational time.

In order to overcome the problem of increasing inlet buffer length at low velocities, we enable inlet diffusion. Figure B.5 shows that when inlet diffusion is turned on and

the inlet buffer is removed for the case with face velocity of 10 cm/s, the concentration profile in the reactor zone matched with the case with appropriate inlet buffer.

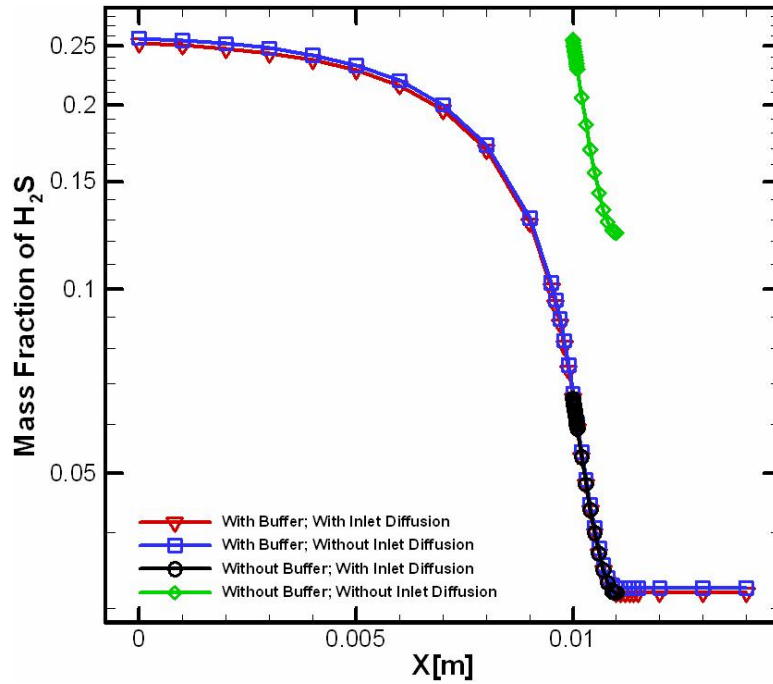


Figure B.5: Effect of inlet buffer on the concentration profiles ; $V_f=10$ cm/s

From this study, when the inlet is close to the reactor (i.e., no buffer case), enabling inlet diffusion effectively assumes a virtual inlet far away from the reactor and agrees well with the long entrance length case. In this work, inlet diffusion has been enabled and small inert buffer is added at the entrance and exit of the reacting zone to minimize the end effects.

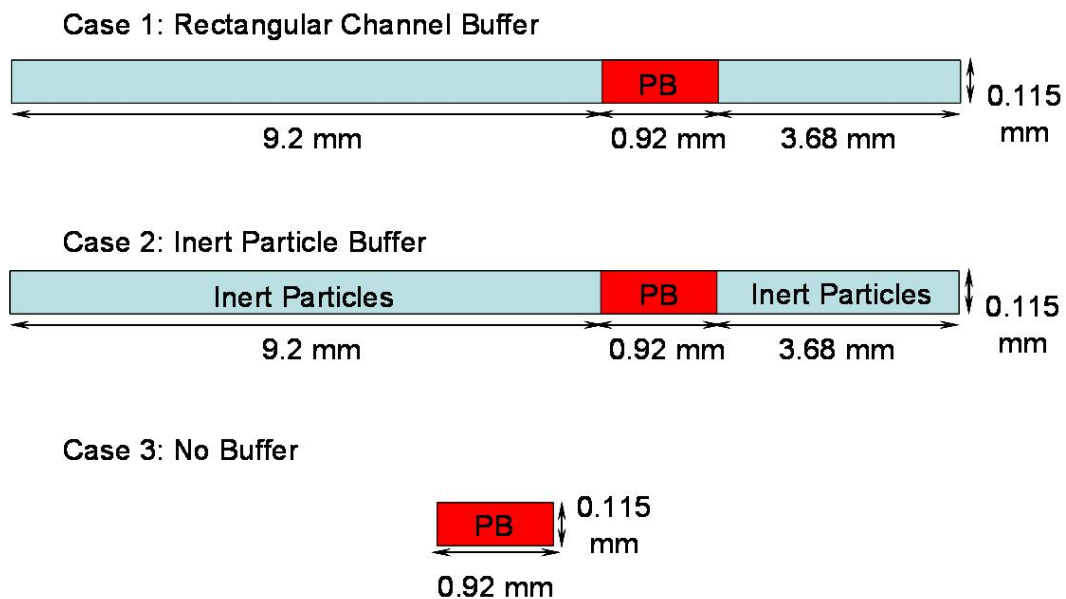


Figure B.6: Schematic geometry of the packed bed reactor (red denotes reactive region)

B.2 Packed Bed Reactor

Packed bed reactors are commonly used in the chemical processing industries. Here we study the effect of inlet diffusion on concentration profiles in packed bed reactors. Similar to the study made on rectangular channels, an inert buffer is added at the inlet and outlet; however, in this study the effect of the type of inlet buffer is also studied. The schematic of the geometries used in this study are shown in Figure B.6.

In case 1, a long rectangular inert buffer is added at the inlet and outlet of the packed bed reactor zone (red colored zone). In case 2, the rectangular inert buffer

used in case 1 is filled with inert particles (i.e., a packed bed buffer). In case 3, only a packed bed reactor is used without any inert buffer.

A study was performed by enabling and disabling inlet diffusion for case 1 and 2. The concentration profiles for both cases are shown in Figure B.7. It is observed that with the inert particles in the buffer, a smaller buffer is required at the inlet compared to rectangular channel buffer.

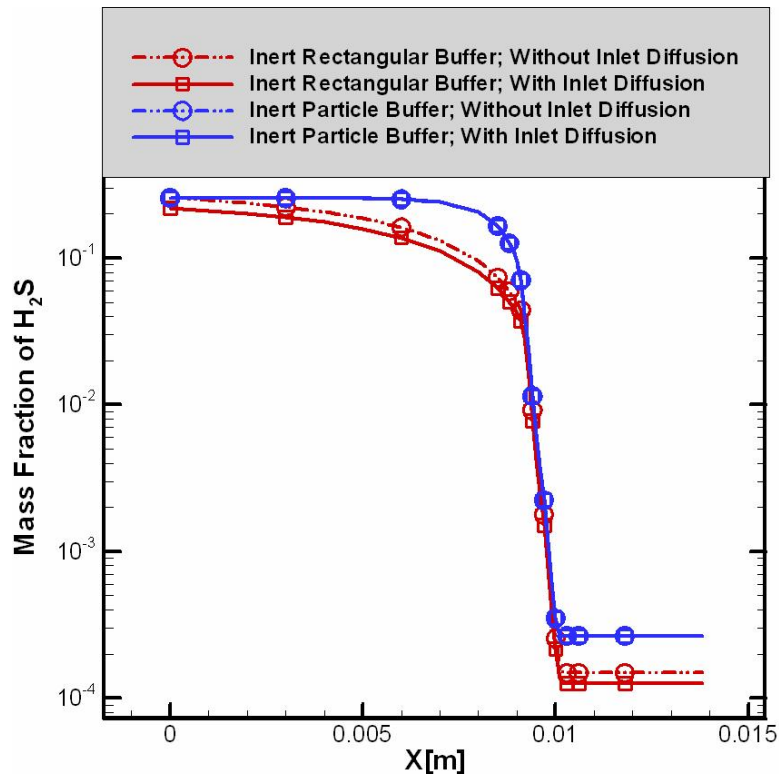


Figure B.7: Effect of type of inlet buffer on the concentration profiles

A similar analysis to that done in rectangular channel reactors is performed in packed bed reactors. Concentration profiles were examined for the cases with and

without particle buffer and with and without inlet diffusion in Figure B.8. It is observed that by enabling inlet diffusion, we can eliminate the buffer and thus reduce computational time.

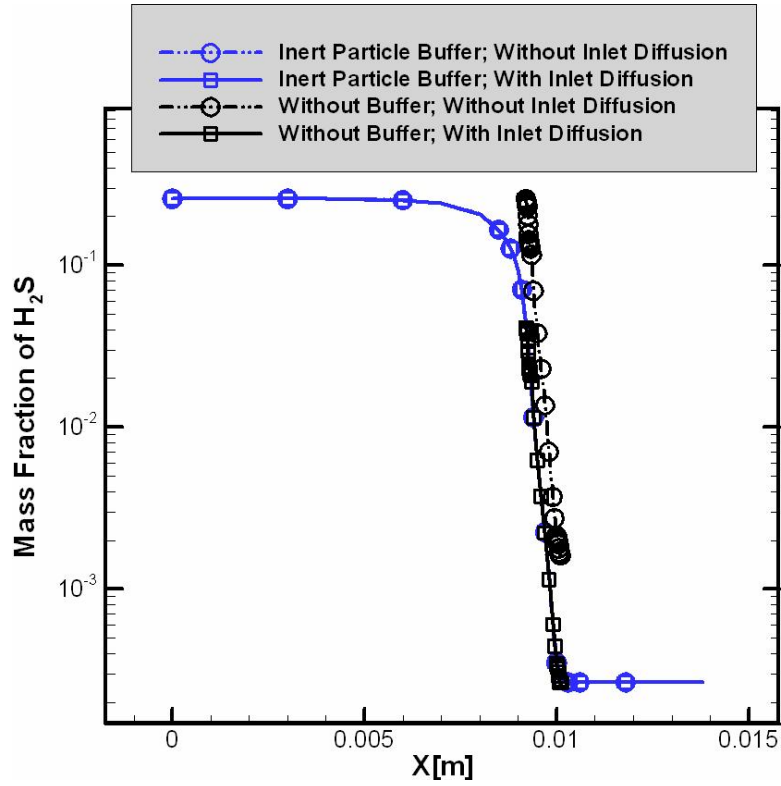


Figure B.8: Effect of inlet buffer on the concentration profiles in packed bed reactors

Finally, in this study it is concluded if the inert buffer is not used, then enabling inlet diffusion gives the correct results while disabling inlet diffusion produces spurious results. From our observations, the implementation of inlet diffusion in FLUENT [53] is backwards (i.e., turning off the inlet diffusion option in Fluent actually enables inlet diffusion).

APPENDIX C

UNIFORM GRID REFINEMENT FOR GRID CONVERGENCE

In order to perform grid convergence studies using Richardson extrapolation, the grid should be refined uniformly in all directions. This section explains the way to refine or coarsen the grid uniformly in all directions using the Gambit grid generator and also explains how to use Tecplot to help verify whether the grid is refined uniformly in all directions. This section has been divided into two parts: (1) volumetric grid refinement and (2) boundary layer grid refinement.

VOLUMETRIC GRID REFINEMENT: This section deals with refining grid in the volume. A volumetric mesh can be created in three ways:

1. Mesh all edges using appropriate element size and then mesh the volume.
2. Mesh all faces using appropriate element size and then mesh the volume.
3. Mesh the volume using appropriate element size.

Starting with a coarse grid, the fine grid can be generated just by changing the element size using

$$\left\{ \begin{array}{l} \text{Element size} \\ \text{of fine grid} \end{array} \right\} = \left\{ \begin{array}{l} \text{Refinement} \\ \text{factor} \end{array} \right\} \times \left\{ \begin{array}{l} \text{Element size} \\ \text{of coarse grid} \end{array} \right\}.$$

BOUNDARY LAYER GRID REFINEMENT: This section explains the way to refine a boundary layer mesh in order to get uniform refinement. The parameters involved in defining a boundary layer mesh are first row height (a), growth factor (b/a), total number of rows (n), and total height of the boundary layer (H). Let the refinement factor be r_n/r_d , i.e., if the refinement factor is 1.5, $r_n=3$ and $r_d=2$, and the subscripts f and c represent parameters for the fine and coarse grid, respectively. Table C.1 shows the parameters used in this boundary layer grid refinement. One thing to be remembered while refining or coarsening a boundary layer grid is that the total height of the boundary layer must be maintained constant.

Table C.1: Parameters used in boundary layer grid refinement

Parameter	Fine grid	Coarse grid
First row height	a_f	a_c
Growth factor	$\left(\frac{b}{a}\right)_f$	$\left(\frac{b}{a}\right)_c$
Total number of rows	n_f	n_c
Total height	H_f	H_c

Coarsening a Boundary Layer Grid: Let us first start with a fine grid and then calculate the parameters for the coarse grid. Since the total height of the boundary layer must be constant, we must have $H_f = H_c$.

Calculation of growth factor:

$$\left(\frac{b}{a}\right)_c = \left(\frac{b}{a}\right)_f \times \left(\frac{r_n}{r_d}\right)$$

Calculation of first row height:

$$a_c = \frac{a_f \sum_{i=1}^{r_n} \left(\frac{b}{a}\right)_f^{i-1}}{\sum_{i=1}^{r_d} \left(\frac{b}{a}\right)_c^{i-1}}$$

Calculation of total number of rows:

$$n_c = n_f \times \left(\frac{r_n}{r_d}\right)$$

Refining a Boundary Layer Grid: Let us start with a coarse grid and then calculate the parameters for the fine grid. Since the total height of the boundary layer must be constant, we must have $H_f = H_c$.

Calculation of growth factor:

$$\left(\frac{b}{a}\right)_f = \left(\frac{b}{a}\right)_c \times \left(\frac{r_d}{r_n}\right)$$

Calculation of first row height:

$$a_f = \frac{a_c \sum_{i=1}^{r_d} \left(\frac{b}{a} \Big|_c \right)^{i-1}}{\sum_{i=1}^{r_n} \left(\frac{b}{a} \Big|_f \right)^{i-1}}$$

Calculation of total number of rows:

$$n_f = n_c \times \left(\frac{r_d}{r_n} \right)$$

VERIFYING UNIFORM REFINEMENT: Once two grid levels (coarse and fine) are generated, it is important to check whether we obtained uniform refinement or not. In order to verify this, the *Tecplot CFD Analyzer* has been used. The following procedure is adopted to verify the uniform refinement.

1. Load coarse grid in Tecplot using *File* → *load data files* → *fluent data loader*.
2. Calculate cell volume using *Analyze* → *calculate variables*.
3. Write data into a file using *File* → *write data files*.
4. Repeat steps 1-3 for fine grid.
5. Load files of coarse grid and fine grid with cell volumes.

6. Interpolate the cell volume of fine grid onto the coarse grid using *Data* \rightarrow *interpolate*.
7. Write data on the coarse grid data with interpolated cell volumes from the fine grid.
8. Load files for coarse grid with coarse grid cell volume and interpolated fine grid cell volumes.
9. Define a new variable which is the cube root of the ratio of cell volume of the coarse grid to the interpolated cell volume of the fine grid using *Data* \rightarrow *alter* \rightarrow *specify equations*. This ratio is the actual locally varying grid refinement factor.
10. Plot the contours of the new variable at different sections and in different directions. If the ratio is approximately equal to the refinement factor, then the grids are said to be uniformly refined in terms of the cell volumes.

Above steps were followed to verify whether the refinement was uniform or not. Figure C.1 shows the contours of the cube root of the ratio of cell volume of the coarse grid to the interpolated cell volume of the fine grid in all three directions. The actual refinement used to generate fine from coarse grid is 1.5. It is observed that the grid refinement achieved is nearly equal to 1.5 (generally between 1.45 and 1.55) which confirms approximately uniform grid refinement.

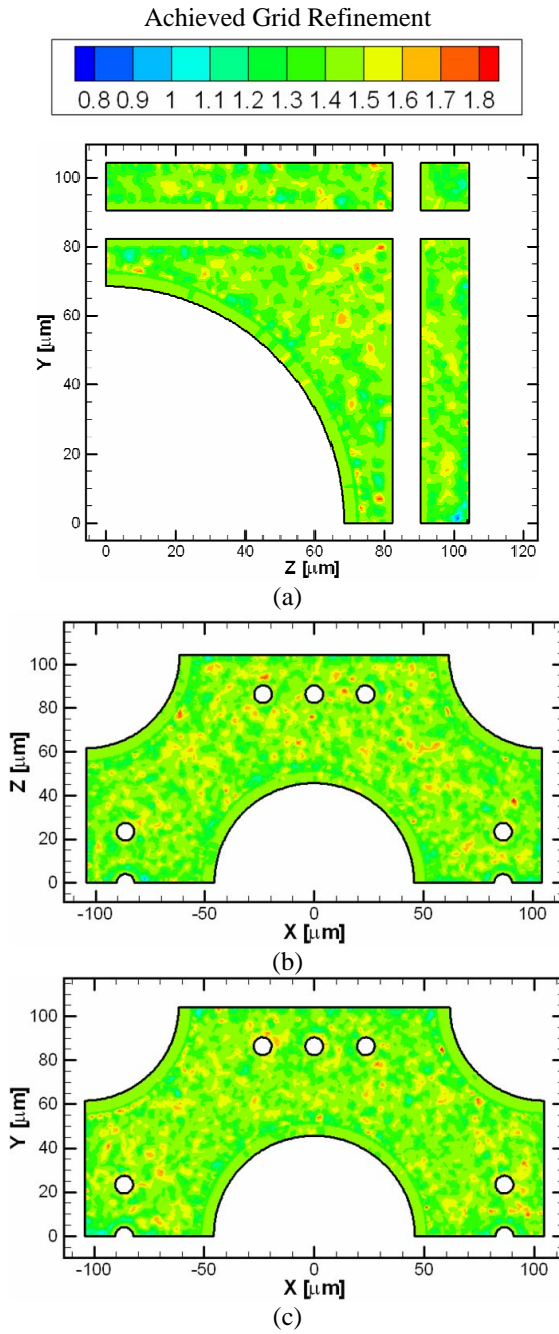


Figure C.1: Achieved grid refinement in all three directions (a) constant X, (b) constant Y, and (c) constant Z

APPENDIX D

FLUENT INPUT FILES AND USER-DEFINED FUNCTIONS

D.1 Input Files

D.1.1 Pressure Drop

The journal file used to run cfd simulation to predict pressure drop in BATCH mode

using FLUENT is:

```
; READ CASE FILE
rc Eps-0.41-Coarse-Vf59
;AUTO-SAVING CASE AND DATA FILES
/file/autosave/case-frequency 500
/file/autosave/data-frequency 500
/file/autosave/overwrite-existing-files yes
/file/autosave/max-files 1
/file/autosave/root-name/Eps-0.41-Coarse-Vf59-
; INITIALIZING THE SOLUTION
/solve/init/init
; calculate
it 2500
; WRITING THE CASE AND DATA FILES - INITIAL RESULT
wcd Eps-0.41-Coarse-Vf59-V2
;NET SET CALCULATIONS
;CHANGE THE DISCRETIZATION SCHEME
/solve/set/discretization-scheme/density 1
/solve/set/discretization-scheme/mom 1
/solve/set/discretization-scheme/temperature 1
;DEFINE CONVERGENCE CRITERIA
/solve/monitors/residual/convergence-criteria
;CONTINUITY
1e-7
```

```

;X-MOMENTUM
1e-7
;Y-MOMENTUM
1e-7
;Z-MOMENTUM
1e-7
;TEMPERATURE
1e-7
; SOLVING NUMBER OF ITERATION
it 5000
; WRITING THE CASE AND DATA FILES - FINAL RESULT
wcd Eps-0.41-Coarse-Vf59-V3
; Exit FLUENT
exit
yes

```

D.1.2 Chemical Reactions

The journal file used to run chemical reaction simulation in BATCH mode using

FLUENT is:

```

; READ CASE FILE
rc PB-Coarse
;AUTO-SAVING CASE AND DATA FILES
/file/autosave/case-frequency 450
/file/autosave/data-frequency 450
/file/autosave/overwrite-existing-files yes
/file/autosave/max-files
1
/file/autosave/root-name/PB-Coarse-Pe0.01-Da0.1-Iter-
/define/models/species/inlet-diffusion
no
; ENTERING CHANGE AND CREATE OPTION
/define/material/change-create
mixture-template

```

```
mixture-template
; CHANGE MIXTURE SPECIES?
no
; CHANGE REACTION
yes
1
; SURFACE REACTION?
yes
; PARTICLE SURFACE REACTION
no
; NUMBER OF REACTANTS
2
; REACTANT-1
h2s
; STOICH. COEFF. OF H2S
1 ; RATE EXPONENT OF H2S
1
; REACTANT-2
zno
; STOICH. COEFF. OF ZNO
1
; RATE EXPONENT OF ZNO
0
; NUMBER OF PRODUCTS
2
; PRODUCT-1
h2o
; STOICH. COEFF. OF H2O
1
; RATE EXPONENT OF H2O
0
; PRODUCT-2
zns
; STOICH. COEFF. OF ZNS
1
; RATE EXPONENT OF ZNS
0
; PRE-EXPONENTIAL FACTOR
17.0
```

```

; ACTIVATION ENERGY (J/KG-MOL)
30312000
; TEMPERATURE EXPONENT
0
; INCLUDE BACKWARD REACTION?
no
; PRESSURE DEPENDENT REACTION?
no
; SPECIFY 3RD BODY EFFICIENCIES?
no
; CHANGE MECHANISM?
no
; CHANGE DENSITY?
no
; CHANGE Cp (SPECIFIC HEAT)?
no
; CHANGE THERMAL CONDUCTIVITY?
no
; CHANGE VISCOSITY?
yes
constant
7.062e-7
; CHANGE MASS DIFFUSIVITY?
yes
; METHODS: (CONSTANT-DILUTE-APPX DILUTE-APPROX MULTICOMPONENT KINETIC-THEORY
USER-DEFINED)
; NEW METHOD [CONSTANT-DILUTE-APPX]
constant-dilute-appx
; NUMBER OF PARAMETERS
1
; PARAM-1 (M2/S)
1.5e-3
; CHANGE THERMAL EXPANSION COEFFICIENT?
no
; CHANGING INLET BOUNDARY CONDITION
/define/boundary-conditions/velocity-inlet
; ZONE ID/NAME
inlet
; VELOCITY SPECIFICATION METHOD: MAGNITUDE AND DIRECTION

```

```

yes
;REFERENCE FRAME: ABSOLUTE
yes
;USE PROFILE FOR VELOCITY MAGNITUDE
no
; VELOCITY MAGNITUDE (M/S)
0.25
; COORDINATE SYSTEM: CARTESIAN (X,Y,Z)
yes
; USE PROFILE FOR X-COMPONENT OF FLOW DIRECTION?
no
;X-COMPONENT OF FLOW DIRECTION
1
; USE PROFILE FOR Y-COMPONENT OF FLOW DIRECTION?
no
;Y-COMPONENT OF FLOW DIRECTION
0
; USE PROFILE FOR Z-COMPONENT OF FLOW DIRECTION?
no
;Z-COMPONENT OF FLOW DIRECTION
0
; USE PROFILE FOR TEMPERATURE?
no
; TEMPERATURE (K)
673
; USE PROFILE FOR DUMMY MASS FRACTION?
no
; DUMMY MASS FRACTION
0
; USE PROFILE FOR H2O MASS FRACTION?
no
; H2O MASS FRACTION
0
; USE PROFILE FOR H2S MASS FRACTION?
no
; H2S MASS FRACTION
0.2575
; SET UNDER-RELAXATION PARAMETERS
/solve/set/under-relaxation/body-force 1

```

```

/solve/set/under-relaxation/density 1
/solve/set/under-relaxation/pressure 0.3
/solve/set/under-relaxation/mom 0.7
/solve/set/under-relaxation/temperature 1
/solve/set/under-relaxation/species-0 1
/solve/set/under-relaxation/species-1 1
/solve/set/under-relaxation/species-2 1
; INITIALIZING THE SOLUTION
/solve/initialize/set-defaults/pressure 0
/solve/initialize/set-defaults/x-velocity 0
/solve/initialize/set-defaults/y-velocity 0
/solve/initialize/set-defaults/z-velocity 0
/solve/initialize/set-defaults/species-0 0
/solve/initialize/set-defaults/species-1 0
/solve/initialize/set-defaults/species-2 0
/solve/initialize/set-defaults/temperature 673
/solve/initialize/initialize-flow
; SOLVING NUMBER OF ITERATION
/solve/iterate
50
; SET UNDER-RELAXATION PARAMETERS
/solve/set/under-relaxation/body-force 1
/solve/set/under-relaxation/density 1
/solve/set/under-relaxation/pressure 0.3
/solve/set/under-relaxation/mom 0.7
/solve/set/under-relaxation/temperature 1
/solve/set/under-relaxation/species-0 1
/solve/set/under-relaxation/species-1 0.9
/solve/set/under-relaxation/species-2 0.9
; SOLVING NUMBER OF ITERATION
/solve/iterate
4000
; WRITING THE CASE AND DATA FILES - FINAL RESULT
wd PB-Coarse-Pe0.01-Da0.1

```

D.2 User Defined Functions

D.2.1 Slip Boundary Condition

UDF used to verify slip model implementation in commercial CFD software (FLUENT) is

```
#include "udf.h"
#include "mem.h"
#define sigma_v 1
DEFINE_PROFILE(Bot_Slip_Wall,t,i)
{
  cell_t c0;
  Thread *t0;
  face_t f;
  real Lamda,rho,rmu,kn,RGas,z;
  real pi=3.14;
  real Twall=300.0;
  begin_f_loop(f,t)
  {
    c0 = F_C0(f,t);
    t0 = F_C0_THREAD(f,t);
    rho = C_R(c0,t0);
    rmu = C_MU_L(c0,t0);
    RGas = C_RGAS(c0,t0);
    Lamda = rmu/(rho*sqrt(2*RGas*Twall/pi));
    kn = Lamda/2e-3;
    z = ((2-sigma_v)/sigma_v)*Lamda*C_DUDY(c0,t0);
    /* we can also use C_U_G(c0,t0)[1] instead of C_DUDY(c0,t0)/
    Message(" n grad %f t knudsen %f", z, kn);
    F_PROFILE(f,t,i) = z;
  }
  end_f_loop(f,t)
}
DEFINE_PROFILE(Top_Slip_Wall,t,i)
{
  cell_t c0;
```



```

Thread *t0;
face_t f;
real Lamda,rho,rmu,kn,RGas,z;
real pi=3.14;
real Twall=300.0;
begin_f_loop(f,t)
{
c0 = F_C0(f,t);
t0 = F_C0_THREAD(f,t);
rho = C_R(c0,t0);
rmu = C_MU_L(c0,t0);
RGas = C_RGAS(c0,t0);
Lamda = rmu/(rho*sqrt(2*RGas*Twall/pi));
kn = Lamda/2e-3;
z = ((2-sigma_v)/sigma_v)*Lamda*C_DUDY(c0,t0);
/* we can also use C_U_G(c0,t0)[1] instead of C_DUDY(c0,t0) */
Message(" n grad %f  t knudsen %f", z, kn);
F_PROFILE(f,t,i) = -z;
}
end_f_loop(f,t)
}

```

D.2.2 Explicit Surface Reaction

UDF to adjust the source terms in surface reaction model

```

#include "udf.h"
#include "sg.h"
#define AP_FRACTION 0.0; /* IMPLICIT FUNCTION */
DEFINE_SOURCE(rxn_source, c0, t0, dS, eqn)
{
Thread *t;
face_t f ;
int nspe = THREAD_NSPE(t0);
int ns,n,nspm = nspe-1;
real At,A[ND_ND],dr0[ND_ND],es[ND_ND],A_by_es,ds,S_FRAC;

```

```

real diff_term[MAX_SPE_EQNS] ;
c_face_loop(c0,t0,n)
{
f = C_FACE(c0,t0,n);
t = C_FACE_THREAD(c0,t0,n);
if(FLUID_THREAD_P(t->t0) && THREAD_F_WALL == THREAD_TYPE(t)&&
THREAD_VAR(t).wall.react && rp_spe_surf)
{
/* CALCULATE THE DIFFUSION TERMS */
F_AREA(A,f,t); At=NV_MAG(A);
BOUNDARY_FACE_GEOMETRY(f,t,A,ds,es,A_by_es,dr0);
spe_loop(ns,nspm)
diff_term[ns]=(A_by_es/ds)(C_R(c0,t0)C_DIFF_L(c0,t0,ns,ns));
/* ADJUST THE SOURCE TERMS */
for( ns=1;ns<nspm;ns++)
{
WALL_F_CVD_AP(f,t,ns) = diff_term[ns] AP_FRACTION ;
S_FRAC = 1-AP_FRACTION ;
WALL_F_CVD_S(f,t,ns) -= diff_term[ns] C_YI(c0,t0,ns) S_FRAC ;
}
}
}
return 0. ;
}

```